Charge transition level energies of the 1+, 2+, 3+, and 4+ 3dq transition metals; new insight and tutorial review

Dorenbos, Pieter

DOI
10.1016/j.optmat.2025.117007

Publication date
2025

Document Version
Final published version

Published in
Optical Materials

Citation (APA)
Dorenbos, P. (2025). Charge transition level energies of the 1+, 2+, 3+, and 4+ 3dq transition metals; new insight and tutorial review. *Optical Materials*, *164*, Article 117007.
https://doi.org/10.1016/j.optmat.2025.117007

Optical Materials 164 (2025) 117007

Contents lists available at ScienceDirect

Optical Materials

journal homepage: www.elsevier.com/locate/optmat

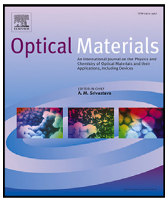

Review article

Charge transition level energies of the 1+, 2+, 3+, and 4+ $3d^q$ transition metals; new insight and tutorial review

Pieter Dorenbos

Delft University of Technology, Faculty of Applied Sciences, Department of Radiation Science and Technology, Mekelweg 15, 2629 JB Delft, Netherlands

ARTICLE INFO

Keywords:
Transition metals
Charge transition levels
VRBE
Crystal field
Chemical shift
Nephelauxetic effect

ABSTRACT

The defect levels of the $3d^q$ transition metals (TM) within the bandgap of compounds provide compounds with properties that are utilized in *e.g.* luminescence, lasers, photochromism, batteries, catalysis, semiconductors, biochemistry. Knowledge of the ground-state level locations, or equivalently the charge transition level (CTL) energies, or equivalently the vacuum-referred binding energies (VRBE), is important to understand or engineer performance. Despite 70 years of interest in the topic, understanding and controlling TM defect levels remains elusive. In this work, experimental data, theories developed, progress over time, and current status are reviewed, and new insights are presented. We will start with the classic theory, first for free-ion $3d^q$ TMs and then for TMs in inorganic compounds and organic complexes. The Slater–Condon F^k, the Racah A, B, and C parameters, the crystal field interaction, and the Tanabe–Sugano diagrams will be treated on a tutorial level. An expression reproducing the CTL energies relative to the vacuum level as a function of the number q of electrons in the $3d^q$ TMs will be derived. The expression contains five essential parameters related to the chemical shift, Racah parameters, the nephelauxetic effect, and the crystal field. Data on TMs of different valences in 18 chemical environments are collected from the literature. These are inorganic compounds ranging from wide-band-gap halides (F, Cl, Br), chalcogenides (O, S, Se), small-band-gap II–VI and III–V semiconductors, and two TM organic complexes. All provide octahedral or tetrahedral coordinated sites for the TM. Data from luminescence and absorption spectroscopy, deep-level transient spectroscopy, photocurrents, thermoluminescence, and electrochemistry are translated into CTL energies. Next, the derived expression is used to reproduce the CTL energies, providing the values of the five parameters for each compound. The parameters appear strongly related to each other and change predictably with the valence of the TM and the properties of the environment.

Contents

E-mail address: p.dorenbos@tudelft.nl.

https://doi.org/10.1016/j.optmat.2025.117007
Received 28 February 2025; Received in revised form 27 March 2025; Accepted 28 March 2025

---

1. Introduction

Transition metals (TM) with $3d^q$ (q=0, 1, 2, …10) electron configuration may adopt valencies ranging from $Q = 1+$ like for Cu$^+$ in Cu$_2$O until $Q = 7+$ like for Mn^{7+} in KMnO$_4$. Either as a dopant in inorganic compounds or as a constituent of the compound they have been studied widely in fields of science like that of the TM laser crystals [1], materials for batteries [2], materials for catalysis, or materials for photoelectric splitting of water [3].

The theory describing the $3d^q$ excited state energy levels of TM elements is well established [4–6], and is frequently applied to explain luminescence and excitation spectra. All of this involves energy differences between the TM energy states. However, determining the level locations within the bandgap of compounds is another issue. The level location refers to the TM charge transition level (CTL) energy. To express it theoretically, we have to deal with the energy difference between the ground state of a transition metal with valence Q and the ground state of the same transition metal with valence $Q + 1$.

In this work, we will find that the Mn$^{4+/3+}$ CTL energy is located around −5 eV relative to the vacuum level as illustrated in Fig. 1. A valence band (VB) top at $E_V = -9$ eV and conduction (CB) bottom at $E_C = -2$ eV typical for a wide-bandgap inorganic compound, are also shown. Let us consider Mn^{4+} as a dopant, and suppose the Fermi energy level of the compound, usually near mid-bandgap energy, is being raised. The Mn$^{4+/3+}$ charge transition level is then defined as the energy where Mn^{4+} will reduce to Mn^{3+}. The CTL energy is equivalent to the vacuum-referred binding energy (VRBE) in the ground state of Mn^{3+}. It therefore requires about 5 eV to bring an electron from Mn^{3+} to the vacuum energy level. The VRBE energy scale is shown on the left-hand side of Fig. 1. With the host-referred binding energy (HRBE) scale shown on the right-hand side, energies are referred to the top of the VB. For the TMs surrounded by organic complexes in solution, the CTLs can be probed in electrochemical cells. CTL energies are then known as redox potentials that are often relative to the standard hydrogen electrode (SHE) potential. With the SHE potential equivalent to −4.44 eV relative to the vacuum level, the reduction potential of Mn $E^0(III/IV)$ is around 0.56 V in the illustration of Fig. 1.

Despite the importance of TM CTL energies for understanding and predicting properties of TM-based functional materials, progress has been little. The foundations of the CTL energies for the TMs but also for the lanthanides were already laid down in the 1950s and 1960s following the fundamental theories of Slater, Condon, Dieke, Racah, Jørgensen, Tanabe and Sugano, and many others. The theory was initially developed for the free ions, *i.e.*, in vacuum. To account for the interactions with ligands and compounds, ligand and crystal field theory were added. However, the complexity of the interactions between a TM and the surrounding ligands and difficulties in obtaining reliable experimental data led to poor predictive models. Some general trends could be observed but variations therein usually not. It seems that different fields of science (TM-doped semiconductors, redox potentials, chromophores, phosphor, etc.) developed their own methods. With the rise of computational methods and power, the success in computing CTL energies of TMs in a chemical environment ab initio and from first principles is increasing [7–12]. At some stage, the correct CTL energy for TMs in each compound or chemical environment may be computed. The classic theories of the 1950s and 1960s [4,13,14] may then become obsolete. However, being able to compute the values does not necessarily provide insight into what interactions and phenomena are at play because of the mere complexity of the computations themselves. For understanding the trends, the classic theories remain of lasting value.

This work will start with a historical overview that covers about 70 years of theoretical and experimental developments on CTL energies of the $3d^q$ TMs of valence 1+, 2+, 3+, and 4+ and also that of the $4f^q$ lanthanides of valence 2+ and 3+. Next, the theory on TMs, first as free ions and then as dopants in an inorganic compound, is presented. The CTL energies of the TMs as free ions will be derived from the expressions for the ^{2S+1}L term energies. The (relative) energy $E_{LS}(q, Q)$ of each term is determined by the electron–electron repulsion energy between the q electrons in the partly filled $3d^q$-orbital of our

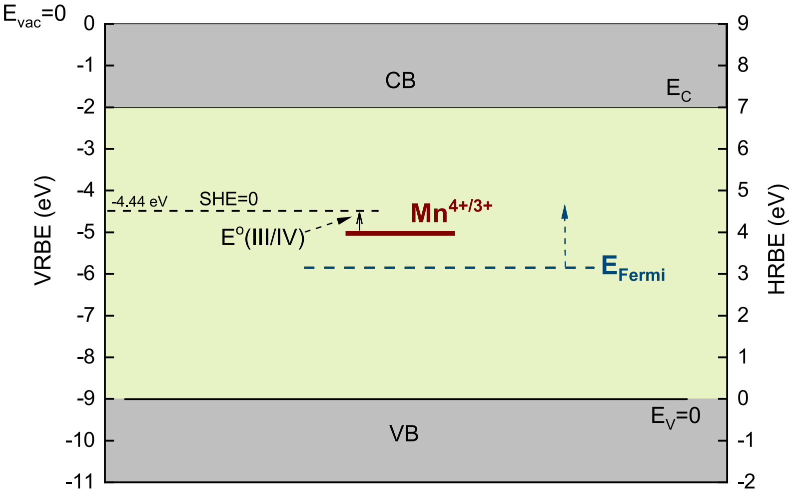

Fig. 1. Illustration of the relation between different energy scales used to place charge transition level energies. On the left, the vacuum-referred binding energy (VRBE) scale with the zero of energy at the vacuum level $E_{\rm vac}=0$. On the right, the host-referred binding energy (HRBE) scale with energy zero at the valence band top $E_V=0$. The zero of the standard hydrogen electrode (SHE) potential corresponds with −4.44 eV on the VRBE scale. The Mn$^{4+/3}$ CTL energy is placed at −5 eV on the VRBE scale, or +4 eV on the HRBE scale, or at redox potential E^o(III/IV)=0.56 V on the SHE scale.

TM of valence Q+. In the theory of Racah and others, this inter-electron Coulomb repulsion is parameterized with the Slater–Condon F^k parameters [4,6]. The energy $E_{LS}(q,Q)$ can then be expressed as a linear combination of these parameters. By adding the spin–orbit interaction with the spin–orbit coupling parameter ζ_{dd}, the energy $E_{LSJ}(q,Q)$ of the $^{2S+1}L_J$ energy level is obtained. In compounds, we have to deal with the crystal field interaction between $3d^q$ electrons and the anion ligands which leads to the introduction of the Tanabe–Sugano diagrams. In addition, one has to deal with covalence and the nephelauxetic effect resulting in a reduction of the Slater–Condon F^k parameters and the spin–orbit coupling parameter ζ_{dd}.

The lanthanide CTL and VRBE energies can be obtained quite successfully with the Chemical Shift model developed in 2012 [15–17]. The success is due to the atomic-like character of the inner lanthanide $4f$ orbital. Each lanthanide has almost the same interaction with the crystal field, and the variation in CTL energy along the lanthanide series when in a compound remains almost unaltered from the free-ion variation. A $3d$ orbital, however, extends to the periphery of the TM that causes an order of magnitude larger interaction with the ligand field, and the CTL shape will be altered from the free-ion shape in many different ways.

To treat the CTL energy or VRBE for the TMs in compounds, one first needs to understand the TMs as free ions in the vacuum where a crystal field and a nephelauxetic effect are absent. The VRBE in the $3d^q$ and $4f^q$ ground states as a function of q are equivalent to minus the ionization potentials, and follow typical zigzag patterns as a function of q or atomic number Z as shown in Fig. 2 for the TMs and in Fig. 3 for the lanthanides.

The smoothly decreasing dashed curves in the lower panels of Figs. 2 and 3 represent the contributions from the bonding of the d (or f) electrons to the inner core of the TM (or Ln) plus the spherical part, *i.e.*, the part that does not depend on the total spin S and total angular momentum L, of the electrostatic repulsion between the d electrons (or the f electrons). For that reason, we will frequently refer to these curves as the spherical interaction curves $C(q,Q,A)$ of the $3d^q$ TM^Q or $4f^q$ Ln^Q in the environment A. The spherical interaction energies for the lanthanides were derived in [16,17], and those for the TMs will be derived in this work. By adding the directional part of the electrostatic repulsion, the typical zigzag patterns in CTL energies are obtained. For future reference, Table 1 compiles the coefficients of the linear and quadratic least squares fits to the found spherical interaction energies.

The Chemical Shift model [15] and later the Refined Chemical Shift (RCS) model [16,17], derive the VRBE in the lanthanide 4f^q ground

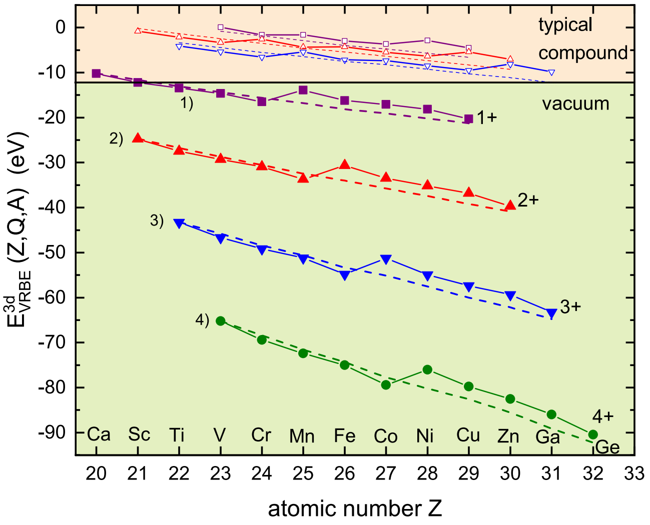

Fig. 2. The lower panel shows the vacuum-referred binding energy in the lowest level of the $3d^q$ electron configuration of free-ion transition metals with valence 1+ curve (1), 2+ curve (2), 3+ curve (3), 4+ curve (4). The dotted lines are the spherical interaction curves $C(q,Q,\text{vac})$ as derived in this work. The upper panel shows VRBEs (solid curves) and the spherical interaction curves (dashed) for the TMs of valence 1+, 2+, and 3+ when in a typical compound.

Table 1
The coefficients $a_0(Q)$, $a_1(Q)$, and $a_2(Q)$ from the least squares linear or quadratic fitting of the spherical interaction energies $C(q,Q,\text{vac})=a_0(Q)+(q-1)a_1(Q)$ for the transition metals and the spherical interaction energies $C(q,Q,\text{vac})=a_0(Q)+(q-1)a_1(Q)+(q-1)^2a_2(Q)$ for the lanthanides. $C(1,Q,\text{vac})$ are the spherical interaction energies in the lowest $3d^1$ TM level and lowest $4f^1$ lanthanide level. Energies are in eV.

	$C(1,Q,\text{vac})$	$a_0(Q)$	$a_1(Q)$	
TM^{1+}	−10.19	−10.54	−1.220	
TM^{2+}	−24.73	−25.06	−1.776	
TM^{3+}	−43.22	−43.50	−2.355	
TM^{4+}	−65.21	−65.46	−2.941	
	$C(1,Q,\text{vac})$	$a_0(Q)$	$a_1(Q)$	$a_2(Q)$
Ln^{2+}	−18.17	−18.49	−1.309	0.0349
Ln^{3+}	−36.59	−36.88	−1.532	0.0355

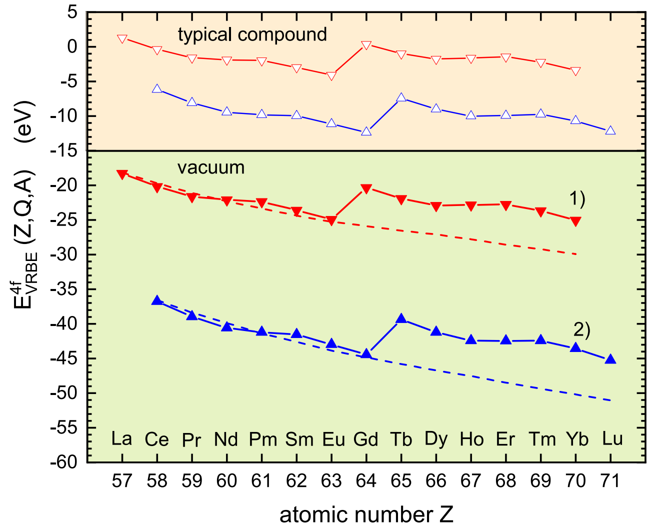

Fig. 3. The lower panel shows the vacuum-referred binding energy in the lowest energy $4f^q$ level of the free-ion lanthanides with valence 2+ curve (1) and valence 3+ curve (2). The dashed curves show the spherical interaction curves $C(q, Q, \text{vac})$ as derived in [16,17]. The upper panel shows the Ln^{2+} and Ln^{3+} VRBEs in a typical compound like YPO_4. Note that the free-ion zigzag shapes remain almost unaltered.

states as a dopant in compounds from the free-ion VRBEs. In this work, we intend to establish to what extent our knowledge and models about the VRBE in the $4f^q$ ground states can be applied to the VRBE in the $3d^q$ ground states. We will start with the Slater–Condon F^k and ζ_{dd} parameters that are available for the di-, tri-, tetra-, and pentavalent free $3d^q$ transition metals from computations by Brik and Ma [6]. Next, the contribution of the inter-electron repulsion between d-electrons to the binding energy in the ground states is determined. Finally, the effect of the chemical shift, the crystal field splitting, and the nephelauxetic effect on the VRBE in the transition metal ground state multiplets when in a chemical environment will be treated. This all leads to an expression for the $TM^{Q+1/Q}$ CTL energy that appears quite similar to what was established in the 1960s [4,13,14,18,19]. We will call this the *classic theory*. An important and unique difference is that, in this work, all CTL energies will be referred to the vacuum level rather than to the valence or conduction band of the host compound or to the SHE potential in electrochemistry.

Eighteen different chemical environments are studied, covering inorganic compounds with bandgaps ranging from > 12 eV in fluorides to < 2 eV for the semiconductors (selenides, phosphides). It also covers CTL energies in water and an organic complex. Experimental and computational data are collected, and derived CTL or VRBE energies will be reproduced by the expression of the classic theory. Clear trends of CTL energy with the number q of $3d$ electrons and with valence Q, and how this all depends on the type of compound will emerge from this study. It provides insight and a broad perspective on how the CTL energies of the TMs behave. We will see that the Racah, crystal field, nephelauxetic, and chemical shift parameters in the expression follow clear trends. Trends that can be compared with similar ones for the lanthanides, and that provide predictive potential.

The top panel of Fig. 2 already illustrates the main outcome of this work. It shows the CTL energies in a typical compound. The free-ion spherical interaction curves in the lower panel of Fig. 2 are tilted counterclockwise due to the nephelauxetic effect, and shifted up due to the chemical shift from the surrounding negative charge of the environment. The spherical interaction curves shown for valences 1+, 2+, and 3+ are moved to the 0 to −10 eV region and run almost parallel and close to each other. The final CTL energies are obtained by adding the directional part of the interaction energies. 0 to −10 eV is the energy range where the top of the valence band, the bandgap, and the bottom of the conduction band of inorganic compounds are usually found. Other than the lanthanides in the upper panel of Fig. 3, the zigzag shapes of the free-ion TM curves are fully distorted when in a compound.

2. Historical overview

Experimental determination and theoretical modeling of the CTL energies of the TMs and the lanthanides in chemical environments have received quite a lot of attention in the past 70 years in different fields of science. Often, each field deals with a specific class of materials, uses a different reference of energy, uses different names for the same concept, and employs different types of experiments. This means that fragments of data and information are distributed over different fields of science at different periods in our 70-year history. It also means that knowledge is fragmented in time and discipline. In this section, the different disciplines, periods, and models are placed in a historical perspective.

CTL energies are relevant whenever an electron is added to or removed from an nl^q orbital where $n = 3, 4, 5$ and $l = 2$ for transition metal d orbitals. $n = 4$ and $l = 3$ for the lanthanide $4f$ orbitals. Ionization energies or electron affinities relate to the CTL energies in the gaseous state, *i.e.*, when the vacuum is the environment. Theories describing excited lanthanide $4f^q$ states and TM nd^q states as free ions were developed in the 1940s and 1950s [20,21]. Soon thereafter, the effect of the ligand or crystal field was added to explain level energy differences in a chemical environment. For the lanthanides, the $4f^q$ energy level diagram in any environment remains very close to that of the free ions. The Dieke diagram [22] of excited states gives in most cases an adequate description. The nd^q level diagrams for the TMs in compounds are much different from the free-ion diagrams, and one then uses the so-called Tanabe–Sugano diagrams of the energies of nd^q excited states. The theories behind the TM level energies can be found in textbooks [4,6].

Jørgensen in 1959 [13] explored whether theories describing excited states can be used to explain strong absorption bands in hexahalide TM complexes. For example, in the $OsCl_6^{2-}$ hexachloride $5d^4$ osmium complex, a strong absorption band can be attributed to electron transfer from the chlorine ligand to Os^{4+}, which then reduces to Os^{3+}. With the energy of the absorption band, the $Os^{4+/3+}$ CTL energy is probed relative to the electron binding energy in the chlorine ligand. In 1962, a similar study was performed on lanthanide organic complexes by Jørgensen [18]. This all led to the formulation of his spin pairing theory to explain the characteristic zigzag shapes observed in ionization energies and electron transfer spectra. In the book by Griffith in 1961 [4] the basis theory that explains the ionization potentials of the divalent free-ion transition metals can be found. Allen in 1964 [14] added the effect of the crystal field at tetrahedral sites in ZnS to semi-empirically calculate the $TM^{3+/2+}$ CTL energies. Later, Mizushima and co-workers in the 1970s [19,23] used that method to predict the $TM^{3+/2+}$, $TM^{4+/3+}$, and $TM^{5+/4+}$ CTL energies in the bandgap of TiO_2 that provide octahedral sites.

Whereas d orbital crystal field splitting provides a large (up to 1 eV) contribution to the TM CTL energy, it is quite insignificant (< 0.1 eV) for the lanthanide CTL energy. McClure and Kiss [24] related the $4f^q \rightarrow 4f^{q-1}5d^1$ optical transition energies of divalent lanthanides in CaF_2 to the free-ion ionization potentials and Jørgensen theory in 1963. As with ionization, an electron is removed from the $4f^q$ orbital in these optical transitions. Thermodynamic properties like the enthalpy of formation of the lanthanide metals are also linked to the ionization energies of the lanthanides. Johnson [25] applied the spin pairing theory in 1969 to treat the third ionization energies and the sublimation energies of the lanthanides, and Nugent in 1970 [26] to treat the so-called tetrad effect in lanthanide and actinide solvents. Morss in 1976 [27] and Johnson in 1974 [28] correlated experimental data on electron transfer spectra, redox potentials, and formation enthalpies of the lanthanide metals with each other and with the ionization potentials. In the 1970s, Jørgensen theory was applied in a series of papers by Nugent and co-workers [29–34] to explain and predict those properties for the lanthanides and actinides. Much later, Kawabe in 1992 used spin pairing theory to study its effect on lanthanide ionic radius, and how properties relate to the reduction of Racah parameters due to the nephelauxetic effect [35].

Redox potentials in electrochemistry also deal with adding (oxidation) or removing (reduction) an electron from a TM or a Ln when dissolved in a liquid like water. The effect of the ligand field was observed in the Fe(II/III) and Co(II/III) redox potentials in various solvents, and a correlation with the $10Dq$ crystal field splitting was suggested by Rock [36] in 1968. Later in 1980, Lintvedt and Fenton [37] commented that the directional crystal field leading to crystal field splitting alone cannot explain the variation in the redox potentials of the TMs with changing type of ligand. The spherical part of the ligand field should also be taken into account. The situation was reviewed and further modeled in 1982 by van Gaal and van der Linden [38]. An analysis in terms of changing Racah parameters and the classic theory of Ref. [4,13,14,18,19] was not, to the authors' knowledge, made in this field of science.

Many studies have appeared in the 1980s on the TMs as dopants in II–VI and III–V semiconductors. As deep impurity states, the TMs may act as electron donors or acceptors for which the CTL location is crucial. Based on electron transfer bands, photo-ionization thresholds, deep-level transient spectroscopy, ESR, etc., the CTL location in the bandgap has been determined for various TMs in different semiconductors. Ledebo et al. [39] in 1982 and also Caldas et al. [40] in 1984 showed that the VRBE energy of the same TM^Q in different semiconductors tends to be fairly constant when energy is referred to the vacuum level. These are the first papers that relate CTL energies relative to the vacuum level. Note that redox potentials can also be converted to VRBE energies. However, in electrochemistry, such an approach is rarely followed. Many papers followed in the 1980s to better understand TM deep-level states [41–44] in III–V semiconductors like GaAs, GaP, InP, GaSb, and in II–VI semiconductors like ZnS, CdS, ZnSe, CdSe, CdTe. In 1989, Delerue et al. [42] used full computational methods to obtain the TM impurity levels. They also expressed the *need for simpler models to point out the main physical properties of TM impurities and to perform a systematic analysis of trends*. In all those studies, an interpretation with the classic theory employing Racah parameters was again not made. Besides, these studies are limited to small band-gap semiconductors, and the connection with other fields of science where other chemical environments are the subject of study is then missed.

TMs in wide-bandgap inorganic compounds form another class of chemical environments. The wide bandgap enables one to study the energies of the $3d^q$-$3d^q$ transitions from which, with the help of the Tanabe–Sugano diagrams, the Racah parameters and the magnitude of crystal field splitting can be obtained, see *e.g.* [45]. McClure and coworkers [46,47] worked in this field in the 1960s and 1970s. TM^{3+} in Al_2O_3 was studied in 1962 focusing on the $3d^q$-$3d^q$ transitions and not yet on the VB→ TM^{3+} CT-band energies [46]. This was done by Tippins [48] in 1970 who for interpretation used a simple model based on the free-ion TM^{2+} ionization potential and the octahedral crystal field splitting of the $3d$ levels in the compound. Sabatini et al. [47] followed that analysis in their studies of TMs in $KMgF_3$, MgF_2, and CaF_2. In 1978, Coutts [49] studied Fe^{2+}, Co^{2+}, and Ni^{2+} in $CdCl_2$ and $CdBr_2$. From the VB→TM^{2+} CT bands, the $TM^{2+/1+}$ CTL energies relative to the VB-top were obtained, and the authors used the classic theory for interpretation. The work by McClure [50] in 1979 on the TM^{2+} in LiF, $KMgF_3$, and LiCl collects electron transfer data. For the fluoride compounds, transfer from the TM provides information on $TM^{3+/2+}$ CTL energies relative to the CB-bottom (or the 4s states), and for LiCl transfer to the TM provides information on $TM^{2+/1+}$ CTL energies relative to the VB-top.

McClure and Pedrini in 1985 [51] derived $Ln^{3+/2+}$ CTL energies relative to the bottom of the conduction band from photoionization studies in Ln^{2+} doped CaF_2, SrF_2, and BaF_2. They found that the CTL curve is a counterclockwise tilted version of the free-ion ionization curve and attributed the tilt to lattice relaxation around the impurity. This explanation was adopted by Thiel et al. [52] to explain XPS data on trivalent lanthanides in $Y_3Al_5O_{12}$ sixteen years later in 2001. Dorenbos [53] used the idea to explain VB→ Ln^{3+} CT-energies of the lanthanides in about 50 different compounds in 2003. Ten years later this evolved into the Chemical Shift model of 2012 [15] where for the first time lanthanide CTL energies and lanthanide VRBEs could be determined relative to the vacuum energy level.

The classic theory of ionization potentials and CTL energies developed in the early 1960s [4,13,14,18,19] and employed in the following decades seems to become less popular for explaining experimental data in the 1990s. With the growth of computational power, methods to compute the location of TM or lanthanide levels in the bandgap gained popularity [7,8,42,54,55]. Qu and co-workers computed the energy needed to excite an electron from the VB-top to the TM for the entire series of TMs at octahedral sites in Al_2O_3 and in $Y_3Al_5O_{12}$ in 2019 [56]. In 2022 similar computations were done for the TMs in compounds providing tetrahedral sites [57]. CTL energies appear to follow a characteristic pattern, and the authors propose to use that same pattern as a predictive tool for other compounds. This work will show that the pattern, however, changes from compound to compound. Jing and co-workers [9–11] computed the CTL energies of the TMs relative to the VB-top in several different compounds. They went a step further by also computing VRBE energies. A method was proposed to parameterize the results to arrive at predictive models. Unfortunately, the classic theory was not used to interpret the computational results.

One may conclude from the above historical overview, that the classic theory on TM CTL energies was already laid down in the early days. However, it was never fully exploited to analyze CTL data covering different types of materials (wide-bandgap inorganics, semiconductors, and organic complexes) from differing fields of science. Usually, energies were related to the VB-top but rarely to the vacuum level. It seems that the classic theory has somehow even been forgotten.

3. Theory on the free $3d^q$ transition metals

For a free TM ion, each electron in the $3d^q$ orbital, whether it is in the ground or in an excited state, will experience the same interaction with the inner core consisting of the nucleus and the electrons of the [Ar] closed shells electron configuration [4]. This means that the remaining interactions determine energy differences between $3d^q$ states, *i.e.*, the mutual Coulomb repulsion between the q $3d$ electrons, and the spin–orbit interactions. Each state or energy level can be characterized by the quantum numbers L, S, and J of the total orbital momentum, the total spin momentum, and the total angular momentum (spin plus orbital) of all q electrons. The ${}^{2S+1}L_J$ symbol is then used to label each state of the free ions. Ignoring spin–orbit interaction for the moment, one needs to compute the total energy $E^{dd}_{LS}(q,Q)$ of Coulomb repulsion between all the q d-electrons to obtain the ${}^{2S+1}L$ term energies relative to each other. The repulsion energy between any two nl electrons is given by an integral of the form

$$E = \frac{e^2}{4\pi\epsilon_0}\int Y^*_{lm}(\theta_2,\phi_2)Y^*_{lm}(\theta_1,\phi_1)R_{nl}(r_2)R_{nl}(r_1) \times \frac{1}{r_{12}}Y_{lm}(\theta_2,\phi_2)Y_{lm}(\theta_1,\phi_1)R_{nl}(r_2)R_{nl}(r_1)\,dV_1\,dV_2 \quad (1)$$

where r_1 and r_2 are the distances to the nucleus of the two interacting electrons, and r_{12} is the distance between the two electrons. R_{nl} and Y_{lm} are the radial and angular parts of the nl wavefunction. The entire integral can be reduced to a linear combination of the so-called F^k Slater–Condon integrals [4,6],

$$F^k = \frac{e^2}{4\pi\epsilon_0}\iint \frac{r^k_<}{r^{k+1}_>}R_{nl}(r_1)^2R_{nl}(r_2)^2r_1^1r_2^2\,dr_1\,dr_2 \quad (2)$$

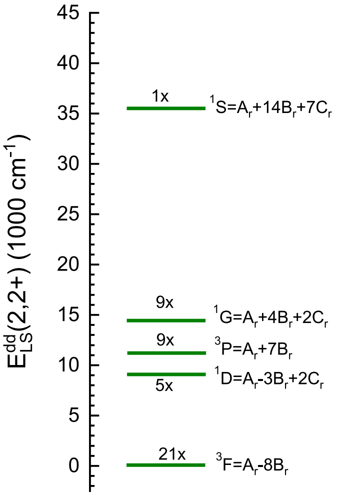

Fig. 4. The ^{2S+1}L level scheme for the free-ion $3d^2$ Ti^{2+} constructed with Racah B_r=735 cm^{-1} and Racah C_r=2730 cm^{-1}. The level energies $E^{dd}_{LS}(q=2, Q=2+)$ are expressed as linear combinations in the Racah parameters A_r, B_r, and C_r. The (2S+1)(2L+1) degeneracy numbers are provided. $E^{dd}_{LS}(2,2+)$ for the ^3F ground state ^{2S+1}L term is defined as the zero of energy.

that contain only the radial parts of the wavefunctions. $r_< = r_1$ and $r_> = r_2$ when $r_1 < r_2$, and $r_< = r_2$ and $r_> = r_1$ when $r_2 < r_1$. The angular part of the integral of Eq. (1), which depends on L and S, determines the coefficients in the linear combination. When $nl = 3d$, only for $k = 0, 2$, and 4 the angular part is non-zero, and Eq. (1) becomes a linear combination of the F^0, F^2, and F^4 Slater–Condon integrals.

Rather than the three F^k parameters, usually the A_r, B_r, and C_r Racah parameters are used to parameterize the energy of inter-electron repulsion in the TMs [20]. Here we added the subscript r to avoid confusion with other symbols used in this work. The Racah parameters are positive numbers (energies) and linear combinations of the F^k parameters as in the following expressions [4,6,58].

$$A_r \equiv F^0 - \frac{1}{9}F^4 = F^0 - \frac{7}{5}C_r \tag{3}$$

$$B_r \equiv \frac{1}{49}F^2 - \frac{5}{441}F^4 = \frac{1}{49}F^2 - \frac{1}{7}C_r \tag{4}$$

$$C_r \equiv \frac{5}{63}F^4 \tag{5}$$

Each energy $E^{dd}_{LS}(q,Q)$ can now be expressed as a linear combination of the three Racah parameters

$$E^{dd}_{LS}(q,Q) = a_A A_r(q,Q) + n_B B_r(q,Q) + m_C C_r(q,Q) \tag{6}$$

where the values for the coefficients a_A, n_B, m_C are all well-documented [4,6,21]. a_A is always equal to $q(q-1)/2$ and independent on L or S. Racah parameter A_r therefore represents the spherical part of the electrostatic interaction between $3d$ electrons. B_r and C_r represent the directional parts, and their coefficients n_B and m_C do depend on L and S. Fig. 4 shows the LS-level scheme for the $3d^2$ free-ion Ti^{2+} with the expressions for each ^{2S+1}L-term. From the experimental energy differences between ^{2S+1}L-terms, one may derive the values for B_r and C_r but not for A_r. Since the coefficient a_A is the same for each ^{2S+1}L-term, the Racah A_r contribution always drops out in energy differences between ^{2S+1}L-terms.

A ^{2S+1}L-term will be further split by the spin–orbit interaction leading to $2J+1$ different $^{2S+1}L_J$ levels. The total energy $E_{LSJ}(q,Q)$ of all q electrons of a TM with valence Q in a $^{2s+1}L_J$-term is now written as a sum of three contributions

$$E_{LSJ}(q,Q) = E_{ic}(q,Q) + E^{dd}_{LS}(q,Q) + E^{so}_{J}(q,Q) \tag{7}$$

where the inner-core bonding $E_{ic}(q,Q)$ represents the attractive interaction of each of the q electrons with the positive nucleus and the 18 electrons of the [Ar] electron configuration. The attraction is spherically symmetric and independent on L, S, or J. $E^{dd}_{LS}(q,Q)$ is given by Eq. (6), and $E^{so}_{J}(q,Q)$ is an additional small contribution to the total energy from spin–orbit interaction.

To further express $E_{ic}(q,Q)$, the nuclear charge $Z(q,Q)$ of the $3d^q$ TM^Q is written as $Z(q,Q) = Z(1,Q) + (q-1)$. We will next separate the bonding of each of the q electrons into (1) a contribution from the bonding $-W(q,Q)$ with the positive charge $Z(1,Q)$ and the 18 electrons from the [Ar] configuration, and (2) a contribution from the bonding $-(q-1)V(q,Q)/2$ with the (q-1) remaining positive charges at the nucleus. Since each of the q $3d$ electrons will have the same bonding with the inner core (see *e.g.* the treatment in section 4.3 in [4]), the bonding of all q electrons together with the inner core can be written as

$$E_{ic}(q,Q) = -qW(q,Q) - \frac{q(q-1)}{2}V(q,Q) \tag{8}$$

where both W and V are positive quantities such that E_{ic} is negative. For the $3d^1$ transition metals $E_{ic}(1,Q) = -W(1,Q)$ which are the same as $C(1,q,\text{vac})$ in Table 1. $V(q,Q)/2$ has a magnitude of the order

$$\frac{V}{2} = \frac{e^2}{4\pi\epsilon_0}\langle r^{-1}\rangle = \frac{e^2}{4\pi\epsilon_0}\int_0^\infty \frac{1}{r}(R_{3d}(r))^2 r^2 dr \tag{9}$$

where $\langle r\rangle$ the average distance of the $3d$ electron to the nucleus. The expression for $W(q,Q)$ will contain a similar term from the bonding to $Z(1,Q)$ plus a repulsive term from the interaction with the [Ar] electron configuration. An important aspect is that both $W(q,Q)$ and $V(q,Q)$ scale with $\langle r^{-1}\rangle$.

Next, we need to add the electrostatic e-e repulsion energy $E^{dd}_{LS}(q,Q)$ of Eq. (6) that applies to the ^{2S+1}L-term of the TM and the term $E^{so}_{J}(q,Q)$ to Eq. (7). Since $a_A = q(q-1)/2$, Eq. (7) can now be written as

$$\begin{aligned} E_{LSJ}(q,Q) = {} & -qW(q,Q) - \frac{q(q-1)}{2}(V(q,Q) - A_r(q,Q)) \\ & + n_B B_r(q,Q) + m_C C_r(q,Q) + p_\zeta \zeta_{dd}(q,Q) \end{aligned} \tag{10}$$

where the value of the coefficient a_A and $V/2$ are joined in the second term. $E^{s.o.}_J$ is proportional to the spin–orbit coupling parameter ζ_{dd} with coefficient p_ζ.

In this work, we are mostly interested in the total energy in the ground state, and the coefficients n_B and m_C with B_r and C_r then refer to that ground state. For the ^{3}F ground state of Ti^{2+}, $E^{dd}_{LS} = A_r - 8B_r$ and thus $a_A = 1$, $n_B = -8$, and $m_C = 0$. Note, when Racah parameters A_r, B_r, and C_r are replaced with the Racah parameters E^0, E^1, and E^3 for electrostatic interaction between $4f$-electrons, a similar expression is obtained for $E_{LSJ}(q,Q)$ of the $4f^q$ lanthanide of valence Q; see Eq. (SI-1) and Dorenbos [16] for further details.

p_ζ is the coefficient with the spin–orbit coupling parameter ζ_{dd} that for the free-ion ground states evaluates to [58,59]

$$p_\zeta = \frac{-(L+1)}{2} \tag{11}$$

for q is 1 to 4 and

$$p_\zeta = \frac{-L}{2} \tag{12}$$

for q is 6 to 9. p_ζ is zero for q = 0, 5, and 10. For the Ti^{2+} ^{3}F ground state with $L = 3$, Eq. (11) yields $p_\zeta = -2$. The coefficients with A_r, B_r, C_r, and ζ_{dd} in Eq. (10) for the ground states of the $3d^q$ transition metals with valence 1+, 2+, 3+, 4+ are gathered in Table 2. They can also be found in Table 4.12 of Ref. [4].

$W(q,Q)$, $V(q,Q)/2$, and $A_r(q,Q)$ cannot be experimentally determined. Computational studies show that $A_r(q,Q)$ increases almost linearly with q, and the same is expected for $W(q,Q)$ and $V(q,Q)/2$. Then also the sum of the first two terms in Eq. (10) is expected to be a smoothly decreasing function with q. We will define this sum as $c(q,Q)$ that collects all spherical parts of the interactions in the TM,

$$c(q,Q) \equiv -qW(q,Q) - \frac{q(q-1)}{2}(V(q,Q) - A_r(q,Q)). \tag{13}$$

Table 2
The coefficients for the energy terms of inter-electron dd repulsion and spin–orbit interaction for gaseous (free) transition metals with the $3d^q$ configuration in the $^{2S+1}L_J$ ground state.

q	TM^{1+}	TM^{2+}	TM^{3+}	TM^{4+}	g.s.	$a_A = \frac{q(q-1)}{2}$	n_B	m_C	p_ζ
0	–	–	Sc	Ti	$^1S_0$	0	0	0	0
1	–	Sc	Ti	V	$^2D_{3/2}$	0	0	0	−3/2
2	–	Ti	V	Cr	$^3F_2$	1	−8	0	−2
3	–	V	Cr	Mn	$^4F_{3/2}$	3	−15	0	−2
4	V	Cr	Mn	Fe	$^5D_0$	6	−21	0	−3/2
5	Cr	Mn	Fe	Co	$^6S_{5/2}$	10	−35	0	0
6	Mn	Fe	Co	Ni	$^5D_4$	15	−35	7	−1
7	Fe	Co	Ni	Cu	$^4F_{9/2}$	21	−43	14	−3/2
8	Co	Ni	Cu	Zn	$^3F_4$	28	−50	21	−3/2
9	Ni	Cu	Zn	Ga	$^2D_{5/2}$	36	−56	28	−1
10	Cu	Zn	Ga	Ge	$^1S_0$	45	−70	35	0

The sum of the remaining three terms of Eq. (10) will be defined as $s(q,Q)$. It collects the directional parts of the interactions in the TM, and contains the experimentally accessible B_r, C_r, and ζ_{dd} parameters,

$$s(q,Q) \equiv n_B B_r(q,Q) + m_C C_r(q,Q) + p_\zeta \zeta_{dd}(q,Q). \tag{14}$$

Eq. (10) for the ground state (g.s.) LSJ-term energy becomes

$$E_{g.s.}(q,Q) = c(q,Q) + s(q,Q). \tag{15}$$

In the equation

$$E_{g.s.}(q,Q) + \Delta E = E_{g.s.}(q-1,Q+1), \tag{16}$$

ΔE is the energy needed to remove an electron from the ground state of a $3d^q$ TM of valence Q and bring it to the vacuum energy level. After removal, we are left with the TM in the $3d^{q-1}$ ground state with valence $Q+1$. Then, $-\Delta E$ is equivalent to the vacuum-referred binding energy $E_{VRBE}(q,Q,\text{vac})$ in the ground state of the $3d^q$ TM^Q. It is also equivalent to the TM$^{Q+1/Q}$ CTL energy. A = vac has been added as a variable in $E_{VRBE}(q,Q,A)$ to denote that the ambient A or chemical environment is the vacuum.

$$\begin{aligned} E_{VRBE}(q,Q,\text{vac}) &\equiv E_{g.s.}(q,Q,\text{vac}) - E_{g.s.}(q-1,Q+1,\text{vac}) \\ &= C(q,Q,\text{vac}) + S(q,Q,\text{vac}) \end{aligned} \tag{17}$$

where

$$C(q,Q,\text{vac}) \equiv c(q,Q,\text{vac}) - c(q-1,Q+1,\text{vac}) \tag{18}$$

is again expected to be a smoothly varying function with q, and

$$S(q,Q,\text{vac}) \equiv s(q,Q,\text{vac}) - s(q-1,Q+1,\text{vac}) \tag{19}$$

can be evaluated from the experimentally accessible or computed values for the parameters B_r, C_r, and ζ_{dd} for TM^Q and TM^{Q+1} as free cations in the vacuum. $C(q,Q,\text{vac})$ will be referred to as the spherical interaction energy and $S(q,Q,\text{vac})$ as the directional interaction energy.

The spherical interaction energy cannot be determined experimentally. However, it can be derived from the experimentally known $E_{VRBE}(q,Q,\text{vac})$ and the experimentally or computationally derived $S(q,Q,\text{vac})$ energies. The values of $E_{VRBE}(q,Q,\text{vac})$ as obtained from the National Institute of Standards and Technology [60] are compiled in Table 3 and shown in Fig. 2. Except for Ca$^+$, Sc$^+$, and Ti$^+$, $E_{VRBE}(q,Q,\text{vac})$ is the same as minus the 2nd, 3rd, 4th, or 5th ionization potential.

4. Data and results on the free $3d^q$ transition metals

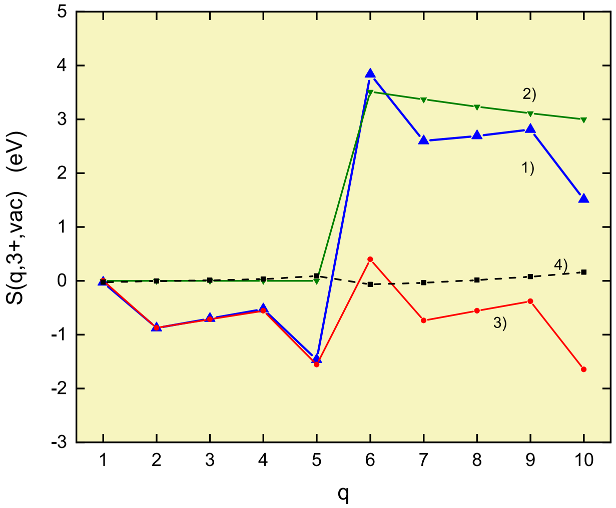

Fig. 5. Curve (1) shows the contribution $S(q,3+,\text{vac})$ to the VRBE of the free trivalent $3d$ transition metals and (2), (3), and (4) the separate contributions from C_r, B_r, and ζ_{dd}, respectively.

To employ Eq. (17) to analyze the binding energy for the free monovalent, divalent, trivalent, and tetravalent TMs, we need the Racah parameters $B_r(q,Q,\text{vac})$ and $C_r(q,Q,\text{vac})$ together with $\zeta_{dd}(q,Q,\text{vac})$ of the TMs in the 1+, 2+, 3+, 4+, and 5+ valence state. We will use the Hartree–Fock (HF) calculated parameters by Brik and co-workers [5,6]. The F^k_{HF}, A_r, B_r, C_r, and $\zeta^{1/4}_{dd}$ increase to good approximation linearly with the atomic number Z, or equivalently with the number of electrons in the $3d$-orbital. Therefore, instead of compiling the values for each TM^Q, we can work with the coefficients of the linear relationships. The coefficients from [6] are compiled for Q = 2+, 3+, 4+, and 5+ in Table 4. The coefficients of the linear relations change when Q increases from 2+ to 5+. Using a least squares quadratic extrapolation to Q = 1+, the coefficients for the linear expressions for Q = 1+ were obtained.

The experimental values are systematically smaller than the calculated ones. The Slater–Condon F^k_{exp} and the three Racah parameters are ≈ 0.8 times the HF-values, and $\zeta_{\text{exp}} \approx 0.9\zeta_{\text{HF}}$. Using this together with the linear relations in Table 4 and the definition of $S(q,Q,\text{vac})$ and $s(q,Q,\text{vac})$, we have everything to compute the directional contribution $S(q,1+,\text{vac})$, $S(q,2+,\text{vac})$, $S(q,3+,\text{vac})$, and $S(q,4+,\text{vac})$ to the free TM ion $E_{VRBE}(q,Q,\text{vac})$ energy. As an example, the function $S(q,3+,\text{vac})$ is shown as curve (1) in Fig. 5. The separate contributions from the B_r, C_r, and ζ_{dd} terms in Eqs. (14) and (17) are shown as curves 2, 3, and 4. Figures SI-1, SI-2, and SI-3 show the equivalent curves for Q = 1+, 2+, and 4+.

The most important feature is the jump between q = 5 and 6. Column 9 of Table 2 shows that C_r does not contribute for Ti^{3+} with q = 1 until Fe^{3+} with q = 5, but for Co^{3+} with q = 6 there is a $7C_r$ eV contribution to the e-e repulsion. The contribution decreases when approaching the end of the TM series as illustrated in curve (2). The reason is that after the removal of a $3d$ electron, the radial function $R_{3d}(r)$ has shrunk and Racah $C_r(q-1,4+,\text{vac})$ will be larger than $C_r(q,3+,\text{vac})$ before. Similar pertains to the lanthanides where a jump appears between q=7 and 8 due to the sudden appearance of a 9

Table 3

Atomic number Z, $E_{VRBE}(q, Q, \mathrm{vac})$ (in eV) in the lowest $3d^q$ level, and the Shannon ionic radii $R(Q)$ in pm of the mono-, di-, tri-, and tetravalent TMs. We used the tabulated radii for TMs in 6-fold coordination from [61]. Values between braces refer to the low spin [LS] ground state of the TM.

Z	TM	$E_{VRBE}(1+)$	$E_{VRBE}(2+)$	$E_{VRBE}(3+)$	$E_{VRBE}(4+)$	$R(1+)$	$R(2+)$	$R(3+)$	$R(4+)$
20	Ca	−10.20	–	–	–	–	–	–	–
21	Sc	−12.20	−24.75	–	–	–	–	74.5	–
22	Ti	−13.46	−27.47	−43.25	–	–	86	67	60.5
23	V	−14.63	−29.31	−46.69	−65.25	–	79	64	58
24	Cr	−16.49	−30.95	−49.14	−69.43	–	(73)80	61.5	55
25	Mn	−13.90	−33.69	−51.18	−72.42	–	(67)83	(58)64.5	53
26	Fe	−16.20	−30.64	−54.8	−75	–	(61)78	(55)64.5	58.5
27	Co	−17.08	−33.49	−51.28	−79.46	–	(65)74.5	(54.5)61	53
28	Ni	−18.17	−35.16	−54.91	−76.03	–	69	(56)60	48
29	Cu	−20.29	−36.83	−57.35	−79.77	77	73	54	–
30	Zn	–	−39.71	−59.36	−82.56	–	74	–	–
31	Ga	–	–	−63.24	−86.01	–	–	62	–
32	Ge	–	–	–	−90.5	–	–	–	53

Table 4

The linear relationships between the calculated Racah parameters $A_r(q, Q, \mathrm{vac})$, $B_r(q, Q, \mathrm{vac})$, and $C_r(q, Q, \mathrm{vac})$, and of $\zeta_{dd}(q, Q, \mathrm{vac})$ with the number of electrons q in the $3d$ orbital of the free TM^Q ions (Q = 2+, 3+, 4+, 5+). The calculated relations are from [6]. The $\frac{1}{4}^{th}$ power of the calculated spin–orbit coupling parameter ζ_{dd} are shown as linear functions of the atomic number Z. The relationships for Q = 1+ are obtained from extrapolation from those for Q = 5+, 4+, 3+, and 2+. One needs to multiply calculated Racah values by 0.8 and spin–orbit coupling values by 0.9 to reach an agreement with the experimental values.

Q	$A_r(q, Q, \mathrm{vac})$ (eV)	$B_r(q, Q, \mathrm{vac})$ (meV)	$C_r(q, Q, \mathrm{vac})$ (meV)	$\zeta^{1/4}_{dd}(q, Q, \mathrm{vac})$ (eV$^{1/4}$)
1+	$10.94 + 1.443q$	$65.88 + 9.030q$	$242.2 + 33.06q$	$0.03123(Z - 11.385)$
2+	$14.75 + 1.366q$	$94.62 + 8.490q$	$350.7 + 30.91q$	$0.02986(Z - 10.021)$
3+	$18.27 + 1.307q$	$120.0 + 8.079q$	$451.0 + 29.27q$	$0.0288(Z - 8.822)$
4+	$21.35 + 1.278q$	$143.2 + 7.896q$	$539.0 + 28.53q$	$0.02807(Z - 7.879)$
5+	$24.19 + 1.263q$	$162.7 + 7.81q$	$620.2 + 28.17q$	$0.02765(Z - 7.071)$

times Racah E^1 contribution [16]. The contribution from B_r illustrated by curve (3) creates the zigzagging VRBE in the left-hand and right-hand branch of the $S(q, Q, \mathrm{vac})$ curve. B_r also contributes to the jump in the $S(q, Q, \mathrm{vac})$ energy between $q = 5$ and $q = 6$. Such a zigzagging pattern is also present for the lanthanides where it is caused by the Racah parameter E^3 [16]. This pattern is known as the tetrad effect for the lanthanides [26,35]. The name is not encountered with the TMs, probably because crystal field interactions create stronger zigzag patterns than those from B_r as can also be seen in the upper panel of Fig. 2. The spin–orbit contribution illustrated by curve (4) has a minor influence on the overall shape.

The experimentally known $E_{VRBE}(q, Q, \mathrm{vac})$ energies from Table 3 were shown in Fig. 2. By subtracting the directional interaction energies $S(q, Q, \mathrm{vac})$ in Fig. SI-1, Fig. SI-2, Fig. 5, and Fig. SI-4, one obtains the spherical interaction energies $C(q, Q, \mathrm{vac})$. The energies are compiled in Table SI-I, and they are connected by the dashed curves in Fig. 2. As for the lanthanides in Fig. 3, they are indeed varying smoothly with q although for $C(q, 3+, \mathrm{vac})$ and $C(q, 4+\mathrm{vac})$ the curves undulate slightly. Unless this is supposed to be, it may signal that the values used for the Racah parameters B_r and C_r deviate somewhat from the true ones. The spherical interaction energies for the TMs can be well represented with $a_0(Q) + (q-1)a_1(Q)$. The parameters a_0 and a_1 of this linear relation are obtained from a least squares fitting to $C(q, Q, \mathrm{vac})$ and can be found in Table 1. The energies for the lanthanides as established in [16] are better represented with a quadratic dependence. The three parameters from a quadratic least squares fitting can also be found in Table 1.

5. Theory on transition metals in inorganic compounds and organic complexes

For TMs in inorganic compounds or organic complexes, the positive charge of the TM will be screened by the negative charge from the anions or molecular ligands. That charge will interact with the $3d$ electrons and the inner core in various ways. In this work, we mostly deal with chemical environments that provide point symmetry O_h at the TM-site. An illustrative example is a TM surrounded by a set of six point charges Z located at the vertices of a regular octahedron. The point charges create a crystal or ligand field potential $V(r, \theta, \phi)$ that interacts with the $3d$ electrons. Eq. (20) is the general expression [6]

$$V(r,\theta,\phi) = \frac{6Ze^2}{4\pi\epsilon_0 R} + \frac{7Ze^2}{8\pi\epsilon_0 R^5} r^4 \left(C^4_0(\theta,\phi) + \sqrt{\frac{5}{14} C^4_4(\theta,\phi) + C^4_{-4}(\theta,\phi)} \right) \tag{20}$$

with

$$C^k_m(\theta,\phi) = \sqrt{\frac{4\pi}{2k+1}} Y_{km}(\theta,\phi) \tag{21}$$

and with Y_{km} the spherical harmonic functions. Expressions for other symmetries than octahedral can *e.g.* be found in the tutorial review by Gorller-Walrand and Binnemans [62]. The first term of Eq. (20) is the spherical part of the crystal field, and the other is the directional part. The spherical part is often ignored because it drops out when one is interested in energy differences between crystal field states. However, the spherical part is essential for the VRBE and CTL energies. The directional part leads to the crystal field splitting of the energy levels. Its interaction with the shielded $4f$ electrons in the lanthanides is small ($<$ 0.1 eV) and can be ignored. However, the interaction with electrons excited to lanthanide $5d$ orbitals or with $3d$ electrons of TMs can amount to several eV, and the directional part becomes quite important.

5.1. Lanthanide CTL energies in compounds

Before starting with the CTL energies for the TMs in compounds, the main findings on the CTL energies for the lanthanides in compounds are presented. The lanthanides taught us that several interactions must be accounted for to derive CTL energies in a chemical environment. The chemical shift E_{cs} of VRBE due to the Coulomb repulsion from the $-Q$ screening charge of the surrounding ligands at an effective screening distance $R_Q(A)$ is the most important. It causes an upward shift of $4f$ electron binding energy

$$E_{cs}(Q,A) = \frac{eQ}{4\pi\epsilon_0 R_Q(A)} = \frac{1440Q}{R_Q(A)} \tag{22}$$

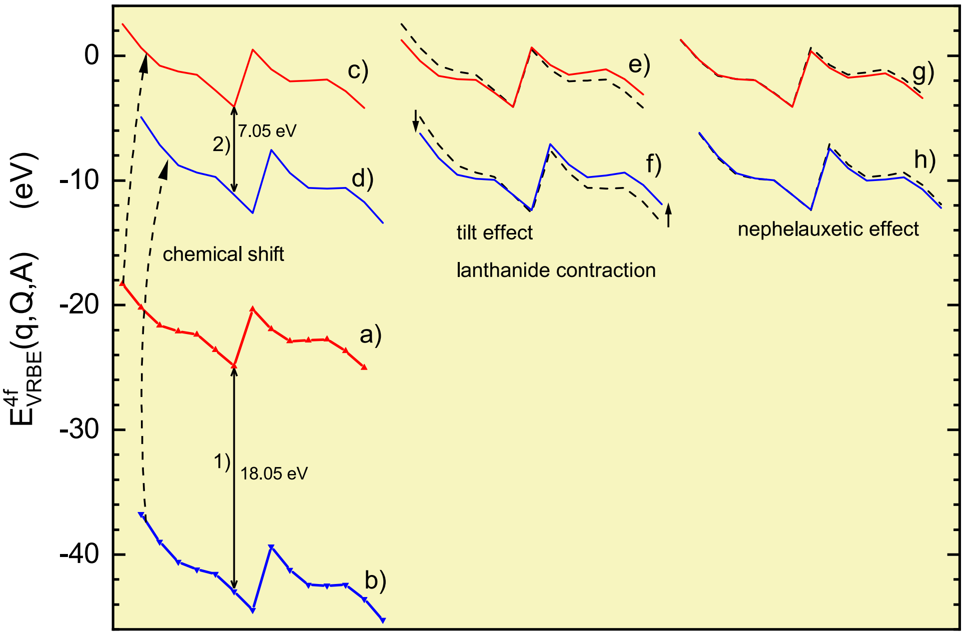

Fig. 6. Demonstration of how the free lanthanide ion CTL energies alter when they are placed in a chemical environment. Curve (a) connects the $Ln^{3+/2+}$ and curve (b) the $Ln^{4+/3+}$ free lanthanide ion CTL energies. Curves (c) and (d) demonstrate how the CTL energies change due to the chemical shift when U=7.05 eV. Solid curves (e) and (f) demonstrate the counterclockwise tilting of the CTL curves attributed to the lanthanide contraction. The dashed curves are the same as (c) and (d). Solid curves (g) and (h) demonstrate the nephelauxetic effect. The most important change is a lowering of the right-hand branch of the CTL curve. The dashed curves are the same as (f) and (e).

where in the expression on the far right, energy is in eV and distance in pm. The chemical shift is equivalent to the spherical part of the crystal field.

The VRBEs for the free lanthanides in Fig. 3 are shown as curves (a) and (b) in Fig. 6. In the example of Fig. 6 that pertains to the lanthanides in YPO_4, the $Ln^{3+/2+}$ CTL curve (a) shifts up by 20.8 eV to obtain curve (c). The $Ln^{4+/3+}$ CTL curve (b) shifts up by 31.8 eV resulting in curve (d). The factor of 1.52 between the two shifts is close to the ratio 3/2 between $Q = 3+$ and $Q = 2+$ as predicted with Eq. (22). The energy difference between the $Eu^{4+/3+}$ and the $Eu^{3+/2+}$ CTL energy, as illustrated with arrows (1) and (2), decreases from 18.05 eV to 7.05 eV. The Chemical Shift model provides an expression that relates this difference, known as the $U(A)$-value, with the VRBE energy in the Eu^{2+} ground state [15]

$$E_{VRBE}(\mathrm{Eu}^{2+}) = -24.92 + \frac{18.05 - U(A)}{0.777 - 0.0353U(A)}. \tag{23}$$

where −24.92 eV is the 3rd ionization potential of Eu, and the second term on the right-hand side is the size of the chemical shift $E_{cs}(\mathrm{Eu}^{2+}, A)$.

The $U(A)$-value can be derived experimentally, but can also be predicted quite well from the composition of the compound [63]. The chemical shift for TMs is expected to correlate strongly with that for lanthanides when they have the same valence and are located on the same site in the same compound.

The size of the chemical shift of Eq. (22) depends on the type of lanthanide due to the lanthanide contraction. Curves (1), (2), and (3) in Fig. 7, show that from the beginning to the end of the lanthanide series, the ionic radius decreases by 28 pm, 18 pm, and 14 pm. With a smaller radius, the screening charge can approach the lanthanide closer because of lattice relaxation around the defect. This results in a shorter screening distance and increasingly larger Coulomb repulsion and chemical shift. The effect was noticed by McClure and Pedrini in 1985 [51] for divalent lanthanides in CaF_2, SrF_2, and BaF_2. Effectively, this leads to a counterclockwise tilting of the VRBE curve that may change the CTL energies by several electronvolts. The tilt is illustrated with curves (f) and (e) in Fig. 6.

The nephelauxetic effect provides the next contribution to the CTL energies. The interaction between $4f$ electrons and anion ligands reduces the inter-electron $4f - 4f$ repulsion, and Racah parameters become smaller. The reduction is usually attributed to an expansion of the $R_{4f}(r)$ radial function. Depending on the type of compound, it causes 0.1 to 0.3 eV change in the CTL energies [16]. The effect is weak, and appears only significant for the right-hand branch of the zigzag curve as illustrated with curves (g) and (h) in Fig. 6.

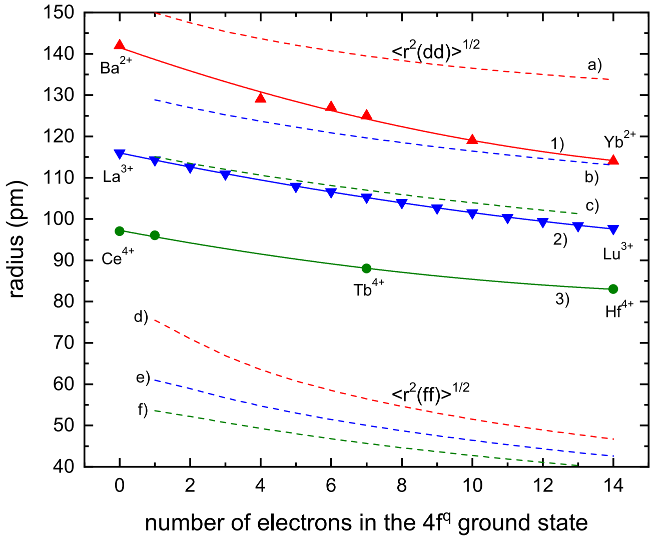

Fig. 7. The ionic radius (in pm) from the Shannon Tables [61] of Ln^Q cations and Ba^{2+} and Hf^{4+} of curve (1) Q=2+, curve (2) Q=3+, and curve (3) Q=4+ at sites with 8-fold coordination. Solid lines are fitted quadratic polynomials. Dashed lines (a), (b), and (c) connect computed $\sqrt{\langle r^2\rangle}$ values for the free-ion excited state $5d^1$ orbitals from [6]. Dashed lines (d), (e), and (f) connect computed $\sqrt{\langle r^2\rangle}$ values for the free-ion $4f^q$ orbitals from [6].

An even smaller effect is caused by the crystal field splitting of the ground states caused by the directional part of the crystal field potential. The splitting can be observed with high-resolution excitation

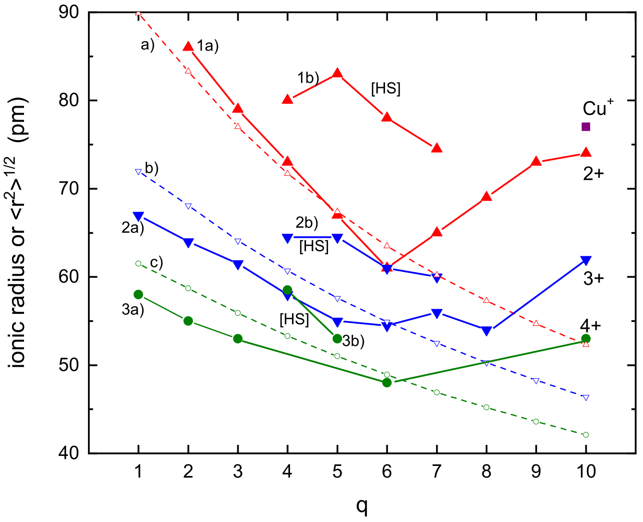

Fig. 8. The ionic radii (in pm) from the Shannon Tables [61] for TM cations of valence 1+ (Cu^+), 2+ curve (1a), 3+ curve (2a), and 4+ curve (3a) on 6-fold anion coordinated lattice sites in halides and chalcogenides against the number q of electrons in the $3d$ orbital. For $q = 4$, 5, 6, and 7 a differentiation between the low spin [LS] and the high spin [HS] states (curves 1b, 2b, and 3b) is made. The spin state for $3d^4$ Fe^{4+} was not specified in [61], but based on the systematics for other TMs the [HS] spin state was assumed in this work. Dashed lines (a), (b), and (c) with open symbols are computed $\sqrt{\langle r^2\rangle}$ values for the free-ion $3d^q$ orbitals from [6].

or absorption spectroscopy of the lanthanide $4f^n \rightarrow 4f^n$ transitions. However, for the CTL energies, the effect is smaller than the error in CTL energy determination, and therefore it will not be considered further.

Figs. 6 and 3 show that despite various interactions, the original shapes of the free lanthanide CTL curves remain almost the same when the lanthanides are in a chemical environment.

5.2. The chemical shift and the centroid shift

Curves (d), (e), and (f) in Fig. 7 show that $\sqrt{\langle r^2(\mathrm{ff})\rangle}$ for the $4f^q$ orbitals of the free lanthanides are $\approx 2\times$ smaller than their ionic radii in compounds which are determined by the filled $5s^2$ and $5p^6$ orbitals of their [Xe] electron core. This again demonstrates that $4f$-orbitals are inner orbitals. The situation for the TMs is different. Fig. 8 shows the ionic radii of TM^Q at octahedral sites in compounds from Shannon [61] that can be found in Table 3. The figure also shows the computed $\sqrt{\langle r^2(\mathrm{dd})\rangle}$ radii for the free-ion $3d^q$ orbitals from [6]. For $q = 1-6$ the computed radii follow the Shannon radii. The deviating behavior for the so-called high spin [HS] states when $q = 4,5,6,7$ will be addressed later. Unlike $4f$ orbitals, the d-orbitals extend to the periphery of the cation and have a much stronger interaction with the anion ligands. One may then wonder to what extent Eq. (22) for the chemical shift will also apply to the $3d$-orbitals of TMs. Again, the knowledge gained from the lanthanides can be used to answer that question.

Fig. 9 illustrates the situation for Ce^{3+} as a free ion in the vacuum on the left and in a chemical environment on the right. The $4f^1$ ground state level is at VRBE of −36.76 eV. The $4f^0 5d^1$ excited state is split by the spin–orbit interaction and its average energy is 6.35 eV above the ground state. In a chemical environment A, the $4f^1$ VRBE shifts by an amount $E_{cs}(\mathrm{Ce}^{3+}, A)$, and if the same applies to the $4f^0 5d^1$ excited states, the average energy of the excited $5d^1$ levels should again be 6.35 eV above the $4f^1$ ground state level. However, this is not observed experimentally. The right-hand side of Fig. 9 shows that the $5d^1$ levels are split by the crystal field into five separate energy levels. The average energy appears lowered by an amount ϵ_c known as the centroid shift. Both crystal field splitting and centroid shift have been analyzed in detail for Ce^{3+} in many different compounds [64–68]. The centroid shift ranges from 0.5 eV in fluoride compounds to larger than 3 eV in selenide compounds. The shift has been attributed to a correlated motion between $5d$ electron and ligand electrons combined with covalence between $5d$-states and anion states [69]. The knowledge about the $5d^1$ level energies of Ce^{3+} should apply equally to the $3d^1$ level energies of TMs like Sc^{2+}, Ti^{3+}, and V^{4+} and to $4d^1$ and $5d^1$ TMs.

The centroid shift of the Ce^{3+} $5d$-levels can be determined by measuring the five 4f-5d transition energies with optical spectroscopy. This is not possible for TMs where only $3d^q - 3d^q$ transitions can be probed. Nevertheless, one may expect that correlated motion and covalence will also reduce the chemical shift for the TMs.

5.3. The nephelauxetic effect

The Racah parameters B_r and C_r for the $3d^q$ TM^Q become smaller when the TM is in a chemical environment. Their values can be derived from the experimental $3d^q \rightarrow 3d^q$ excitation or absorption energies by employing the Tanabe–Sugano diagrams. The Racah values for Mn^{4+} with $3d^3$ configuration in 27 different compounds were reviewed by Brik et al. [70]. $B_r(3, 4+, A)$ ranges from 568 cm^{-1} to 997 cm^{-1} and $C_r(3, 4+, A)$ from 2800 cm^{-1} to 4074 cm^{-1}. When compared with the (corrected) computed free-ion values of $B_r = 1080$ cm^{-1} and $C_r = 4030$ cm^{-1} derived from Table 4, the Racah parameters B_r and C_r are reduced. Traditionally, this reduction is explained by a $3d$-orbital charge cloud expansion resulting in a larger average separation between $3d$-electrons and hence smaller inter-electron repulsion energy E^{dd}_{LS}. This is referred to as the nephelauxetic effect, where nephelauxetic is Greek for cloud expansion. An expanded $R_{3d}(r)$ radial function will according to Eq. (2) reduce the Slater–Condon parameters F^k and hence following Eq. (3), (4), (5) the Racah Parameters $A_r(q, Q, A)$, $B_r(q, Q, A)$, and $C_r(q, Q, A)$. The reduction will, following Eq. (9), also reduce the interaction with the inner core expressed by $V(q, Q, A)$ and $W(q, Q, A)$ in Eq. (8). $A_r(q, Q, A)$, $V(q, Q, A)$, and $W(q, Q, A)$ cannot be determined experimentally. Only $W(1, Q, \mathrm{vac})$ for the free ions is known but how it changes in compounds can also not be determined experimentally. There are computed values of $A_r(q, Q, \mathrm{vac})$ for the free TM cations from Brik and Ma [6]. $A_r(q, Q, \mathrm{vac})$ increases almost linearly with q and the linear coefficients are provided in Table 4. Because parameters cannot be determined experimentally, their effect on CTL energies has never been treated properly. In this work, a first attempt will be made and its influence on CTL energies will be treated.

The ratio between the Racah parameter for a TM in a compound and that for a free TM ion is known as the nephelauxetic ratio β. The nephelauxetic ratio $\beta_A(q, Q, A) \equiv A_r(q, Q, A)/A_r(q, Q, \mathrm{vac})$ and β_B and β_C are defined likewise. To this, we will add the ratios β_V and β_W. The spin–orbit coupling parameter ζ_{dd} also reduces in compounds, and a β_ζ ratio can be defined as well. It is not possible to determine β_W, β_A, and β_V separately. They are all related to spherical interactions, and assuming they have about the same values we will define the spherical nephelauxetic parameter β_{sp} to represent all three. The results for Mn^{4+} demonstrate that $\beta(3, 4+, A)$ in fluorides and oxides is around 0.6-0.7, and we will see later that it can be as low as 0.3 in small-bandgap II–VI and III–V semiconductors or in some types of TM organic complexes. In the above data on Mn^{4+}, $\beta_B(3, 4+, A)$ often differs from $\beta_C(3, 4+, A)$.

In the theory on the $4f$ orbitals of the lanthanides, the coefficients in the linear combination of F^k Slater–Condon integrals are non-zero for $k = 0, 2, 4$, and 6 that leads to a set of four Racah parameters E^0, E^1, E^2, and E^3. For the lanthanides only one β ratio is used in the Refined Chemical Shift model [16,17] to represent the reduction of Racah parameters E^1 and E^3. It varies from 0.98 in highly ionic fluorides to 0.9 in highly covalent selenides. The reduction in β for lanthanides is therefore a factor of 5–10 less than for $3d$-transition metals.

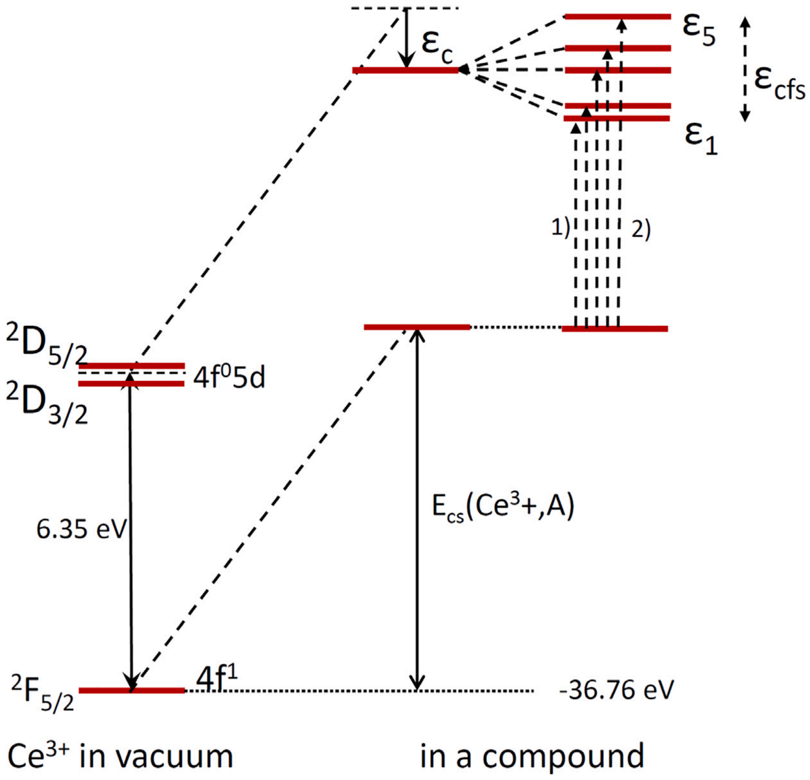

Fig. 9. Illustration of VRBEs in the $4f^1$ ground and $4f^0 5d^1$ excited states of Ce^{3+} as free ion on the left and in a chemical environment on the right. The free-ion level VRBE undergoes an upward chemical shift of $E^{4f}_{cs}(Ce^{3+}, A)$. The interaction with the chemical environment leads to a centroid shift ϵ_c and crystal field splitting of $5d$-levels.

5.4. The crystal field splitting and filling of 3*d*-orbitals

In the free TM ions, the $3d$ orbitals are, apart from spin–orbit splitting, 5-fold degenerate and can accommodate at most 10 electrons. Upon filling the $3d$ orbital with q electrons, the state with the maximum total spin quantum number will form the ground state. This is a manifestation of Hund's first rule and finds its origin in the exchange interaction that causes the average distance between electrons in open orbitals to be largest when total spin is maximal thus minimizing $e-e$ repulsion. The first five electrons of $3d^q$ and the first seven of $4f^q$ align parallel to form the ground state ^{2S+1}L-term. The 6th $3d$ electron or 8th $4f$ electron cannot be aligned anymore. This is the origin for the jumps in the free-ion zigzag curves in Figs. 2 and 3.

In compounds, depending on the point symmetry at the site where the TM is located, the 5-fold degeneracy is lifted resulting in at most five different $3d$ levels as illustrated for Ce^{3+} in Fig. 9. Fig. 10 illustrates the splitting in a lower energy t_{2g} triplet and higher energy e_g doublet state that is formed at a 6-fold octahedrally coordinated site providing O_h point symmetry. The two e_g orbitals are directed towards anion ligands and will have relatively high energy. The three t_{2g}-orbitals are directed in between anion ligands and will have relatively low energy. The energy difference between the two states can be derived by using the crystal field potential of Eq. (20) as a perturbation. It is commonly expressed as the $10Dq$ crystal field splitting [6]

$$10Dq = 10\frac{1}{4\pi\epsilon_0}\frac{35Ze^2}{4R^5}\frac{2}{105}\langle r^4\rangle = \Delta \tag{24}$$

where $\langle r^4\rangle$ is the expectation value for r^4 of the d electron. Here we will use the symbol Δ for the crystal field splitting instead of $10Dq$ to avoid the otherwise confusing use of symbol q.

Another common anion coordination around a TM is that of a regular tetrahedron from four coordinating anions with T_d point symmetry at the TM site. In this case a lower energy e_2 doublet state ($\epsilon_1 = \epsilon_2 = -3/5\Delta$) and upper t_2 triplet state ($\epsilon_3 = \epsilon_4 = \epsilon_5 = +2/5\Delta$) is formed. When the bond lengths are the same, $\Delta_{tetra} = -\frac{4}{9}\Delta_{oct}$. 5-fold coordination, 7-fold coordination, and distorted octahedral or tetrahedral coordination with a low point symmetry are also possible. It will lead to splitting into five separate states with energy ϵ_i ($i = 1, 2, \ldots, 5$) relative to the centroid energy.

Crystal field splitting has been analyzed in depth for the $4f^0 5d^1$ excited states of Ce^{3+} and the $4f^6 5d^1$ excited states of Eu^{2+} in many different compounds providing many different anion coordination polyhedrons [65–68]. All the experimental data demonstrate that crystal field splitting is determined by the shape and the size of the anion coordination polyhedron. The formal charge Z of the N coordinating anions appears of little relevance, *i.e.*, the energies ϵ_i produced by F^-, by O^{2-}, or by N^{3-} are practically the same as long as the shape and size of the coordination polyhedron remain the same [71]. Rogers and Dorenbos [71] suggested to replace the formal charge Z by the screening charge Q/N per coordinating anion in Eqs. (20) and (24). Rather than the formal charge of the anions, the crystal field splitting would become proportional to the formal charge Q of the central Ln^Q or TM^Q cation. This would predict that the crystal field splitting of Ce^{3+} should be 1.5 times larger than that of Eu^{2+}. Experimentally, it appears 1.3 times as large [72,73]. The difference is probably related to the factor $\langle r^4\rangle/R^5$ in Eq. (24). One should realize that the point charge model of Eq. (24) is not very realistic, and should not be used to arrive at quantitative agreements. It is nevertheless expected that $\Delta(Q)$ for TM^Q will increase when Q increases.

The above deals with situations with just one electron in the d-orbital. For $3d^q$ systems, we need to fill the five d levels with q electrons so that the total energy is minimum in the ground state. Upon filling, the electrons tend to align their spins but also tend to occupy the next lowest energy crystal field state; whatever is energetically more favorable. For the situation of Fig. 10, the first three electrons will always enter the t_{2g} state with all three electron spins oriented parallel. The 4th electron can be antiparallel in the t_{2g} state (arrow 4b) forming the so-called low spin [LS] ($2S+1$=3) t^4_{2g} electron configuration.

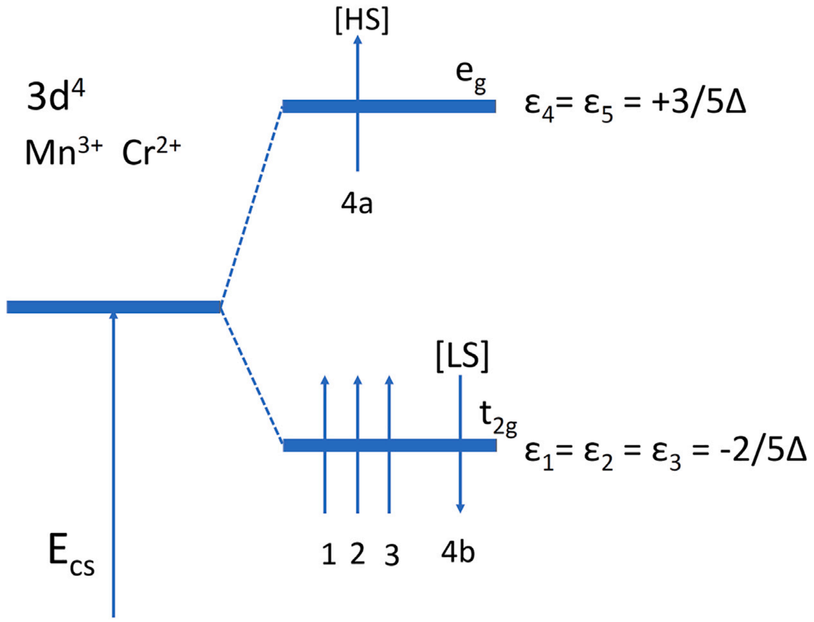

Fig. 10. Illustration of occupation of octahedral crystal field levels with the [HS] $t_{2g}^3 e_g$ and the [LS] t_{2g}^4 electron configurations that may belong to *e.g.* Mn^{3+} or Cr^{2+} in compounds providing 6-fold octahedral coordinated sites.

Alternatively, it may enter the e_g state with parallel spin (arrow 4a) forming the high spin [HS] $(2S+1=5)$ $t_{2g}^3 e_g^1$ electron configuration. This happens when the energy gained in spin alignment is larger than the energy Δ lost in occupying the higher energy e_g state. [LS] and [HS] states are also possible for $q = 5$, 6, and 7, but for $q = 8$, 9, and 10 we only deal with one possible ground state electron configuration.

The length of the TM to the anion bond on the octahedral sites in compounds increases when the e_g state is occupied. The reason is that e_g-orbitals are oriented more towards the anion ligands than t_{2g}-orbitals. It leads to stronger $3d$-electron-ligand repulsion translating to a higher energy crystal field state and longer TM to anion bond length. Fig. 8 therefore shows for $q = 4$, 5, 6, and 7 larger ionic radii for the [HS] states than for the [LS] states. Fig. 8 shows also that when electrons are added to the t_{2g} orbital until it is filled when $q = 6$, the ionic radius decreases continuously. The radii follow nicely the computed $\sqrt{\langle r^2 \rangle}$ for free ions. For $q = 7$ until 10, the e_g orbital is bound to become occupied with electrons, and the ionic radius increases again whereas the free-ion $\sqrt{\langle r^2 \rangle}$ keeps decreasing. Note that the behavior is different for the lanthanides in Fig. 7 where the ionic radius for all q is determined by the [Xe]-core of the lanthanide and, apart from the lanthanide contraction, not by the filling of the inner $4f$-orbital.

The relatively strong interaction between electrons in the e_g orbitals and anion ligands may also lead to a Jahn–Teller (JT) effect. The anions surrounding the TM move slightly to distort the octahedral symmetry, and the t_{2g} and e_g levels are further split resulting in energy lowering of the ground state. The JT-effect can be observed in optical spectroscopy and may amount, in special cases, to several 0.1 eV. In theory, it may also alter the CTL energy, but in this work the JT-effect will be ignored.

5.5. CTL energies of the [HS] ground states

We wish to explore to what extent the CTL energies of TMs in compounds can be derived from the free-ion CTL energies for which Eq. (17) was derived using Eq. (10) as input. Eq. (10) contains expressions for the total bonding of the q $3d$ electrons with the inner core, the spherical and directional parts of the electrostatic interaction between the d electrons, and the spin–orbit interaction. Before implementing the chemical shift, the nephelauxetic effect, and the crystal field interaction, one needs to explore how the expression for electrostatic interaction alters in a chemical environment. This can be done for chemical environments with octahedral (O_h) or tetrahedral (T_d) point symmetry sites. Instead of the ${}^{2S+1}L$-terms of the free ion that apply in the case of full rotational symmetry, one should work with the ${}^{2S+1}\Gamma$ representations from group theory that belong to octahedral or tetrahedral symmetry. This is illustrated for a d^2 TM in O_h point symmetry with the Tanabe–Sugano diagram of Fig. 11. On the far left where $\Delta/B_r=0$ we find the same sequence of free-ion ${}^{2S+1}L$-terms as in Fig. 4. In the presence of a crystal field, the ${}^3F$ level separates into ${}^3T_1$, ${}^3T_2$, and ${}^3A_2$ terms that belong to the [HS] t_{2g}^2, $t_{2g}e_g$, and e_g^2 electron configurations. The ${}^3T_1$ (t_{2g}^2) term forms the ground state, and ${}^3T_2$, and ${}^3A_2$ are at about Δ and 2Δ higher energy since one or two electrons are in the Δ higher energy e_g orbital. A second ${}^3T_1$ term evolves from the higher energy ${}^3P$ ${}^{2S+1}L$-term. In such cases of double occurrence of the same term, one must calculate the genuine ground state energy from diagonalizing a 2×2 matrix. The expression for the energy of the two ${}^3T_1$ terms for d^2 (see *e.g.* Table 8.2 in [6]) in octahedral symmetry reads

$$E({}^3T_1, 3d^2) = A_r + \frac{1}{2}\Delta - \frac{1}{2}B_r \pm \sqrt{\frac{1}{4}(\Delta + 9B_r)^2 + 36B_r^2} \tag{25}$$

In the weak-field approximation when Δ goes to zero one obtains the two energies $A_r{-}8B_r$ and $A_r{+}7B_r$ that are the same as the expression for the ${}^3F$ ground state and ${}^3P$ excited state of the free d^2 ion in Fig. 4. In the strong-field approximation when Δ becomes very large, one obtains $A_r - 5B_r$ for the ${}^3T_1$ ground state and $A_r + 4B_r + \Delta$ for the ${}^3T_1$ excited state. This shows that the coefficient n_B of electrostatic repulsion in the ground state has changed. The coefficients a_A and m_C remain the same. Table 5 shows for each $3d^q$ TM, the strong-field coefficients a_A, n_B, and m_C together with the ground state representations and the free-ion ${}^{2S+1}L$-terms they emanate from. Apart from $q = 2$ and 7, they are the same as that of the free ions in Table 2. For a $3d^7$ TM, the ${}^4T_1$ representation emanates as $t_{2g}^5e^2$ electrons configuration from the free-ion ${}^4F$ ground state and also as $t_{2g}^4e_g^3$ electron configuration from the ${}^4P$ excited state. Again a 2×2 matrix needs to be solved yielding

$$E({}^4T_1, 3d^7) = 21A_r + \frac{1}{2}\Delta + 14C_r - \frac{71}{2}B_r \pm \sqrt{\frac{1}{4}(\Delta + 9B_r)^2 + 36B_r^2}. \tag{26}$$

In the strong-field approximation, the coefficient m_B changes from −43 to −40, and those of a_A and n_C remain the same.

We now have all the tools to express the total energy of our q $3d$-electrons when the TM is in a compound providing a site of O_h point

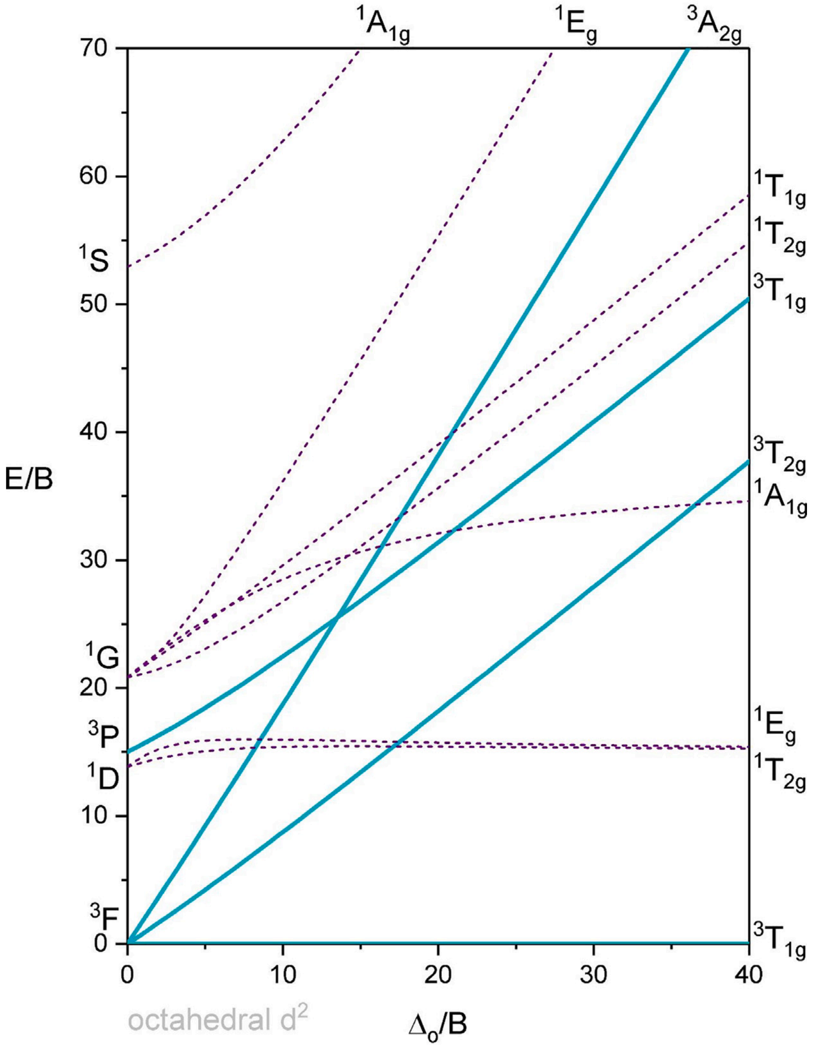

Fig. 11. Tanabe–Sugano diagram for a d^2 transition metal at a site of O_h point symmetry for $C_r/B_r \approx 4$.
Source: Adapted from LibreTexts Chemistry [74].

Table 5
The strong-field coefficients for the energy terms of inter-electron $3d - 3d$ repulsion for the $3d^q$ TMs on octahedrally coordinated sites in the high spin [HS] electron configurations. The $^{2S+1}\Gamma$ representations of the ground state and the ^{2s+1}L terms they arise from are in column 5. The electron configuration of the crystal field levels is in column 6.

q	TM^{2+}	TM^{3+}	TM^{4+}	$[^{2S+1}L]^{2S+1}\Gamma$	conf.	a_A	n_B	m_C
0	–	Sc	Ti	$[^1S]\ ^1A_1$	t_{2g}^0	0	0	0
1	Sc	Ti	V	$[^2D]\ ^2T_2$	t_{2g}	0	0	0
2	Ti	V	Cr	$[^3F,\ ^3P]\ ^3T_1$	$t_{2g}^2,\ t_{2g}e$	1	−5	0
3	V	Cr	Mn	$[^4F]\ ^4A_2$	t_{2g}^3	3	−15	0
4	Cr	Mn	Fe	$[^5D]\ ^5E$	$t_{2g}^3 e_g$	6	−21	0
5	Mn	Fe	Co	$[^6S]\ ^6A_1$	$t_{2g}^3 e_g^2$	10	−35	0
6	Fe	Co	Ni	$[^5D]\ ^5T_2$	$t_{2g}^4 e_g^2$	15	−35	7
7	Co	Ni	Cu	$[^4F,\ ^4P]\ ^4T_1$	$t_{2g}^5 e_g^2,\ t_{2g}^4 e_g^3$	21	−40	14
8	Ni	Cu	Zn	$[^3F]\ ^3A_2$	$t_{2g}^6 e_g^2$	28	−50	21
9	Cu	Zn	Ga	$[^2D]\ ^2E$	$t_{2g}^6 e_g^3$	36	−56	28
10	Zn	Ga	Ge	$[^1S]\ ^1A_1$	$t_{2g}^6 e_g^4$	45	−70	35

symmetry. One has to start with Eq. (15), Eq. (13), and Eq. (14). The coefficients of Table 2 need to be used in the weak-field approximation, and those of Table 5 in the strong-field approximation. Without approximating, Eq. (25) when $q = 2$ and Eq. (26) when $q = 7$ must be used to obtain the proper energies of the directional electrostatic interaction between the d electrons. Later, we will see that the differences between both approximations are 0.2–0.4 eV. Technically, the coefficient p_ζ with ζ_{dd} will also change for $q = 2$ and 7. However, since spin–orbit interaction contributes little to the CTL energy, the values in Table 2 will always be used for $q = 2$ and 7.

Next, the interaction energy with the spherical and directional parts of the crystal field must be added. Expressing the spherical part as

$E_{sp}(q, Q, A)$ one obtains

$$\begin{aligned} E_{g.s.}(q, Q, A) = & -qW(q, Q, A) - \frac{q(q-1)}{2}(V(q, Q, A) - A_r(q, Q, A)) \\ & + n_B B_r(q, Q, A) \\ & + m_C C_r(q, Q, A) + p_\zeta \zeta_{dd}(q, Q, A) + qE_{sp}(q, Q, A) \\ & + \sum_{i=1}^{5} \epsilon_i(q, Q, A) o_i(q, Q, A) \end{aligned} \tag{27}$$

where the centroid shift $\epsilon_c(q, Q, A)$ of the crystal field levels is now within $E_{sp}(q, Q, A)$. N.B., in the absence of a centroid shift, one might write $E_{sp} = 1440Q/R_Q$ as in Eq. (22). The summation in the last term is the interaction energy of the q $3d$-electrons with the directional part of the crystal field. ϵ_i is the energy of the ith level relative to the centroid energy. o_i is the occupancy of level ϵ_i that can be 0, 1, or 2 with $\sum o_i = q$. In the special case of octahedral coordination with O_h point symmetry at the TM site $\epsilon_1 = \epsilon_2 = \epsilon_3 = \frac{-2}{5}\Delta$ and $\epsilon_4 = \epsilon_5 = \frac{+3}{5}\Delta$.

Eq. (27) expresses the total energy of the q $3d$ electrons from the interactions internal to the TM plus the interactions with the environment. Eq. (17) for the CTL or VRBE energy evaluates the difference in these total energies when in the vacuum before and after removing a $3d$ electron. One should realize that in a compound we have to take the interaction of the TM^{Q} with the environment before and that of TM^{Q+1} after removal of a $3d$ electron. Upon removal of one electron from $3d$, all other electrons in the TM, in the ligands, and for that matter the entire compound have adapted to the new situation. The $(R_{3d}(r))^2$ function has shrunk and the Racah parameters have increased. This is accounted for by the $S(q, Q, A)$ term in Eq. (17). However, the environment will polarize and the screening charge will change from Q to $Q+1$. This changes the spherical interaction energy to $E_{sp}(q-1, Q+1, A)$ and the crystal field splitting increases to $\Delta(q-1, Q+1, A)$. Using Eq. (17) one obtains

$$\begin{aligned} E_{VRBE}(q, Q, A) = & C(q, Q, A) + S(q, Q, A) \\ & + (Q+1)E_{sp}(q-1, Q+1, A) - QE_{sp}(q, Q, A) \\ & + \sum_{i=1}^{5} \big(\epsilon_i(q, Q, A) o_i(q, Q, A) \\ & - \epsilon_i(q-1, Q+1, A) o_i(q-1, Q+1, A)\big). \end{aligned} \tag{28}$$

Here we have assumed that the 18 electrons of the [Ar] configuration and the nucleus of charge Z have (apart from a minus sign) the same spherical interaction with the environment as a $3d$ electron. Below, the deviations from that assumption will be incorporated in the parameters β_{sp} and E_{cs} of the spherical interactions.

The $S(q, Q, A)$ part of Eq. (28) can be obtained when the Racah parameters B_r and C_r and spin–orbit parameter ζ_{dd} are experimentally available for all q of both TM^{Q} and TM^{Q+1} in the compound. Such a complete set of data is never available. When they are available for just one or a couple of TMs, one may establish the nephelauxetic ratios β_B and β_C. Assuming, the same ratios for each TM, the complete set can be generated from the free TM values in Table 4 to obtain $S(q, Q, A)$.

Next, we need to know how the spherical interaction energies $C(q, Q, A)$ will change in a chemical environment. For this, some assumptions will be made. The expressions for $W(q, Q)$, $V(q, Q)$, and $A_r(q, Q)$ deal with integrals containing $(R_{3d}(r))^2$ as argument. When Q decreases, the $R_{3d}(r)$ function expands and the energies W, V, and A_r decrease. This explains why the downward slope, *i.e.*, $a_1(Q)$ in Table 1, of the free-ion $C(q, Q, \mathrm{vac})$ curves in Fig. 2 becomes less steep when Q decreases from 4+ to 1+. The nephelauxetic effect in a chemical environment will have the same result. The decrease of W, V, and A_r due to the environment will reduce the downward slope of the $C(q, Q, A)$ curve. Since W, V, and A_r deal with spherical interactions, we have defined the spherical nephelauxetic ratio β_{sp} to express the reduction of W and $(V - A_r)$. Its value is expected to be strongly correlated with that of β_B and β_C.

With a reduction of the spherical interactions, the original $C(q, Q, \mathrm{vac})$ curve will move up by an amount $(C(1, Q, A) - C(1, Q, \mathrm{vac})) > 0$ and tilt counterclockwise. To incorporate such predicted changes, Eq. (28) is rewritten as

$$\begin{aligned} E_{VRBE}(q, Q, A) = & C(1, Q, \mathrm{vac}) + \beta_{sp}(Q, A)(C(q, Q, \mathrm{vac}) \\ & - C(1, Q, \mathrm{vac})) + S(q, Q, A) \\ & + E_{cs}(1, Q, A) + \sum_{i=1}^{5} \big(\epsilon_i(q, Q, A) o_i(q, Q, A) \\ & - \epsilon_i(q-1, Q+1, A) o_i(q-1, Q+1, A)\big). \end{aligned} \tag{29}$$

where $\beta_{sp}(Q, A) < 1$ acts as a tilt factor that tilts the $C(q, Q, \mathrm{vac})$ curve counterclockwise around $-W(1, Q, \mathrm{vac}) = C(1, Q, \mathrm{vac})$ at the start of the TM series.

The introduced chemical shift $E_{cs}(1, Q, A)$ in Eq. (29) has now been defined as

$$E_{cs}(1, Q, A) \equiv (Q+1)E_{sp}(q-1, Q+1, A) - QE_{sp}(q, Q, A) - (C(1, Q, A) - C(1, Q, \mathrm{vac})) \tag{30}$$

where the right-hand expression was obtained under the assumption that the electrons of the inner core [Ar] configuration and the nucleus have the same spherical interaction with the chemical environment as a $3d$ electron. Such an assumption may apply to lanthanides where the $4f$ electrons are inside the inner core [Xe] configuration, but for TMs where the $3d$ orbitals overlap with the ligands it will not be the case. The centroid shift ϵ_c of the $3d$ level energies is believed to be a result of this. Unfortunately, there is no means to establish how $E_{cs}(q, Q, A)$ depends on q, and we need to use a plausible approximation. Since many of the parameters scale linearly with q, we will assume the same for the chemical shift. Such a linear dependence can then be treated as part of the chosen value for β_{sp}, and $E_{cs}(q, Q, A)$ can be replaced with $E_{cs}(1, Q, A)$ as in Eq. (29).

The chemical shift as defined in Eq. (30) is obtained from the interaction of the TM with the environment before and after a $3d$ electron has been removed. This is different from Eq. (22) of the Chemical Shift model for the lanthanides. Here, chemical shift is the Coulomb repulsion of a single $4f$ electron from the screening charge $-Q$. A change of screening charge when a $4f$ electron is removed was overlooked in the Chemical Shift model. If the same is done for TMs then $E_{sp}(q-1, Q+1, A) = E_{sp}(q, Q, A) = 1440Q/R_Q(A)$. By further neglecting a nephelauxetic effect, Eq. (30) for the chemical shift of TMs becomes the same as Eq. (22) for the chemical shift of the lanthanides. If, on the other hand, the screening charge does increase to $Q+1$ with unaltered screening distance one obtains

$$E_{cs}(1, Q, A) = \frac{2Q+1}{R_Q}. \tag{31}$$

It predicts a linear increase with Q with about two times larger screening distance than with Eq. (22). Eq. (31) still neglects the contribution of the nephelauxetic effect and the centroid shift of the $3d^q$-levels to the chemical shift. This demonstrates that Eq. (22) and (31) are of limited value. Screening charge and distance are, nevertheless, valuable concepts for understanding the origin and magnitude of the chemical shift. We will use Eqs. (22) and (31) only to express the main trends.

This is a good moment to compare Eq. (29) with the expressions and ideas in the 1960s. Replacing $C(1, Q, \mathrm{vac})$ with $a_0(Q)$ and $C(q, Q, \mathrm{vac})$ with $a_0(Q) + (q-1)a_1(Q)$ from Table 1, one obtains the equation of the 1960s [14,19]

$$\begin{aligned} E_{VRBE}(q, Q, A) = & -\phi(Q, A) - (q-1)\eta(Q, A) + S(q, Q, A) \\ & + \sum_{i=1}^{5} \big(\epsilon_i(q, Q, A) o_i(q, Q, A) \\ & - \epsilon_i(q-1, Q+1, A) o_i(q-1, Q+1, A)\big). \end{aligned} \tag{32}$$

where $\eta(Q, A) \equiv -\beta_{sp}(Q, A)a_1(Q)$ tilts the $C(q, Q, \mathrm{vac})$ curve, and $-\phi(Q, A)$ is an energy that places the CTL energies relative to the valence band top. Both parameters were empirically chosen to reach the best

Table 6
The coefficients in the strong-field approximation of the [LS]-states for q = 4, 5, 6, 7 at octahedral coordinated sites. Corresponding electron configurations are provided. Coefficients within braces apply in the limit Δ=0 for the weak-field approximation.

q	TM^{2+}	TM^{3+}	TM^{4+}	[LS]	conf.	a_A	n_B	m_C
4	Cr	Mn	Fe	^3H $^3T_1$	t_{2g}^4	6	−15 (−17)	5 (4)
5	Mn	Fe	Co	^2I $^2T_2$	t_{2g}^5	10	−20 (−24)	10 (8)
6	Fe	Co	Ni	^1I $^1A_1$	t_{2g}^6	15	−30 (−29)	15 (13)
7	Co	Ni	Cu	^2G ^2E	$t_{2g}^6e_g$	21	−36 (−39)	18 (17)

agreement with the experiment. In the 1960s, a linear dependence of $C(q,Q,\text{vac})$ on $(q-1)$ was still an assumption. With the results in Table 1, that assumption is now confirmed for the TMs. Furthermore, in the treatment of this work $-\phi(Q,A) \equiv a_1(Q) + E_{cs}(1,Q,A)$, and all CTL energies are referred to the vacuum level. In the 1960s, the parameter $\eta(Q,A)$ was found to depend on Q and the nephelauxetic effect. The same will be established for $\beta_{sp}(Q,A)$ in this work.

$\beta_{sp}(Q,A)$ and $E_{cs}(1,Q,A)$ will turn out to be the most important parameters that determine the $E_{VRBE}(q,Q,A)$ energies within the bandgap of compounds and relative to the vacuum level. They provide the dominant trend. The experimentally accessible energies ϵ_i, B_r, C_r, and ζ_{dd} will then provide the variations in the CTL energies on top. $\beta_{sp}(Q,A)$ and $E_{cs}(1,Q,A)$ are to be determined from best reproducing the experimentally found CTL energies. Clear trends will emerge with the valence Q of the TM and the type of environment A.

5.6. CTL energies of the [LS] ground states

When $\Delta \equiv \epsilon_5 - \epsilon_1$ is smaller than the energy gained in spin alignment, every next electron until q = 5 is added with parallel spin to the next higher ϵ_i level to form the [HS] spin states. The coefficients n_B, m_C, and p_ζ in Table 2 or Table 5 are then used in Eq. (27). One may also encounter situations where $(\epsilon_i - \epsilon_1)$ becomes larger than the energy gained in spin alignment. In the case of octahedral coordination, nothing changes for q= 1, 2, and 3, but for q=4 the 4th electron is added with antiparallel spin to the t_{2g} state to form the [LS] t_{2g}^4 $^3T_1$ term with 2S+1=3 instead of 5, see Fig. 10. Fig. 12 shows the typical Tanabe–Sugano diagram for a d^4 TM at a site of octahedral point symmetry.

For small octahedral crystal field splitting or small Δ/B_r in Fig. 12, the high spin [HS] ^5E term emanating from the ^5D free-ion level with $t_{2g}^3e_g^1$ electron configuration forms the ground state. With an increase of Δ/B_r above ≈ 27, the $^3T_1$ term stemming from the free-ion ^3H excited state with t_{2g}^4 electron configuration moves below the ^5E term and becomes the ground state. The free-ion ^3H term energy is $6A_r - 17B_r + 4C_r$, and in the weak-field approximation one, therefore, should use n_B = −17 and m_C = +4 in Eq. (27) rather than the coefficients that apply for the ground state in Table 2. The coefficients in the strong-field approximation are n_B= −15 and m_C =+5. The coefficients can be found in *e.g.* Table 9.2 of [4]. Since the $^3T_1$ term appears 7 times in the Tanabe–Sugano diagram, we need to solve a 7 × 7 matrix to obtain the proper energy of the [LS] ground state. A similar treatment can be followed for q = 5, 6, and 7. The coefficients with A_r, B_r, and C_r for the [LS] states are compiled in Table 6 for the weak-field and strong-field approximation. For q = 8, 9, and 10, the filling of the t_g and e_{2g} orbitals will always be the same and there are no separate [LS] and [HS] possibilities.

For the [HS] ground states, we only had to solve a 2 × 2 matrix to obtain the term energies and the proper n_B coefficients for q = 2 and q = 7 with the solutions of Eqs. (25) and (26). For the [LS] ground states for q = 4 until 7, much larger matrices must be solved to obtain the term energies. This is not worthwhile, and since with [LS] states, one is usually dealing with large Δ, the coefficients of the strong-field approximation will be used in Eq. (27). Technically, the coefficient with the spin–orbit coupling parameter needs to be determined also. However, we will ignore the spin–orbit coupling when it concerns the [LS] states and take $p_\zeta = 0$ in this work.

In calculating the contribution $S(q,Q,A)$ to the CTL energy, one first needs to establish for the TM^Q and also for the TM^{Q+1} whether we are dealing with a [HS] or a [LS] ground state. Next, the appropriate coefficients a_A, n_B, and m_C in Tables 5 and 6 are to be used. In practice, the involvement of [LS] states will concern only a few individual TMs from the series, and only when crystal field splitting is large.

6. Examples of reconstructed transition metal CTL energies

Before starting the interpretation of the experimental and computed data on TM CTL energies, we will explore how β_{sp}, β_B, β_C, and ϵ_i affect the TM$^{Q+1/Q}$ CTL energies in a chemical environment calculated with Eq. (29). This will be done for octahedral coordination where $\epsilon_1 = \epsilon_2 = \epsilon_3 \equiv \epsilon_t = -0.4\Delta$ and $\epsilon_4 = \epsilon_5 \equiv \epsilon_e = 0.6\Delta$, and for tetrahedral coordination with $\epsilon_1 = \epsilon_2 \equiv \epsilon_e = -0.6\Delta$ and $\epsilon_3 = \epsilon_4 = \epsilon_5 \equiv \epsilon_t = 0.4\Delta$. The computed $B_r(q,Q,\text{vac})$ and $C_r(q,Q,\text{vac})$ values in Table 4 were multiplied by 0.8 to correct for a systematic difference with the experimental values. The values of $\zeta_{dd}(q,Q,\text{vac})$ in Table 4 were multiplied by 0.9. β_{sp} was chosen 0.5, and β_B, β_C, and β_ζ were always kept at the same value of 0.6. The chemical shift $E_{cs}(1,3+,A)$ was always 40 eV to bring the Ti^{3+} VRBE near −4 eV which is the typical value observed in compounds [75].

Fig. 13 shows reconstructed TM$^{4+/3+}$ CTL energies for the high spin [HS] states in an octahedral environment using the strong-field approximation. When q increases from 1 to 5, the first three electrons enter the t_{2g} orbital with aligned spin. Next, the e_g orbital is filled with two more electrons still aligned with those in t_{2g} to form the [HS] ground state. This repeats for q = 6 to 10 but now with antiparallel spin. Dashed curve (1) connects the TM$^{4+/3+}$ CTL energies in the absence of crystal field splitting ($\epsilon_i = 0$). The curve still resembles the free-ion CTL zigzag curve shape. The downward slope of the free-ion CTL curve is reduced by a factor of two due to β_{sp} = 0.5, and the jump between q = 5 and 6 is smaller due to the reduced β_C and β_B.

The solid curve (2) with solid triangle data symbols connects the resulting CTL energies when an octahedral crystal field splitting with $\Delta(3+,A) = \Delta(4+,A)$ = 2.2 eV is added. When an electron is removed from a t_{2g} state, the crystal field contribution $\sum_{i=1}^{5}\left(\epsilon_i(q,Q,A)o_i(q,Q,A) - \epsilon_i(q-1,Q+1,A)o_i(q-1,Q+1,A)\right)$ to the VRBE energy equals $\epsilon_t = \frac{-2}{5}\Delta$. This happens for q = 1, 2, 3, 6, 7, and 8. Otherwise, for q = 4, 5, 9, 10 when an electron is removed from a e_g state, the CTL energy increases by $\epsilon_e = \frac{3}{5}\Delta$. The original zigzag shape of curve (1) is now altered by the additional jumps due to crystal field splitting. Note that the jump between q = 5 and 6 has almost disappeared because it is reduced by $\Delta(3+,A)$ = 2.2 eV. The compound-to-compound variation in the size of the octahedral crystal field splitting will immediately reflect in a compound-to-compound variation in the CTL curve shape. The four open down-triangle data symbols for $q = 2,3,7,8$ are obtained using the coefficients from Table 2 that apply in the weak-field approximation. The VRBE in the V^{3+} ground state decreases, *e.g.*, by 0.26 eV because the coefficient n_B changes from −5 to −8. Unless explicitly mentioned, we will use Eqs. (25) and (26) to evaluate the n_B coefficient of the [HS] states. For [LS] states, the coefficients of the strong-field approximation in Table 6 will always be used.

In the above reconstruction, it was assumed that the $\epsilon_i(q,3+,A)$ are the same as the $\epsilon_i(q-1,4+,A)$ but in reality crystal field splitting is

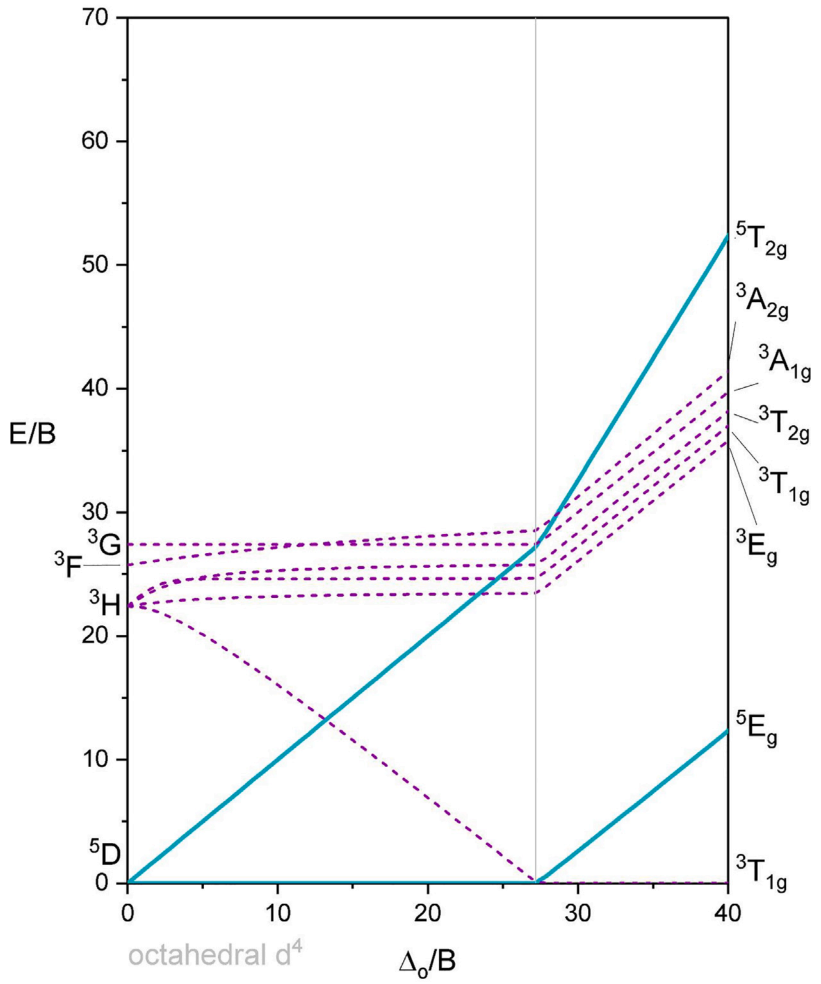

Fig. 12. Tanabe–Sugano diagram for the lowest energy levels of a d^4 transition metal at a site of O_h point symmetry pertaining to $C_r/B_r \approx 4$.
Source: Adapted from LibreTexts Chemistry [74].

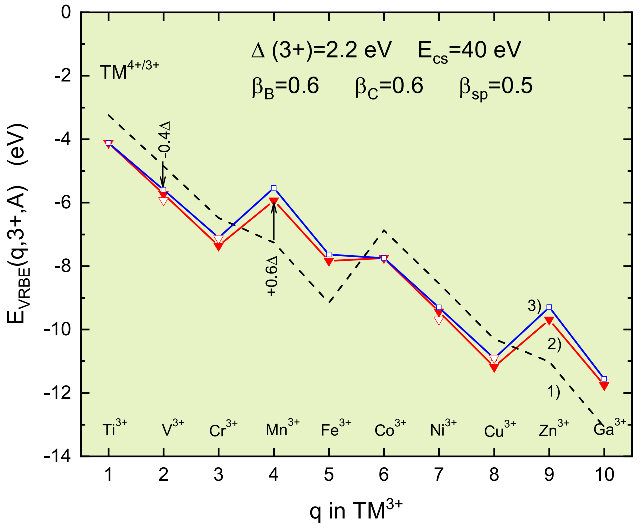

Fig. 13. Dashed curve (1) connects the TM$^{4+/3+}$ CTL energies in the absence of crystal field splitting but with chemical shift $E(1, 3+, A) = 40$ eV and nephelauxetic effect ($\beta_{sp} = 0.5$ and $\beta_B = \beta_C = \beta_\zeta = 0.6$ eV). Solid curve (2) connects the reconstructed TM$^{4+/3+}$ CTL energies in the strong-field approximation for transition metals with [HS] ground states at octahedrally coordinated sites with $\Delta(4+) = \Delta(3+) = 2.2$ eV. The open down-triangle data symbols would be obtained in the weak-field approximation. Solid curve (3) shows the effect when $\Delta(4+) = 1.15 \times \Delta(3+)$. The chemical shift was chosen so that the Ti$^{4+/3+}$ CTL energy is near −4 eV.

expected to increase upon removing an electron from $3d^q$. One may write

$$\epsilon_i(q-1, Q+1, A) = (1 + \gamma(Q))\epsilon_i(q, Q, A) \tag{33}$$

with $\gamma(Q)$ a positive quantity. To take a change in crystal field splitting into account, and assuming that crystal field splitting and level energies are independent of q, Eq. (29) becomes

$$\begin{aligned} E_{VRBE}(q, Q, A) =& C(1, Q, \text{vac}) + \beta_{sp}(Q, A)(C(q, Q, \text{vac}) \\ & - C(1, Q, \text{vac})) + S(q, Q, A) \\ & + E_{cs}(1, Q, A) + \sum_{i=1}^{5} \epsilon_i(Q, A)\Delta o_i \\ & - \gamma(Q) \sum_{i=1}^{5} (\epsilon_i(Q, A) o_i(Q+1, A)) \end{aligned} \tag{34}$$

where $\Delta o_i \equiv o_i(Q, A) - o_i(Q+1, A)$ is the change in occupation of level $\epsilon_i(Q, A)$, *i.e.*, $\Delta o_i = 1$ when an electron is removed from level $\epsilon_i(Q, A)$. Note that in Eq. (34), the variables q and $q-1$ have been removed from the ϵ_i and o_i. One may encounter situations where two electrons are removed from one level ($\Delta o_i = 2$) and one electron added to another. However, always, $\sum_{i=1}^{5} \Delta o_i = 1$ and $\sum_{i=1}^{5} o_i(Q+1, A) = q-1$. Solid curve (3) in Fig. 13 is obtained with $\gamma(3+) = 0.15$. For $q = 1$ and 6, the results remain the same as in curve (2), but for other q the VRBE increases by a few 0.1 eV.

Curve (1) in Fig. 14 shows the same [HS] CTL curve in the strong-field approximation as curve (2) in Fig. 13 with $\gamma(3+) = 0$. Suppose

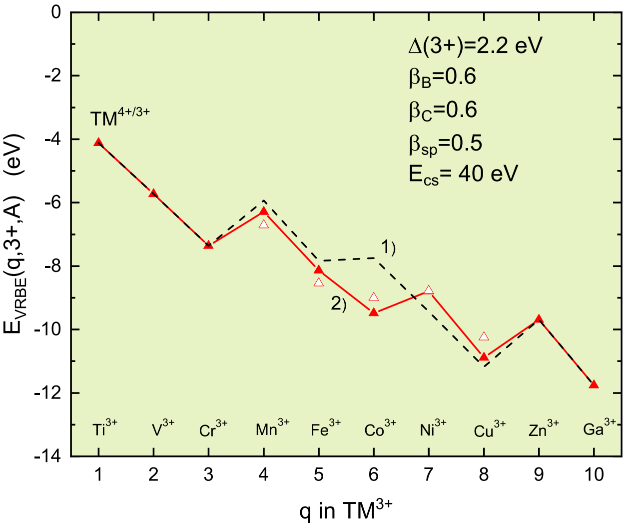

Fig. 14. Dashed curve (1) connects the $TM^{4+/3+}$ CTL energies using the strong-field approximation for TMs with [HS] ground states at octahedral coordinated sites. Solid curve (2) connects the same when dealing before and after ionization with [LS] ground states whenever possible. Open triangle data symbols are CTL energies obtained using the weak-field approximation. The contribution from spin–orbit coupling to the energy was ignored for the [LS] states.

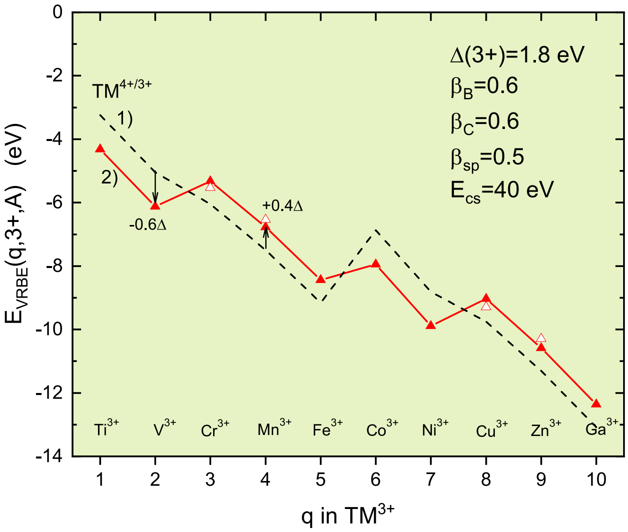

Fig. 15. Dashed curve (1) connects the $TM^{4+/3+}$ CTL energies in the absence of a crystal field splitting but with chemical shift and nephelauxetic effect. Solid curve (2) connects the typical $TM^{4+/3+}$ CTL energies using the strong-field approximation for TMs with [HS] ground states at tetrahedrally coordinated sites. The open data symbols would be obtained in the weak-field approximation with Δ approaching zero. The chemical shift was chosen so that the $Ti^{4+/3+}$ CTL energy is near −4 eV.

now that the octahedral crystal field splitting is larger than the energy gained in spin alignment. The first six electrons will enter the t_{2g} orbital and the last four the e_g-orbital. Rather than a [HS] ground state we deal for $q = 4$, 5, 6, and 7 with a [LS] ground state. This changes the CTL energies. We now have to use the n_B and n_C coefficients of the strong-field approximation in Table 6 for Mn^{3+}, Fe^{3+}, Co^{3+}, and Ni^{3+}. After ionization, we use the same coefficients for Fe^{4+}, Co^{4+}, Ni^{4+}, and Cu^{4+}. For Cu^{3+} before and Mn^{4+} after ionization, the [HS] coefficients of Table 5 are to be used. We therefore deal with a [LS]→[HS] $Mn^{4+/3+}$ CTL, a [LS]→[LS] CTL for Fe, Co, and Ni, and with a [HS]→[LS] CTL for $Cu^{4+/3+}$. Curve (2) shows the resulting CTL energies. For $q = 1$, 2, 3, 9, and 10 the result is not different from curve (1). The jump between $q = 3$ and 4 in curve (1) is caused by the crystal field splitting. However, in curve (2) it is caused by the loss in energy from the antiparallel alignment of the fourth electron spin in the t_{2g} level. Here, they are of similar magnitude.

The open triangle data symbols in Fig. 14 are obtained when the coefficients in Table 6 belonging to the weak-field approximation are used. CTL energies may differ ≈ 0.5 eV from the CTL energies of the strong-field approximation along curve (2).

In principle, one may encounter situations where the preference for occupying the [HS] state over the [LS] state depends on q and it may also change upon oxidation or reduction. For example, Co^{3+} in the t_{2g}^6 [LS] (s=0) ground state can be reduced to Co^{2+} in the $t_{2g}^5 e_g^2$ and $t_{2g}^4 e_g^3$ mixed [HS] (s=3/2) state. Such coupled electron transfer and spin cross-over are widespread in chemistry and biology [76,77].

Eq. (34) can equally well be used when the TM occupies a tetrahedral site with T_d point symmetry creating lower e and upper t_2 states. The crystal field splitting for TMs on tetrahedral sites is always much smaller than on octahedral sites, and the [HS] configuration has usually the lowest energy. Now, the first two electrons are added to e_g and the following three to t_{2g} to form the [HS] states, and this repeats for $q = 6$ to 10. Since the Tanabe–Sugano diagram for a d^q TM subject to tetrahedral crystal field splitting will be the same as that for the d^{10-q} TM subject to octahedral crystal field splitting, one now needs to solve a 2 × 2 matrix for $q = 3$ and $q = 8$ to find the proper CTL energies. Expressions similar to those of Eq. (25) and (26) apply, and in the strong-field approximation coefficient $n(B)$ becomes −12 for $q = 3$ and −47 for $q = 8$. Using these coefficients and $\Delta(3+) = \Delta(4+) = 1.8$ eV but for the rest the same parameter values as in Fig. 13, the CTL curve (2) in Fig. 15 is obtained. Crystal field splitting lowers the CTL energy by -3/5Δ for $q = 1$, 2, 6, and 7. It increases the CTL energy by +2/5Δ for $q = 3$, 5, 6, 8, 9, and 10. The open triangle data symbols are obtained in the weak-field approximation. As in Fig. 13 the effect on the CTL will be at most several 0.1 eV.

The above reconstructed CTL energies all relate to high point symmetry sites. In principle, Eq. (34) also applies to low point symmetry sites but this will generate many practical difficulties. It will not be trivial to experimentally determine the five energies ϵ_i for TMs with more than one electron in $3d$. One also must perform a complicated analysis to obtain the energies of the ${}^{2S+1}\Gamma$ representations. At best, one can make fair estimates for the chemical shift $E_{cs}(1, Q, A)$ and the downward slope of the CTL curve given by β_{sp}.

7. Experimental CTL data with reconstructed CTL energies

We will collect experimental data to derive CTL energies or VRBEs, and next use Eq. (34) to reconstruct those energies. For that, information is needed on the values of Racah parameters B_r, C_r, and the crystal field energies ϵ_i. One also has to assess whether one is dealing with [LS] or [HS] states before and after removing an electron from the TM.

The method on how to obtain CTL energies from experimental or computed data relative to the vacuum level is presented first. This is followed by information on how Eq. (34) will be used to best reconstruct the obtained CTL energies. Finally, the VRBE diagrams of 18 compounds and environments are presented that collect all information. The relations between the reconstruction parameters used and the conclusions therefrom are treated in the discussion section.

7.1. The method followed to derive experimental CTL energies

Fig. 16 illustrates the method to obtain the $D^{Q+1/Q}$ CTL energy relative to the vacuum level where the defect D is a lanthanide or a TM. The right-hand side shows the VB→D^{Q+1} electron transfer process in a configuration coordinate diagram. From point A at the VB-top, an electron is excited to point B on the charge transfer (CT) parabola (b), and D^{Q+1} is reduced to D^Q leaving a VB-hole h_{VB}. The energy for this

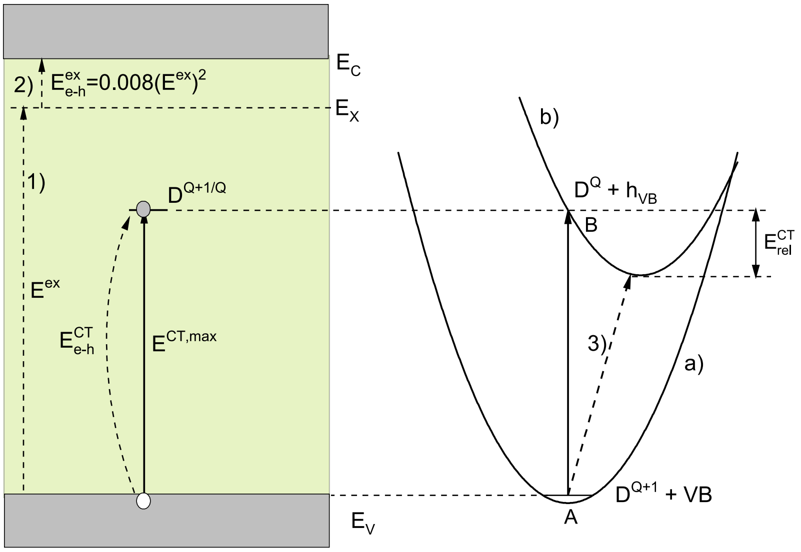

Fig. 16. Illustration of how lattice relaxation and electron–hole binding in the charge transfer states are accounted for in establishing CTL energies from VB→TM^{Q+1} electron transfer data.

transition is given by the energy $E^{CT,max}$ at the maximum of the CT-band observed in absorption or luminescence excitation spectra. The energy at point B might be regarded as equivalent to the binding energy in the D^Q ground state relative to the VB-top. However, this method disregards that the hole at the VB-top resides on the anion ligands that surround D, and therefore still Coulomb bonded with an energy $E^{CT}_{e-h}(D^Q,A)$ to the transferred electron. It also disregards the lattice relaxation that follows the electron transition. It decreases the energy with $E^{CT}_{rel}(D^Q,A)$. One may write, in the case that our defect D is a $3d^q$ transition metal,

$$E_{VRBE}(q,Q,A) = E_V(A) + E^{CT,max}(q-1,Q+1,A) + E^{CT}_{e-h}(\mathrm{TM}^Q,A) - E^{CT}_{rel}(\mathrm{TM}^Q,A). \qquad (35)$$

To determine $E_V(A)$ at the VB-top, the Chemical Shift model [78] in combination with lanthanide spectroscopy will occasionally be used. That method has already provided E_V and E_C energies for several 100s of different compounds [79–81]. First, the energy difference $U(A)$ between the ground states of Eu^{3+} and Eu^{2+} in the environment A as defined in Fig. 6 must be determined. Next, the Eu$^{3+/2+}$ CTL energy or $E_{VRBE}(\mathrm{Eu}^{2+})$ is obtained with Eq. (23). The energy $E^{CT,max}(\mathrm{Eu}^{3+},A)$ at the maximum of the VB→Eu^{3+} electron transfer band is then used to establish E_V with

$$E_V(A) = E_{VRBE}(\mathrm{Eu}^{2+}) - E^{CT,max}(\mathrm{Eu}^{3+},A) - (E^{CT}_{e-h}(\mathrm{Eu}^{2+},A) - E^{CT}_{rel}(\mathrm{Eu}^{2+},A)). \qquad (36)$$

By adding the host exciton creation energy $E^{ex}(A)$ to the VB-top, see arrow (1) in Fig. 16, the VRBE $E_X(A)$ in the exciton state is reached. By adding the electron–hole binding energy $E^{ex}_{e-h}(A)$ of the exciton, see arrow (2), the bottom of the conduction band or mobility edge $E_C(A)$ is reached [78]. The electron–hole binding energy will be estimated as $0.008\times(E^{ex})^2$ as proposed by Dorenbos [82].

$E^{CT}_{e-h}(\mathrm{Eu}^{2+},A)$ in the CT state is expected to be of similar magnitude as $E^{ex}_{e-h}(A)$ in the exciton state that varies from 0.8 eV in wide-band-gap oxides to values around 0.1 eV in semiconductors. $E^{CT}_{rel}(\mathrm{Eu}^{2+},A)$ is of similar magnitude as the typical 0.7–0.8 eV width (FWHM) of VB→Eu^{3+} CT-bands [53]. The idea, as outlined and motivated in [53], is that the energy involved in lattice relaxation more or less cancels against the energy needed to delocalize the hole on neighboring anions into the VB, *i.e.*, $E^{CT}_{e-h}(\mathrm{Eu}^{3+},A) - E^{CT}_{rel}(\mathrm{Eu}^{3+},A) \approx 0$. One may then use the energy $E^{CT,max}(\mathrm{Eu}^{3+},A)$ to derive E_V with Eq. (36). This method has proven to be quite successful in establishing the lanthanide CTL energies relative to the vacuum level in 5 to 12 eV wide-bandgap compounds.

The obtained E_V and E_C form the basis for establishing the TM$^{(Q+1)/Q}$ CTL energy or TM^Q VRBE from the observed VB→TM^{Q+1} electron transfer band energy or the TM^Q→CB electron transfer band energy. As for the Eu^{3+} CT, we will assume throughout this work that $E^{CT}_{e-h}(\mathrm{TM}^Q,A) - E^{CT}_{rel}(\mathrm{TM}^Q,A) \approx 0$. The experimental energy $E^{CT,max}(q-1,Q+1,A)$ then provides the TM$^{(Q+1)/Q}$ CTL energy above the VB-top. An analogous reasoning applies to TM^Q→CB electron transfer. The electron will be located on the cations surrounding the TM where it is still bonded to the hole left behind on the TM^{Q+1}. Therefore, for both types of localized transitions, we will use the energy $E^{CT,max}(q-1,Q+1,A)$ to place the TM$^{Q+1/Q}$ CTL in the bandgap of the compound.

The situation is different when it concerns CTL data derived from photocurrent measurements on TM^Q→CB or VB→TM^{Q+1} transitions. Rather than a localized transition, the transport of delocalized electrons in the CB or delocalized holes in the VB is probed. In those cases, there is no need to correct for e-h Coulomb attraction. In such a case, we will use the onset energy of the photocurrent to place the TM$^{Q+1/Q}$ CTL in the bandgap. The energy difference between the onset and the maximum is then regarded as equivalent to E^{CT}_{rel}. Occasionally data from thermoluminescence studies will be used. An electron from TM^Q is thermally excited to the CB. It transports through the CB to eventually recombine with a hole to generate luminescence. One deals with the transport of a delocalized electron; again, there is no need to correct it for e-h bonding. There is also no need to correct for lattice relaxation since with thermal excitation, the CT ends in the relaxed energy state as indicated with arrow (3) in Fig. 16. The trap depth derived from the TL-glow peak is then used to provide the CTL energy below the CB-bottom. This was confirmed with a recent study on lanthanide TL data covering 37 different compounds by Dorenbos [83]. The electron trapping depth determined from TL glow curves agreed well with predictions from the lanthanide CTL locations in constructed VRBE schemes.

7.2. Method of VRBE diagram and CTL energy reconstruction

Data on transition metals that can be used to derive CTL energies relative to the VB-top, the CB-bottom, the SHE potential, or the vacuum level have been gathered from the archival literature. Since we wish to reproduce the entire $3d^q$ CTL curve, we will only treat compounds where data on several members of the TM-sequence are available. For each compound, CTL energies are converted into energies relative to the vacuum level and will be displayed in a vacuum-referred binding energy diagram.

In a recent study, it was shown that the bandgap, the Eu^{3+} CT-energy, and CTL energies shift with temperature at a typical rate of 5×10^{-4} eV/K [84]. Room temperature (RT) data will be used to construct the VRBE diagrams presented in this work. If there are no RT data available, the RT data have been extrapolated from the data taken at other temperatures. The VRBE diagrams will contain the top of the valence band, the exciton level, the bottom of the conduction band (mobility edge), and data on the TM CTL energies. An account of how E_V, E^{ex}, and E_C were obtained is provided with the references in the Supplementary Information.

Next, the $TM^{Q+1/Q}$ CTL curve is reconstructed with Eq. (34). The values for the free ion TM^Q and TM^{Q+1} Racah parameters B_r and C_r, and ζ_{dd} from Table 4 were used, and the four nephelauxetic parameters $\beta_B(q,Q,A)$, $\beta_C(q,Q,A)$, $\beta_\zeta(q,Q,A)$, $\beta_{sp}(Q,A)$, the crystal field splitting $\Delta(q,Q,A)$, and the chemical shift $E_{cs}(1,Q,A)$ were chosen so that good agreement is obtained with the experimental CTL data.

$\Delta(q,Q,A)$, $\beta_B(q,Q,A)$, and $\beta_C(q,Q,A)$ can be derived from the spectroscopy of the $3d^q \rightarrow 3d^q$ transitions of TM^Q in the environment A with the Tanabe–Sugano diagrams. Sometimes such information is available for one or several TMs but also often not, and fair estimates must be made. In applying Eq. (34) we will ignore a q dependence of the reconstruction parameters, and use $\Delta(Q,A)$, $\beta_B(Q,A)$, $\beta_C(Q,A)$, $\beta_{sp}(Q,A)$, and $\beta_\zeta(Q,A)$. Since the contribution of spin–orbit coupling to the CTL energy will be small, we will not treat it as a free parameter but always choose $\beta_\zeta = \beta_C$. The spin–orbit coupling will be ignored when dealing with [LS] states. $\beta_{sp}(Q,A)$ and $E_{cs}(1,Q,A)$ cannot be determined experimentally and will be chosen so that the reconstructed CTL energies show good agreement with the available data.

We know experimentally that the $5d^1$ crystal field splitting for Ce^{3+} is 1.3 times larger than that for Eu^{2+} when both lanthanides are located at the same site. This indicates that $\gamma(2+) \approx 0.3$ in Eq. (33) for the lanthanides. Similar behavior appears for the TMs. A continuous increase of $\Delta_{oct}(Q,A)$ when Q increases is reported for several $3d^3$ TM^Q in Al_2O_3 [85,86], *i.e.*, it is 1.7 eV for V^{2+}, 2.07 eV for Cr^{3+}, and 2.60 eV for Mn^{4+}. For Cr^{3+}, Mn^{4+}, and Fe^{5+} in $SrTiO_3$, $\Delta_{oct}(Q)$ ≈2.04 eV, ≈ 2.26 eV, and ≈ 2.50 eV, respectively [87]. Computations on the crystal field splitting of Mn^{2+}, Mn^{3+}, and Mn^{4+} at tetrahedral sites in SiO_2 and $Y_3Al_5O_{12}$ also reveal an increase with Q [11].

The observed increase of $\Delta(Q,A)$ when Q increases applies to situations of a fully relaxed lattice around the TM^Q dopant. One may question to what extent this will be the case when, upon removal of an electron from $3d^q$, the TM valence changes from Q to Q+1. All electrons in the compound have instantaneously adapted to the new situation but the atoms need time to relax to a new equilibrium. Therefore, crystal field splitting is expected to increase upon removing an electron but possibly not to the full extent. In order not to ignore the expected increase in crystal field splitting we have chosen to use $\gamma(1+) = 0.25$, $\gamma(2+) = 0.2$ and $\gamma(3+) = 0.15$ in all reconstructed $TM^{2+/1+}$, $TM^{3+/2+}$, and $TM^{4+/3+}$ CTL energies of this work.

It is known experimentally, and it will be further confirmed in this work, that the nephelauxetic effect increases, and hence $\beta_B(Q,A)$ and $\beta_C(Q,A)$ decrease with the increase of Q. Again we do not wish to introduce too many parameters and we will assume $\beta(Q+1,A) = (1-\delta(Q,A))\beta(Q,A)$ where $\delta(Q,A)$ is a positive quantity. In this work, we will choose $\delta(Q,A) = 0.1$.

7.3. Results on 18 different chemical environments

7.3.1. Magnesium fluoride

In MgF_2 with the rutile structure, the coordination at the Mg^{2+} site is distorted octahedral with D_{2h} point symmetry. Computations by Jing et al. [10] show that in MgF_2, the ground states of TM^{2+} and TM^{3+} are of [HS] character, which means that the coefficients from Table 5 with Eq. (25) for $q = 2$ and Eq. (26) for $q = 7$ apply. The three experimental data points for Mn, Fe, and Co are obtained from absorption band maxima at room temperature from Sabatini et al. [47]. The bands are attributed to the transition from TM^{2+} to a hybridized state that is a mixture of the host Mg 3*s*-conduction band state and the TM^{2+} $3d^{q-1}4s$ state [47]. The dashed curve (2) is obtained from computed VB→TM^{3+} charge transfer energies from Jing et al. [10] when added to the VB-top energy at −12.8 eV. The dashed curve (3) is obtained when the computed TM^{2+}→CB photo-ionization energies in Jing et al. [10] are subtracted from the CB-bottom energy at +0.15 eV.

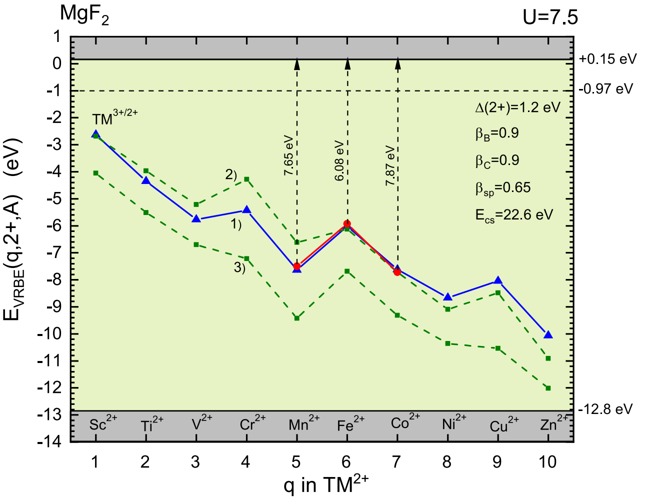

Fig. 17. Solid bullet data symbols, $TM^{3+/2+}$ CTL energies in MgF_2 based on experimental data on TM^{2+}→CB or $3d^q \rightarrow 3d^{q-1}4s$ transition energies. Solid curve (1) connects reconstructed CTL energies obtained assuming [HS] ground states. Dashed curve (2) is derived from computed VB to TM^{3+} CT energies in [10]. Dashed curve (3) is derived from computed TM^{2+} to the CB photo-ionization energies in [10].

For V^{2+} in MgF_2, Sturge et al. [88] report $\Delta(2+) = 1.43$ eV and $\beta_B \approx \beta_C \approx 0.9$. Smaller values of $\Delta(2+)$ around 0.8–0.9 eV are reported [89,90] for Co^{2+} and Ni^{2+} which suggests a dependence on q. Curve (1) in Fig. 17 connects the reconstructed $TM^{3+/2+}$ energies using $\Delta(2+) = 1.2$ eV. β_{sp} was chosen so that the CTL curve runs down at about the same pace as the computed CTL curves (2) and (3) in Fig. 17. Finally, $E_{cs}(1, 2+, MgF_2)$ was chosen to obtain good overlap with the three experimental data points for Mn, Fe, and Co is obtained.

Note that the CTL energies derived from computed photo-ionization (PI) energies of TM^{2+} by Jing et al. [10] (curve (3) are different from those derived from computed VB→TM^{3+} CT energies (curve 2). The chemical shift for the CT data along curve (2) is about 1.5 eV larger than for the PI data along curve (3). It may indicate a systematic error in the computed data, perhaps related to how lattice relaxation is accounted for.

7.3.2. Potassium magnesium fluoride

$KMgF_3$ has the perovskite crystal structure with octahedrally coordinated Mg^{2+} sites that can be occupied by TMs. Studies on V^{2+}, Cr^{2+}, Mn^{2+}, Fe^{2+}, Co^{2+}, and Ni^{2+} identified absorption bands caused by exciting an electron from the $3d^q$ ground state to the conduction band or to the $3d^{q-1}4s$ TM^{2+} states [47,50]. The latter assignment was preferred by McClure [50]. The data have been used in Fig. 18 to provide the experimental CTL energies below the CB-bottom at −0.25 eV. Here we implicitly assumed that the transitions are to a hybridized CB state with the $3d^{q-1}4s$ state near the CB-bottom.

Sabatini et al. [47] on V^{2+}, Cr^{2+}, Mn^{2+}, Fe^{2+}, Co^{2+}, and Ni^{2+} reported values for $\Delta(2+)$ ranging from 1.5 eV for $3d^3$ V^{2+} and $3d^4$ Cr^{2+} and decreasing to 0.9 eV for $3d^8$ Ni^{2+}. Here we used a constant value of 1.4 eV. Racah B_r values were reported [47,88,91] for V^{2+}, Mn^{2+}, Fe^{2+}, Co^{2+}, and Ni^{2+}. The $\beta_B(2+)$ derived therefrom is always close to 0.9. From Sturge et al. [88], $\beta_C(2+)$=0.86 can be derived for V^{2+}. In the reconstructed CTL curve computed with Eq. (34), similar β_B and

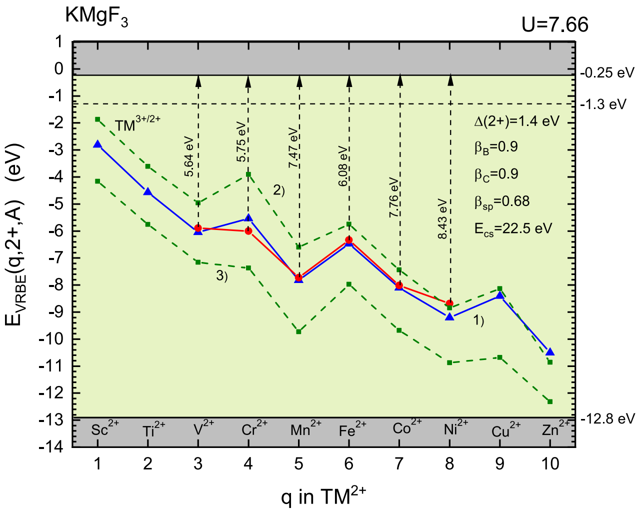

Fig. 18. Solid bullet data symbols, TM$^{3+/2+}$ CTL energies in $KMgF_3$ based on experimental data on TM^{2+}→CB or $3d^q \rightarrow 3d^{q-1}4s$ transition energies. Solid curve (1) connects reconstructed CTL energies obtained assuming [HS] ground states. Dashed curve (2) is derived from computed CT energies from the VB to TM^{3+} in [10]. Dashed curve (3) is derived from computed photo-ionization energies from TM^{2+} to the CB in [10].

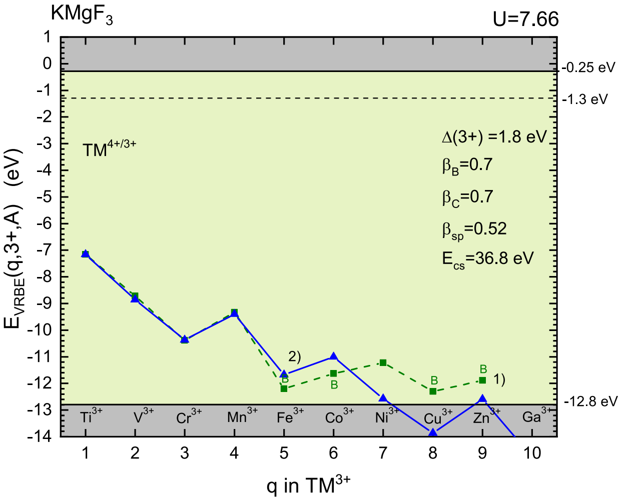

Fig. 19. Dashed curve (1) are computed TM$^{4+/3+}$ CTL energies in $KMgF_3$ from [10]. Data labeled with B are so-called Bader states. Solid curve (2) connects reconstructed TM$^{4+/3+}$ CTL energies obtained assuming [HS] ground states with the parameters chosen to reproduce the computed values for q=1 to 4.

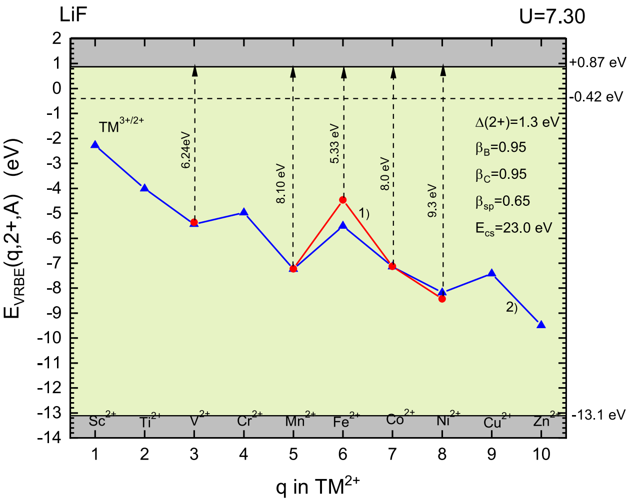

Fig. 20. Curve (1) and solid bullet data symbols, TM$^{3+/2+}$ CTL energies in LiF based on experimental data on TM^{2+}→CB or $3d^q \rightarrow 3d^{q-1}4s$ transition energies. Solid curve (2) connects reconstructed CTL energies obtained assuming [HS] ground states.

β_C were chosen. β_{sp} was again chosen so that the CTL curve runs down at about the same pace as the computed CTL curves (2) and (3) in Fig. 18, and $E_{cs}(1,2+,KMgF_3)$ was chosen so that good overlap with the experimental data is obtained. The data for Cr^{2+} and Ni^{2+} still appear to deviate somewhat. According to computations in [10], Ni^{3+} should have the [HS] ground state configuration, and the deviating Ni$^{3+/2+}$ CTL energy is therefore not explained by a [HS] to [LS] conversion upon removal of a 3d electron.

The experimental, reconstructed, and also computed CTL energies in Fig. 18 are quite similar to those for MgF_2 in Fig. 17. As in MgF_2, the Sc$^{3+/2+}$ CTL energy is predicted near −2.7 eV which is consistent with the findings in Rogers and Dorenbos [92]. In that work, the VRBE in the Sc^{2+} ground state at 13 different sites in 12 different oxides was found to range between −1.8 eV and −3 eV. The chemical shift for the computed CTL energies (2) is about 2 eV larger than for curve (3), *i.e.*, similar as for MgF_2. Note also that for both compounds the energy steps between q = 3 and 4 and between q = 8 and 9 for curves (2) based on VB→TM^{3+} CT are larger than for curves (3) based on TM^{2+}→CB photo-ionization transitions.

Jing et al. [10] also computed the TM$^{4+/3+}$ CTL energies in $KMgF_3$. They are shown as curve (1) in Fig. 19. The data labeled with the letter B are computed to be so-called Bader states. When an electron is removed, rather than the $3d^{q-1}$ configuration, the $3d^q$ configuration together with a hole localized on the neighboring anions is formed. Such states tend to form whenever the CTL is close to the VB-top. The reconstructed CTL energies, assuming [HS] configurations are shown along curve (2). Parameters were chosen so that the first 4 computed CTL energies are well reproduced. Comparing the parameter values with those for the TM$^{3+/2+}$ CTL curve in Fig. 18, one may notice that the nephelauxetic ratios for the TM$^{4+/3+}$ CTL curve are significantly smaller and that for Δ and E_{cs} significantly larger. In treating other compounds, we will consistently observe such a phenomenon when the valence increases, and in the discussion section it will be related to the amount of screening charge around the TM.

7.3.3. Lithium fluoride

The energies for $3d^q \rightarrow 3d^{q-1}4s$ transitions at room temperature of the divalent TMs V^{2+}, Mn^{2+}, Fe^{2+}, Co^{2+}, and Ni^{2+} in LiF were reported by Chase et al. [93] and they pertain to room temperature. Here we assume that the $3d^{q-1}4s$ orbital is hybridized with the bottom of the CB of LiF, and in that case, the energies provide the TM$^{3+/2+}$ CTL energies below E_C as shown in Fig. 20.

Chase et al. report Δ(V^{2+})=1.53 eV and Δ(Ni^{2+})=1.01 eV. We used Δ(2+)=1.3 eV to reconstruct the CTL curve through the experimental data. To better reproduce the large step in CTL energy between q = 5 and q = 6, one would need to select values for β_B and β_C around 1.05 which seems odd, and we kept the values below 1 at 0.95. Possibly, the experimental data point for Fe$^{3+/2+}$ is not correct because Chase et al. were not sure about the interpretation of the absorption bands for Fe^{2+}.

7.3.4. Sodium fluoride

The energies for $3d^q \rightarrow 3d^{q-1}4s$ transitions of V^{2+}, Mn^{2+}, Co^{2+}, and Ni^{2+} in NaF at RT were reported by Chase et al. [93]. Here we assume like with LiF that the $3d^{q-1}4s$ orbital is hybridized with the bottom of the CB of NaF, and in that case, the energies provide the TM$^{3+/2+}$ CTL energies below E_C as shown in Fig. 21.

Δ(2+)=1.2 eV was chosen somewhat smaller than that for LiF because Na$^+$ is larger than Li$^+$ and crystal field splitting tends to decrease

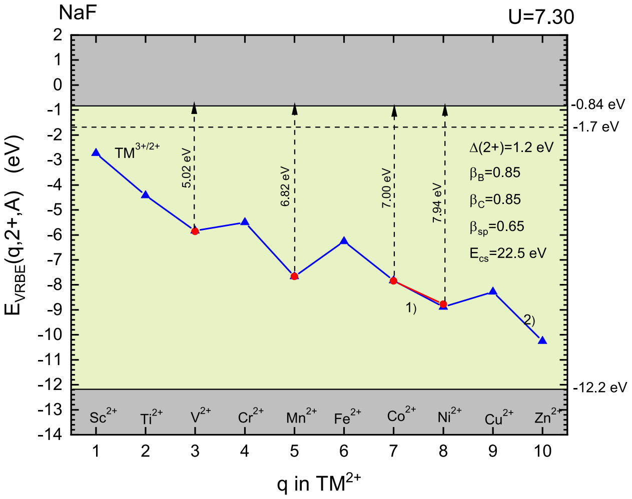

Fig. 21. Curve (1) and solid bullet data symbols, $TM^{3+/2+}$ CTL energies in NaF based on experimental data on $TM^{2+}\rightarrow CB$ or $3d^q\rightarrow 3d^{q-1}4s$ transition energies. Solid curve (2) connects reconstructed CTL energies obtained assuming [HS] ground states.

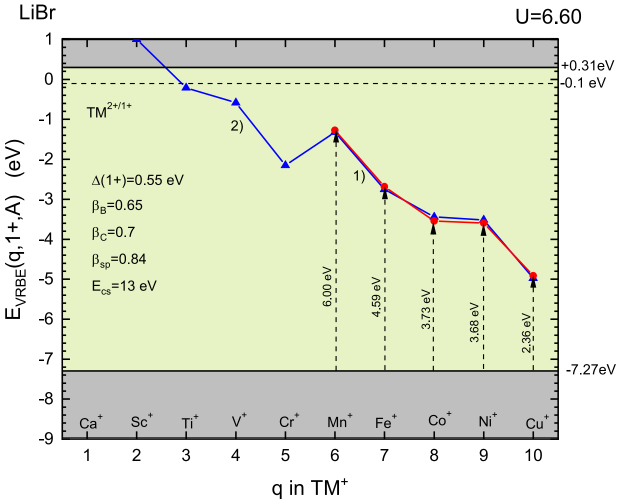

Fig. 23. Solid bullet data symbols along curve (1), $TM^{2+/1+}$ CTL energies in LiBr based on experimental data on $VB\rightarrow TM^{2+}$ transition energies. Solid curve (2) connects reconstructed CTL energies obtained assuming [HS] ground states.

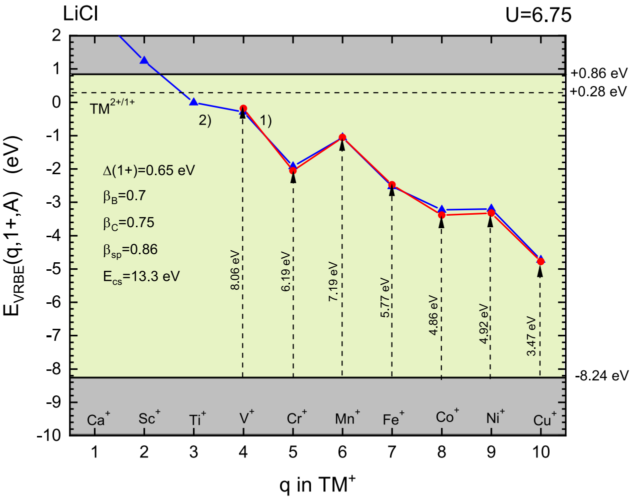

Fig. 22. Solid bullet data symbols along curve (1), $TM^{2+/1+}$ CTL energies in LiCl based on experimental data on $VB\rightarrow TM^{2+}$ transition energies. Solid curve (2) connects reconstructed CTL energies obtained assuming [HS] ground states.

with larger site size. The other parameter values used to reconstruct the CTL curve through the experimental data are not too much different from those used for the $TM^{3+/2+}$ CTL energies in LiF.

7.3.5. Lithium chloride

The experimental energies for the $VB\rightarrow TM^{2+}$ electronic transition reported by Simonetti et al. [94] and later by Hirako et al. [95] provide the TM^{1+} VRBE energies from V^+ until Cu^+ in LiCl as shown along curve (1) in Fig. 22. Hirako et al. report values around 0.8 and 0.9 eV for the octahedral crystal field splitting $\Delta(2+)$ for Fe^{2+}, Co^{2+}, and Ni^{2+}. Crystal field splitting tends to decrease with smaller Q, and a lower value for $\Delta(1+)$ is to be expected for the monovalent TMs. To reconstruct curve (2) in Fig. 22, $\Delta(1+) = 0.65$ eV was used.

7.3.6. Lithium bromide

The spectroscopy of TM^{2+} in LiBr appears very similar to that of TM^{2+} in LiCl. There is one main difference, *i.e.*, the values for the $VB\rightarrow TM^{2+}$ CT-band energies are systematically ≈ 1.2 eV smaller. This is caused by an about 1 eV higher VRBE at the VB-top of LiBr as compared to LiCl as has been established from XPS and UPS studies by Poole et al. [96]. In addition, the crystal field splitting for Fe^{2+} and Co^{2+} appears about 0.1 eV smaller [95] due to the longer TM to anion bond lengths in LiBr. We therefore used a 0.1 eV lower value for $\Delta(1+)$ in the reconstruction of the CTL curve (2) in Fig. 23.

A trend is now starting to emerge in the chemical shift. We had $E_{cs}(1,3+,\mathrm{KMgF}_3) = 36.8$ eV when $Q = 3+$, $E_{cs}(1,2+,A) \approx 23$ eV for various fluorides when $Q = 2+$, and $E_{cs}(1,1+,A) \approx 13$ eV for LiCl and LiBr when $Q = 1+$. The chemical shift decreases almost proportionally or linearly with decreasing Q as expressed by Eq. (22) of the Chemical Shift model for the lanthanides and with Eq. (31) derived in this work for the TMs. We now find that the concept is again similar, *i.e.*, the charge of a transition metal of valence $Q+$ is screened by a negative charge $-Q$ from the environment which leads to a chemical shift that is almost proportional with Q.

7.3.7. Cadmium chloride

Unfortunately, there is no information on lanthanide spectroscopy in $CdCl_2$, and the energy at the VB-top cannot be obtained from the Chemical Shift model. E_V for $CdBr_2$ is estimated the same as in $CsCdBr_3$ which, using the Chemical Shift model, is found at -6.8 eV. Assuming the same VB-top energy difference as between LiCl and LiBr, one may estimate $E_V(CdCl_2) \approx -7.8$ eV.

The energies needed for CT from the VB of $CdCl_2$ to Fe^{2+}, Co^{2+}, and Ni^{2+} were reported by Coutts et al. [49], and they provide the corresponding $TM^{2+/1+}$ CTL energies above the VB-top as shown in Fig. 24. The energies of CT to Cu^{2+} were obtained from Payne et al. [97]. Ackerman et al. [98] studied Ni^{2+} and found $\Delta(Ni^{2+},CdCl_2)$=0.89 eV. Ramirez-Serrano et al. [99] report $\Delta(Mn^{2+}, CdCl_2)$=0.77 eV. Since crystal field splitting decreases with lower valence and with longer bond lengths, $\Delta(1+,CdCl_2) = 0.6$ eV was chosen to reconstruct the CTL curve in Fig. 24.

The reconstructed CTL curve (2) in Fig. 24, reproduces the experimental CTL energies for $q = 7$ until 10 very well. Note that those for q=4 until 6 are not experimentally known. The VRBEs of the corresponding monovalent TMs are predicted inside the CB or for Cr^+ closely below the CB-bottom. In these cases, the TM^+ will spontaneously oxidize by auto-ionization. In other words, the TM^+ valence is not stable.

7.3.8. Cadmium bromide

As for $CdCl_2$, there is no information on lanthanide spectroscopy in $CdBr_2$, and the energy at the VB-top cannot be obtained from

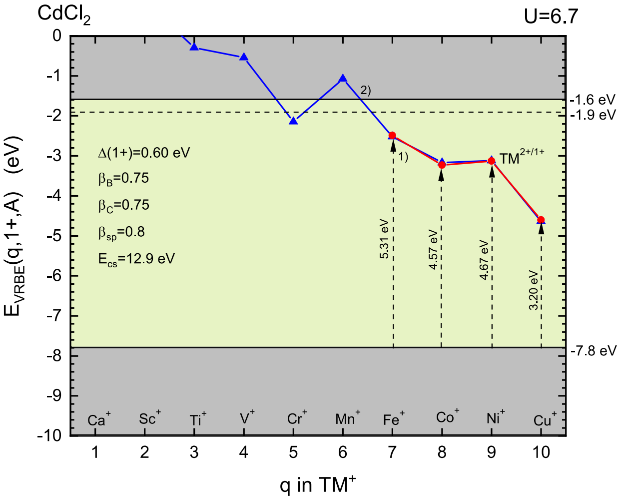

Fig. 24. Solid bullet data symbols along curve (1), TM$^{2+/1+}$ CTL energies in CdCl$_2$ based on experimental data on VB→TM^{2+} transition energies. Solid curve (2) connects reconstructed CTL energies obtained assuming [HS] ground states.

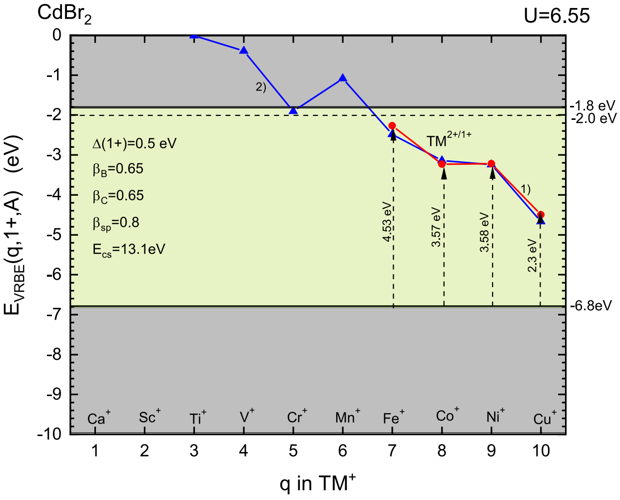

Fig. 25. Solid bullet data symbols along curve (1), TM$^{2+/1+}$ CTL energies in CdBr$_2$ based on experimental data on VB→TM^{2+} transition energies. Solid curve (2) connects reconstructed CTL energies obtained assuming [HS] ground states.

the Chemical Shift model. However, there is information for CsCdBr$_3$ yielding the VB-top at −6.8 eV. The same value is assumed for CdBr$_2$. The energies needed for CT from the VB to Fe^{2+}, Co^{2+}, and Ni^{2+} were reported by Coutts et al. [49], and they provide the corresponding TM$^{2+/1+}$ CTLs above the VB-top as shown in Fig. 25. The energy for CT to Cu^{2+} was obtained from Payne et al. [97]. Ackerman et al. [98] studied Ni^{2+} and report Δ(Ni^{2+}, CdBr$_2$)=0.79 eV. The situation in CdBr$_2$ is similar to CdCl$_2$. The main difference is the ≈ 1 eV smaller VB→TM^{2+} CT-energies in CdBr$_2$ that is, like for LiCl and LiBr, attributed to a higher energy VB-top in CdBr$_2$. The reconstructed CTL curve (2) in Fig. 25 was made to match well with the experimental data using parameters with 0.1 eV smaller $\Delta(1+)$ and 0.1 smaller β_B and β_C than for CdCl$_2$.

7.3.9. Aluminium oxide

Al$_2$O$_3$ provides slightly distorted octahedral coordinated Al^{3+} sites with C_3 point symmetry that can be occupied by TM^{3+} cations. The early work of McClure [46] and Tippins [48], which identified $3d^q \rightarrow 3d^q$ internal transitions and VB→TM^{3+} CT transitions, is still our most important source of experimental data on TM$^{3+/2+}$ CTL energies.

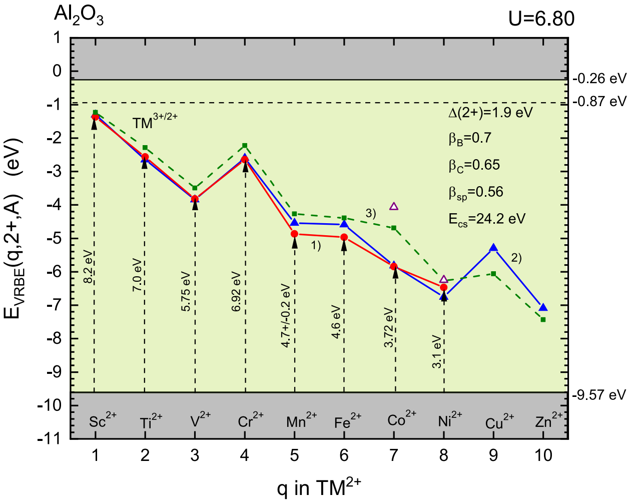

Fig. 26. Closed bullet data symbols along curve (1), TM$^{3+/2+}$ CTL energies in Al$_2$O$_3$ based on experimental data on VB→TM^{3+} charge transfer energies. Solid line (2), reconstructed CTL energies assuming [HS] ground state configurations. The two open triangle data symbols for Ni and Co are the reconstructed CTL energies assuming [LS] states for the TM^{3+} using the strong-field approximation. Dashed curve (3), connects the CTL energies derived from computed VB→TM^{3+} CT-energies in [10].

The CT energies for Ti^{3+}, Cr^{3+}, and Fe^{3+} are confirmed in later reports [100–102]. For Sc^{3+} we used a CT energy of 8.2 eV from Kirm et al. [103]. The value of 4.7±0.2 for Mn^{3+} is an estimate based on the onset of the VB→Mn^{3+} absorption near 4.35 eV in McClure et al. [46]. By adding the CT energies to the VRBE of −9.57 eV at the VB-top in Al$_2$O$_3$, the TM$^{3+/2+}$ CTL energies are obtained as shown along curve (1) in the VRBE diagram of Fig. 26.

The reconstructed CTL energies along curve (2) follow the experimentally obtained data reasonably well. Jing et al. [10] performed a computational study on the $3d^q$ TMs in Al$_2$O$_3$. They found that all divalent and most trivalent TMs adopt the [HS] electron configuration in the ground state. Only Co^{3+} and Ni^{3+} adopt the [LS] configuration. The computed values for the VB→TM^{3+} CT energies were used to construct the dashed CTL curve (3) in Fig. 26. Apart from Co$^{3+/2+}$, the computed data follow those along curve (1) and curve (2). The open triangle data points for the Co$^{3+/2+}$ and Ni$^{3+/2+}$ CTL energies are obtained with Eq. (34) assuming a [LS]→[HS] conversion when an electron is added. For Ni$^{3+/2+}$, the CTL has moved up and coincides with the computed value along curve (3). For Co$^{3+/2+}$, the CTL energy has moved to above the computed value along curve (3). In the reduction of Co^{3+} with [LS] t_{2g}^6 configuration to Co^{2+} with [HS] $t_{2g}^5 e_g^2$ configuration, two electrons are added to e_g and one removed from t_{2g}. This makes the Co$^{3+/2+}$ CTL energy quite sensitive to $\Delta(2+)$. The experimentally derived CTL energy for Co$^{3+/2+}$ appears to agree better with a [HS]→[HS] conversion (see curve (2) than with a [LS]→[HS] conversion (see curve 3).

Fig. 27 shows the TM$^{4+/3+}$ CTL data in Al$_2$O$_3$. CT transitions from the VB-top to Ti^{4+} from [104–106], V^{4+} from [107], and Mn^{4+} from [108,109] provide the three experimental data points. That for Ti$^{4+/3+}$ is uncertain because different CT values are reported. We have added information, see arrow (a) in Fig. 27, on the photo-ionization threshold of Ti^{3+} from Basun and co-workers [104,110] placing the Ti$^{4+/3+}$ CTL about 4.7 eV below the CB-bottom which is consistent with the information from VB→Ti^{4+} CT data.

The VB to TM^{4+} CT energies were computed by Jing et al. [10] and the resulting CTL energies are shown along dashed curve (3). When the TM$^{4+/3+}$ CTL energy is close to the VB-top, TM^{3+} plus a hole localized on surrounding anions is computed to be more stable than TM^{4+}. Those situations are marked with the letter B. The same phenomenon was encountered for the TM$^{4+/3+}$ CTL energies in KMgF$_3$

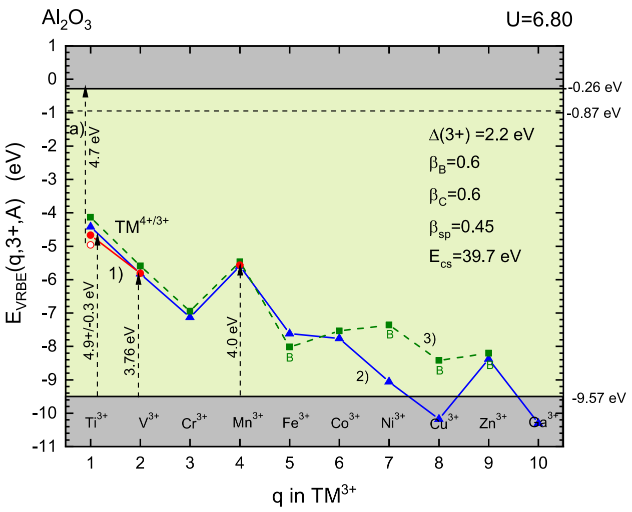

Fig. 27. Closed bullet data symbols along curve (1), $TM^{4+/3+}$ CTL energies in Al_2O_3 based on experimental data on VB→TM^{3+} charge transfer energies. The open-bullet data symbol for Ti is based on the photo-ionization threshold. Solid curve (2), reconstructed CTL energies assuming [HS] ground state configurations. Dashed curve (3), CTL data and curve from computed VB to TM^{4+} CT energies, and from computed Bader state energies in [10]. The Bader states are labeled with the letter B.

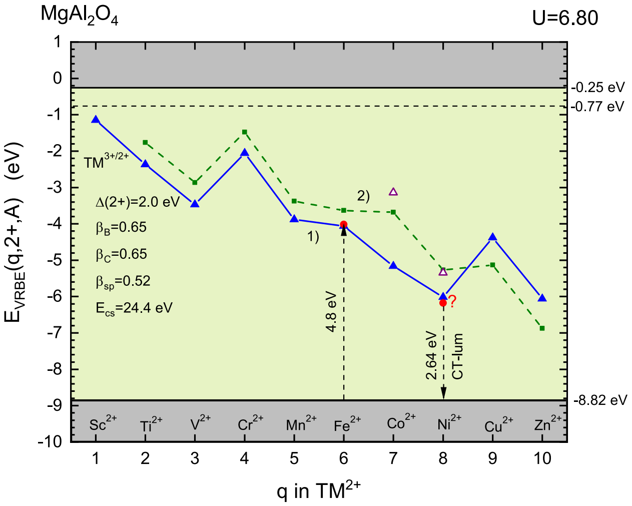

Fig. 28. Closed data symbols, $TM^{3+/2+}$ CTL energies on the octahedral sites in $MgAl_2O_4$ based on experimental data on charge transfer energies. Solid curve (1) connects reconstructed CTL energies assuming [HS] ground state configurations. For Ni and Co, also the reconstructed values assuming [LS] states for the TM^{3+} are shown using the strong-field approximation. Dashed line (2), CTL curve from computed CT energies to TM^{3+} in [10].

in Fig. 19. The computed CTL energies up to $Mn^{4+/3+}$ agree well with the three experimental energies. These experimental CTL energies determine the parameters used to reconstruct CTL curve (2). The crystal field splitting of $\Delta(3+) = 2.2$ eV is based on values of ≈ 2.2 eV determined from $3d^q$-$3d^q$ spectroscopy for Ti^{3+}, V^{3+}, Cr^{3+}, Mn^{3+}, Fe^{3+}, and Co^{3+} in [19,46,105,111,112]. It is responsible for the energy step between $q = 3$ and 4. The chemical shift $E_{cs}(1, 3+, Al_2O_3)$ appears 2.9 eV higher than for $KMgF_3$ in Fig. 19.

7.3.10. Magnesium aluminium oxide

The spinel structure of $MgAl_2O_4$ provides octahedral coordinated Al^{3+} and tetrahedrally coordinated Mg^{2+} sites. Computations by Jing et al. [10] yield for the octahedral sites that, just like in Al_2O_3, the t_{2g}^6 and $t_{2g}^6 e$ configurations form the [LS] ground states in Co^{3+} and Ni^{3+}.

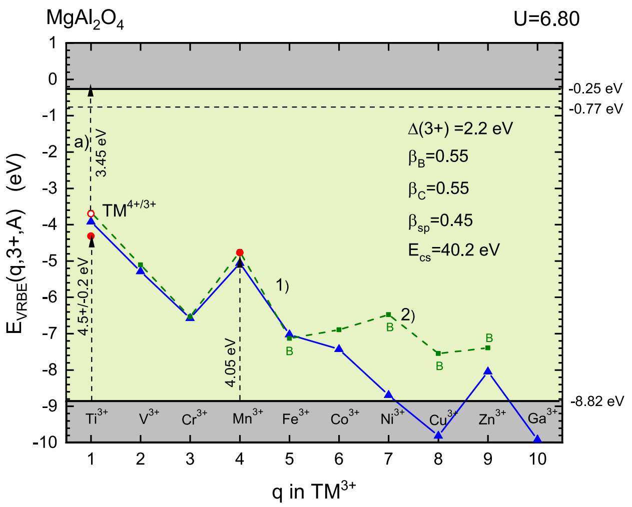

Fig. 29. Closed-bullet data symbols, $TM^{4+/3+}$ CTL energies on the octahedral sites in $MgAl_2O_4$ based on experimental data on VB→TM^{4+} charge transfer energies. The open-bullet data symbol for Ti is based on the photo-ionization threshold. Solid curve (1) connects reconstructed CTL energies assuming [HS] ground state configurations. Dashed line (2), CTL curve from computed CT energies to TM^{4+} in [10]. Data symbols labeled with the letter B indicate that those are Bader states.

All other TM^{3+} and all TM^{2+} have [HS] ground states. Fig. 28 shows two experimental data points. The 4.8 eV VB→Fe^{3+} CT-band energy is from White et al. [113] and seems reliable. Izumi et al. [54] observe for Ni^{3+} doped $MgAl_2O_4$ a 2.64 eV emission band attributed to Ni^{2+}→h_{VB} charge transfer luminescence. The unknown Stokes shift between CT absorption and CT luminescence must be added to arrive at the $Ni^{3+/2+}$ CTL energy above the VB-top.

The dashed curve (2) in Fig. 28 connects the computed CTL energies. The solid curve (1) connects the CTL energies reconstructed with Eq. (34). Reconstruction parameters were chosen so that the reconstructed curve (1) follows the shape of the computed curve (2) and passes through the experimental $Fe^{3+/2+}$ CTL energy. The open triangle data symbols for $Co^{3+/2+}$ and $Ni^{3+/2+}$ CTL energies are obtained when a [LS]→[HS] conversion is assumed when an electron is added. The results strongly resemble those for Al_2O_3. Here $\Delta(2+)$=2.0 eV was used to reproduce the energy step between $q = 3$ and 4 in curve (2). The energy step between $q = 8$ and 9 along curve (2) is much smaller than along curve (1). This suggests that $\Delta(2+)$ at the end of the TM series is smaller than at the beginning. $\Delta(2+) = 1.29$ eV for Ni^{2+} reported by Kuleshov et al. [114] may confirm this suggestion.

Fig. 29 shows the $TM^{4+/3+}$ CTL energies in $MgAl_2O_4$. Data on VB→Ti^{4+} from [54,115,116] and Mn^{4+} from [117] provide the two experimental CTL energies. Arrow (a) is the 3.45 eV onset of one-step photo-ionization of Ti^{3+} from Wong et al. [118] that provides the $Ti^{4+/3+}$ CTL reasonably consistent with that from the CT-band. Dashed line (2) shows the $TM^{4+/3+}$ CTL energies as computed By Jing et al. [10] where the data labeled with B are again Bader states as in Fig. 27. Parameter values were chosen so that the reconstructed CTL energies agree with the computed CTLs for $q = 1$ until 5. $\Delta(3+) = 2.2$ eV was needed to reproduce the step between $q = 3$ and 4. It is in line with values of 2.53 eV reported in [115] for Ti^{3+} and 2.25 eV reported in [54] for Cr^{3+}, and it is 10% larger than $\Delta(2+)$ in Fig. 28.

7.3.11. Yttrium aluminium garnet

The garnet structure provides both tetrahedral and octahedral Al^{3+} sites. Usually, particularly when it concerns the relatively large ionic radius TMs, the octahedral site is occupied. The desired valence of the TM can often be controlled by a co-dopant. For example, the tetravalent co-dopant Si^{4+} can be used to stabilize TM^{2+}, and a divalent co-dopant like Mg^{2+} to stabilize TM^{4+}. Here, we will focus on VB→TM^{4+} and

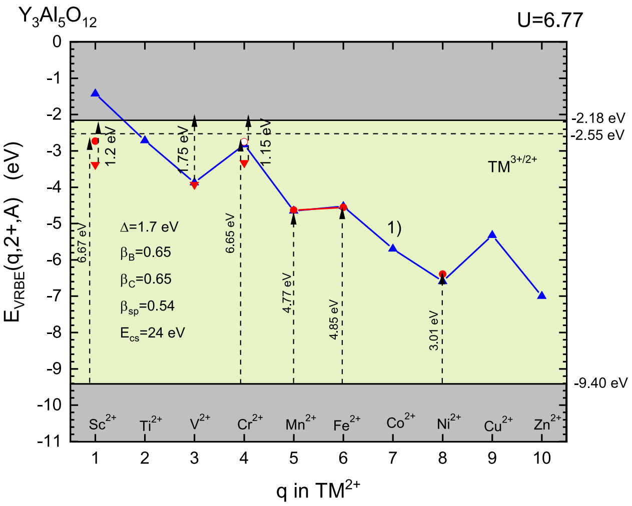

Fig. 30. Solid bullet data symbols, TM$^{3+/2+}$ CTL energies in $Y_3Al_5O_{12}$ based on experimental data on VB→TM^{3+} charge transfer energies. Solid down triangle data symbols, CTL energies based on e-trap depths from thermoluminescence studies. The open data symbol for Cr$^{3+/2+}$ is from computational studies in [8]. Solid curve (1) connects reconstructed CTL energies assuming [HS] ground state electron configurations. All data refer to the octahedral Al^{3+} site of the garnet structure.

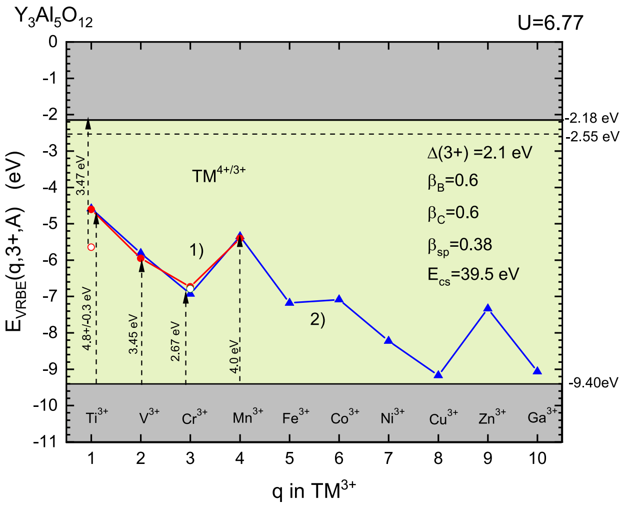

Fig. 31. Solid bullet data symbols with curve (1), TM$^{4+/3+}$ CTL energies in $Y_3Al_5O_{12}$ based on experimental data on VB→TM^{4+} charge transfer energies. The open data symbol for Ti$^{4+/3+}$ is from the one-step photo-ionization threshold of Ti^{3+}. The open data symbol for Cr$^{4+/3+}$ is from computational studies. Solid curve (2) connects reconstructed CTL energies assuming [HS] ground state configurations. All data refer to the octahedral Al^{3+} sites of the garnet structure.

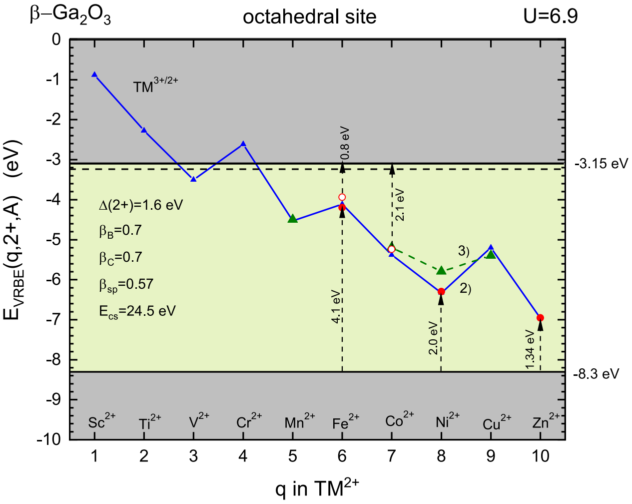

Fig. 32. Solid and open bullet data points are TM$^{3+/2+}$ CTL energies on the octahedral sites in β-Ga_2O_3 derived from experimental data. Solid curve (2) connects the reconstructed CTL energies for the [HS] ground state configurations. Dashed curve (3) connects the TM$^{3+/2+}$ CTL energies as computed in [11].

VB→TM^{3+} CT at the octahedral sites. Data were already collected by Qu et al. [56]. We used and reanalyzed those data and added more.

Fig. 30 shows the experimentally determined TM$^{3+/2+}$ CTL energies at the octahedral Al^{3+} sites in $Y_3Al_5O_{12}$ together with the reconstructed CTL curve (1). A 6.67 eV excitation band for Sc^{3+} reported in [119] was used for the Sc$^{3+/2+}$ CTL data point. CT data are also available for Mn^{3+} in [120], Fe^{3+} in [121,122] and Ni^{3+}in [123]. Ueda et al. [124,125] and also Li et al. [126] reported on thermoluminescence (TL) studies on $Y_3(Al_{5-x}Ga_x)O_{12}$:Ce^{3+} co-doped with Sc^{3+}, V^{3+}, and Cr^{3+}. Ce^{3+} acts as a hole-trapping and recombination center, and the TM acts as an electron-trapping center. The temperature at the maximum of the TL-glow peak provides the electron trap depth with the method of [83]. Employing a frequency factor $s = 1.7 \times 10^{13}$ Hz, trap depths of 1.2 eV, 1.75 eV, and 1.15 eV are obtained. Those were used to establish the CTL energies as shown in Fig. 30. Computations by Lafargue-Dit-Huaret et al. [8] locate the Cr$^{3+/2+}$ CTL energy 6.65 eV above the VB-top.

A value of 1.7 eV was used for $\Delta(2+)$ in the reconstruction of CTL energies along curve (1) in Fig. 30. The Sc$^{3+/2+}$ CTL energy appears more than 1 eV below the reconstructed value. This suggests that instead of the Sc^{2+} $3d^1$ state, a Sc^{3+} trapped exciton state is the final state. Apart from Sc$^{3+/2+}$, the reconstructed CTL curve follows the available experimental data reasonably well.

The derived TM$^{4+/3+}$ CTL energies are shown in Fig. 31. VB→TM^{4+} CT energies are available for the first four TM^{4+} of the series. The 4.8 ± 0.3 eV for the CT to Ti^{4+} from Huang et al. [127] places the Ti$^{4+/3+}$ CTL energy about 2.5 eV below the CB-bottom. However, Wong et al. [118] report a one-step photo-ionization threshold for Ti^{3+} of 3.47 eV that places the Ti$^{4+/3+}$ CTL energy at almost 1 eV lower energy. The reason for the difference is not known. The CTL energies for V$^{4+/3+}$, Cr$^{4+/3+}$, and Mn$^{4+/3+}$ are based on VB→ TM^{4+} CT band energies from [107,120,128,129]. The Cr$^{4+/3+}$ CTL energy derived from computations by Lafargue-Dit-Huaret et al. [8] is the same as derived from the CT band energy.

The choice of 2.1 eV for the crystal field splitting $\Delta(3+)$ was based on the ≈ 2.1 eV splitting for Ti^{3+} and V^{3+} in [127,130,131], the 2.0 eV splitting for Cr^{3+} from [132,133], and the ≈ 2.4 eV splitting reported for Mn^{3+} from [120,134]. Compared to the TM$^{3+/2+}$ CTL curve parameters, the nephelauxetic parameters are smaller, and $\Delta(3+)$ and the chemical shift are larger. The same was observed for $KMgF_3$, Al_2O_3, and $MgAl_2O_4$. Its common origin will be discussed in the discussion section.

7.3.12. Gallium oxide

β-phase Ga_2O_3 provides tetrahedral and octahedral Ga^{3+} sites. Fig. 32 compiles the data on the TM$^{3+/2+}$ CTL energies at octahedral sites. Data from Mn until Cu along the dashed curve (3) are from computational studies by Jing et al. [11].

Based on electron trapping and de-trapping studies involving Fe^{3+}, the Fe$^{3+/2+}$ CTL energy is found at 0.8 eV below the CB-bottom [135–137]. The value agrees reasonably with the computed value. A similar location is obtained when the ≈ 4.1 eV Fe^{3+} related absorption band in β-Ga_2O_3 as reported by Zade et al. [138] is assigned to the VB→Fe^{3+} transition. Analysis of temperature-dependent resistivity measurements between 800 and 1000 K by Seyidov et al. [136] places the Co^{2+} VRBE at 2.1 eV below the CB that agrees with the computed data point. The

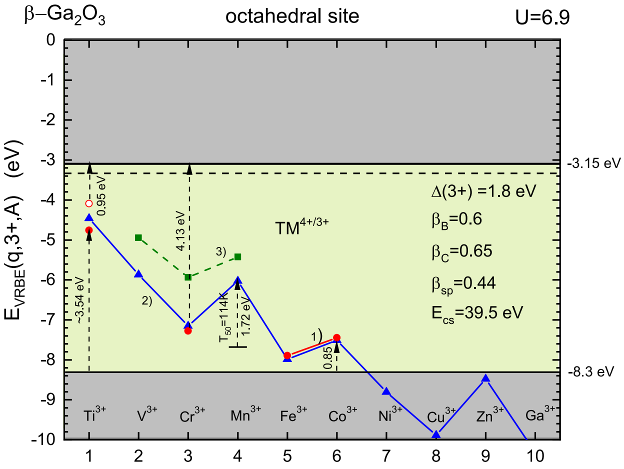

Fig. 33. Solid and open bullet data points with curve (1), $TM^{4+/3+}$ CTL energies derived from experimental data. Solid curve (2) connects reconstructed CTL energies for the [HS] ground state configurations. Dashed curve (3) connects $TM^{4+/3+}$ CTL energies in Ga_2O_3 as computed in [11] for the octahedral sites.

$Ni^{3+/2+}$ CTL energy is reported at 2.0 eV above the VB-top in [139]. Data on $Zn^{3+/2+}$ are from Jesenovec et al. [140].

The reconstructed CTL curve (2) reproduces the experimental and computed CTL energies well. It predicts that the VRBE energies for Sc^{2+} to Cr^{2+} are inside, or for V^{2+} slightly below, the CB. Then, these divalent TMs are not stable which explains why data were not found.

Fig. 33 shows the $TM^{4+/3+}$ CTLs for the octahedral sites in β-Ga_2O_3. The $Ti^{4+/3+}$ CTL energy is obtained from the ≈ 3.54 eV VB→Ti^{4+} CT energy observed by Zade et al. [138] in optical absorption, and the 0.95 eV trap depth from deep-level transient spectroscopy by Zimmermann et al. [141]. The $Cr^{4+/3+}$ CTL energy is derived from a 4.13 eV thermoluminescence excitation band [142]. We also added the $Fe^{4+/3+}$ CTL energy at 0.3–0.4 eV above the VB-top suggested by Ingebrigtsen et al. [137], and the $Co^{4+/3+}$ CTL energy at 0.85 eV above the VB-top suggested by Seyidov et al. [136].

Curve (2) shows the reconstructed CTL curve. In Jing et al. [11], the CTLs for $V^{4+/3+}$, $Cr^{4+/3+}$, and Mn $^{4+/3+}$ were computed, and they are ≈ 1 eV above the experimental data and the reconstructed CTL curve (2) for yet unknown reasons. Mn^{4+} emits at 720 nm (1.72 eV) with a decay time constant of 0.74 ms. The luminescence intensity has decreased by 50% at T_{50} = 114 K [143]. This low quenching temperature is consistent with the $Mn^{4+/3+}$ CTL energy on curve (2). The emitting Mn^{4+} excited state when viewed in the so-called hole-picture [144] is 0.7 eV above the VB-top. Such a small energy difference makes the emission prone to thermal quenching via hole ionization into the VB [81].

7.3.13. Magnesium oxide

MgO has the rocksalt crystal structure with octahedral Mg^{2+} sites. Experimental and computational data are available for deriving $TM^{2+/1+}$, $TM^{3+/2+}$, and $TM^{4+/3+}$ CTL energies. Fig. 34 shows information on $TM^{2+/1+}$ CTL energies.

For Fe^{2+} in MgO, Hansler and Segelken [145] assigned a strongly rising absorption at ≈ 6.7 eV to the VB→Fe^{2+} charge transfer transition. For Ni^{2+}, a distinct absorption band at 6.28 eV was assigned to VB→Ni^{2+} CT by Blazey [146]. Data from Stoneham et al. [147] provide the CT energy of 5.89 eV for Co^{2+}. Stoneham and co-workers [147,148] also provided a theoretical analysis of the available CT energies in MgO.

In Fig. 34, the experimentally derived CTL energies for the three TMs are shown along curve (1). With only three CTL energies, of which $Fe^{2+/1+}$ has a large uncertainty, the choice of parameters for reconstruction with Eq. (34) becomes rather ambiguous. We have chosen

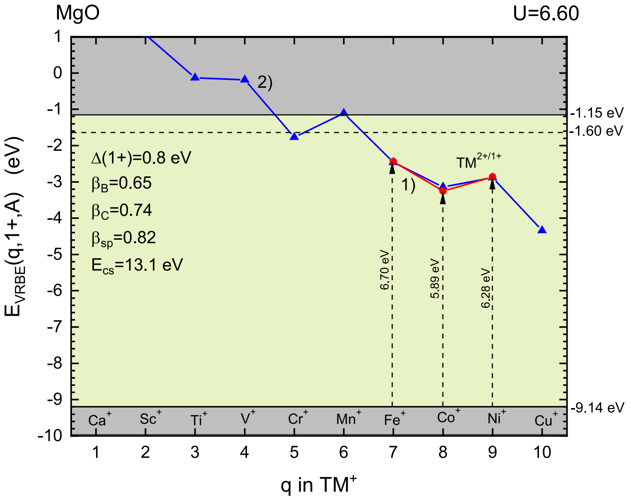

Fig. 34. Solid bullet data symbols along curve (1), $TM^{2+/1+}$ CTL energies in MgO based on experimental VB→TM^{2+} CT data. Solid curve (2) connects reconstructed CTL energies for the [HS] ground state configurations.

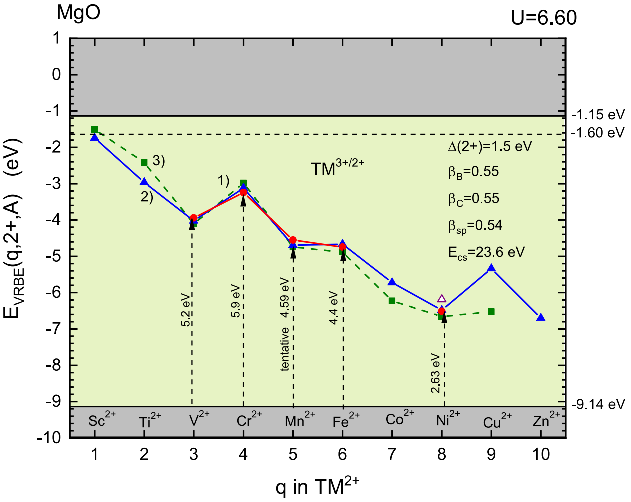

Fig. 35. Solid bullet data symbols along curve (1), $TM^{3+/2+}$ CTL energies in Mg connects CTL energies reconstructed for the [HS] ground state electron configurations. The open triangle data point pertains to the [LS] electron configuration of $Ni^{3+/2+}$. Dashed curve (3) connects the $TM^{3+/2+}$ CTL energies based on computed CT energies in [10].

$E_{cs}(1,1+,\mathrm{MgO})$=13.1 eV which is about the average of the values for LiBr, LiCl, $CdBr_2$, and $CdCl_2$ treated above. The crystal field splitting of $\Delta(1+)$=0.8 eV is in line with expectations based on $\Delta(Co^{2+}) = 1.1$ eV in [19,149] and $\Delta(Ni^{2+}) = 0.9$ eV in [19]. Although a slightly different set of parameters may generate an equally valid $TM^{2+/1+}$ CTL curve (2) in Fig. 34, the CTL curve predicts that the VRBE energies for the $3d^q$ TM^+ with q = 1 to 6 are located above or just below the CB. The monovalent state cannot be stable which explains why there is no data for those monovalent TMs. If this is the case, then the assignment of a 270 nm (4.59 eV) band to the VB→Mn^{2+} charge transfer in ceramic MgO by Kato et al. [150] is probably not correct.

Fig. 35 shows data on $TM^{3+/2+}$ CTL energies in MgO. Experimental data on CT from the VB-top to TM^{3+} are available for V^{3+} in [151], Cr^{3+} in [152], Fe^{3+} in [153–155], and Ni^{3+} in [156]. The data provide the $TM^{3+/2+}$ CTL energies as shown along curve (1) in Fig. 35. CTL energies were also computed by Jing et al. [10], and those are shown along the dashed curve (3). Selecting suitable parameter values, the CTL energies have been reconstructed using Eq. (34) assuming [HS]

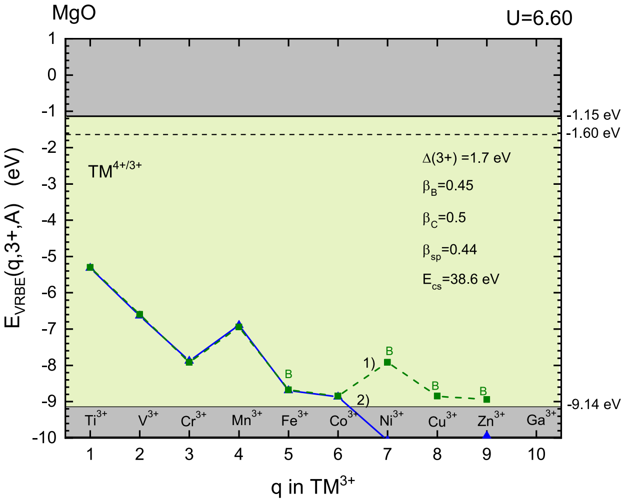

Fig. 36. Dashed curve (1) connects the $TM^{4+/3+}$ CTL energies based on computed CT energies in [10]. Solid curve (2) connects CTL energies reconstructed for the [HS] ground state configurations.

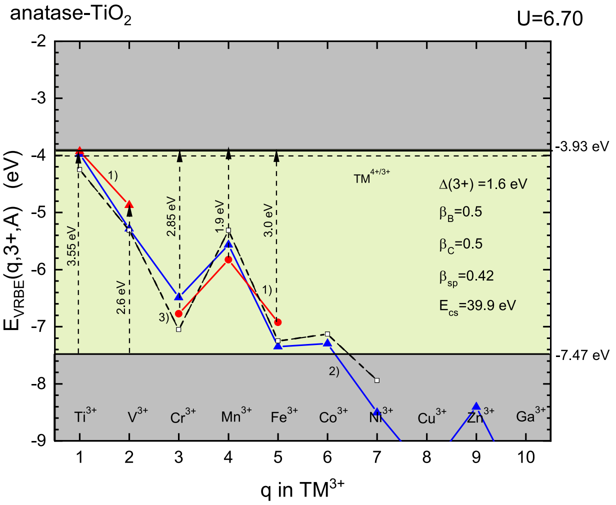

Fig. 37. Solid triangle and bullet data symbols along curves (1), $TM^{4+/3+}$ CTL energies in anatase-TiO_2 based on observed VB→TM^{4+} and TM^{3+} →CB CT-energies, respectively. Solid curve (2) connects CTL energies reconstructed for the [HS] ground state configurations. Dashed curve (3) connects the values proposed by Mizushima et al. [19].

ground states. The computations by Jing et al. [10] show that Ni^{3+} prefers the [LS] $3d^7$ $t_{2g}^6 e_g$ configuration. After adding an electron, the [HS] $3d^8$ $t_{2g}^6 e_g^2$ configuration of Ni^{2+} is obtained. The open triangle data point for $Ni^{3+/2+}$ is obtained assuming such [LS] to [HS] conversion in the reconstruction with Eq. (34).

When presenting the $TM^{2+/1+}$ CTL data in MgO, it was concluded that assigning an excitation band at 270 nm (4.59 eV) to VB→ Mn^{2+} charge transfer cannot be correct. An alternative interpretation was made by Schuyt et al. [157] assigning the same band to Mn^{2+} →CB charge transfer. That assignment would place the $Mn^{3+/2+}$ CTL energy ≈ 1 eV below the reconstructed curve 2) in Fig. 35 which is also not consistent. Possibly, the 270 nm excitation band observed by Kato et al. [150] is from VB→ CT to Mn^{3+} instead of Mn^{2+}. That transition is tentatively shown in Fig. 35, and it would agree with the reconstructed curve. This demonstrates that prior knowledge of where to expect CTL energies may help to assign observed bands in excitation or absorption spectra to specific transitions.

The values used for Δ and E_{cs} are larger and for the nephelauxetic ratios smaller in the reconstruction of the $TM^{3+/2+}$ CTL energies as compared to those used in the reconstruction of the $TM^{2+/1+}$ CTL energies. Crystal field splittings derived from $3d^q$-$3d^q$ transitions are 1.74 eV for V^{2+} in [88], 1.1 eV for Co^{2+} in [19,149], and 0.9 eV for Ni^{2+} in [19]. The $\Delta(2+)$ = 1.5 eV used for the reconstructed curve was chosen to agree with the jump between q = 3 and 4. The above experimental data indicate that $\Delta(2+)$ decreases when q increases. If so, this will reduce the jump between $q = 8$ and 9.

Curve (1) in Fig. 36 connects the $TM^{4+/3+}$ CTL energies as obtained from energies computed for the VB→TM^{4+} CT-band energies in MgO by Jing et al. [10]. Unfortunately, experimental data to verify the computational data were not found. Curve (2) connects the reconstructed CTL energies. The value $\Delta(3+)$ = 1.7 eV needed to reproduce the jump in CTL energy between q = 3 and 4 compares to the experimental $\Delta(Cr^{3+}, MgO)$ = 1.9 eV in [134,158]. The trend of increasingly higher value for $\Delta(Q)$ with a larger valence of the TM, *i.e.*, 0.8 eV, 1.5 eV, and 1.7 eV for MgO, is again confirmed. The same applies to the trend in the chemical shift (13.1 eV, 23.6 eV, and 38.6 eV) that increases with Q. The nephelauxetic parameters, particularly for $\beta_{sp}(Q)$ (0.82, 0.54, 0.44), decrease with higher Q which is also a confirmation of the expected trend.

7.3.14. Titanium oxide

Many studies have been devoted to determining the TM CTL energies, both experimentally and theoretically, in anatase-TiO_2. Mizushima et al. [19] employed already in 1972 the semi-empirical approach of Eq. (32) to estimate $TM^{3+/2+}$, $TM^{4+/3+}$, and $TM^{5+/4+}$ CTL energies in TiO_2. Due to the importance of TiO_2 for application, and because the estimates by Mizushima et al. are still occasionally used as a reference to verify computational results [7,159], it is worthwhile to compare their method and results with the present work.

Since the bottom of the CB in TiO_2 is formed by the $3d^1$ orbital of Ti^{3+}, we can already place the Ti^{3+} VRBE near the bottom of the CB as in Fig. 37. The V^{3+} VRBE energy is based on the observed VB→V^{4+} CT transition at 2.6 eV in [160–162]. That of Cr^{3+} is based on the Cr^{3+}→CB CT transition [160,163,164], and those of Mn^{3+} and Fe^{3+} are estimates based on electron spin resonance (ESR) studies [23]. Data are shown as solid bullet and solid triangle data points along curve (1) in Fig. 37. Solid curve (2) shows the reconstructed CTL curve with Eq. (34). $\Delta(3+)$ = 1.6 eV was used to reproduce the step between q = 3 and 4, and it is 0.5 eV smaller than the octahedral splitting of 2.1 eV from Cr^{3+} spectroscopy in [160,165]. It is not possible to reconstruct the CTLs based on VB→TM^{4+} data together with those based on TM^{3+}→CB data with the same set of parameters. The different types of transitions may lead to different systematic errors possibly related to lattice relaxation effects. Also, data are not yet well-established.

Mizushima et al. [19] used Eq. (32) to construct the CTL curves for TiO_2. The parameter $\phi(Q, A)$ in Eq. (32) then places the CTL curve at the desired location relative to the VB-top. It serves the same purpose as $E_{cs}(1, Q, A)$ in Eq. (34) with the important difference that there was not yet a means to pin the CTL curve relative to the vacuum level. To estimate the $TM^{4+/3+}$ CTL energies in TiO_2, Mizushima et al. assumed that the Racah parameters B_r and C_r are constant with q and Q, and the weak-field approximation for n_B and m_C in Table 2 was used. An estimated value of $\eta(3+, TiO_2)$ = 1.1 eV was chosen. It corresponds to $\beta_{sp}(3+, TiO_2)$ = 0.47 to be compared with 0.42 used in the reconstructed CTL energies of Fig. 37. Mizushima et al. assumed a crystal field splitting independent on q but did take a dependence on Q into account, and used $\Delta(Q)$ = 1.24 eV, 2.11 eV, 2.60 eV, 2.85 eV for Q = 2+, 3+, 4+, and 5+. Dashed curve (3) shows the result of Mizushima et al. The most significant difference with curves (1) and (2) is the higher value of the crystal field splitting that causes a larger

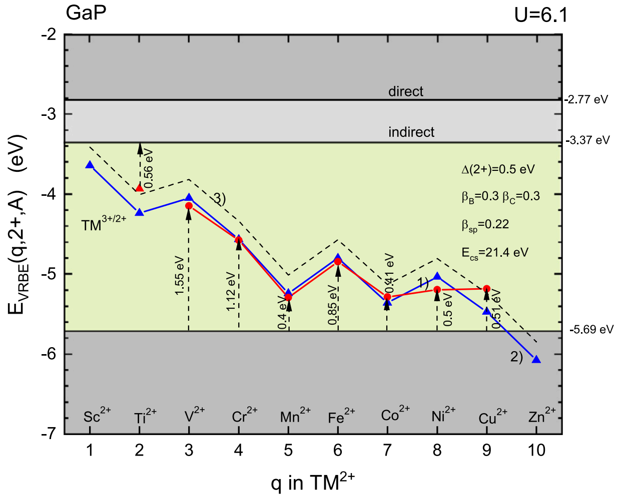

Fig. 38. Solid bullet data symbols along curve (1), experimentally derived $TM^{3+/2+}$ CTL energies on the tetrahedral Ga-sites in GaP based on the onset of VB→TM^{3+} electron transition. The triangle solid data symbol is from the onset of the Ti^{2+} →CB photo-ionization transition. Curve (2) connects the reconstructed $TM^{3+/2+}$ CTL energies for the [HS] ground state electron configurations. Dashed curve (3) is obtained when a 0.23 eV higher energy $E_{cs}(1,2+,\mathrm{GaP})$ is chosen.

step between $q = 3$ and 4. Better experimental or computational data are required to improve the reconstructed CTL curves. Nevertheless, the values of $E_{cs}(1,3+,\mathrm{TiO_2}) = 39.9$ eV and $\beta_{sp} = 0.42$ used to reconstruct curve (2) must be close to the true values.

7.3.15. Gallium phosphide

Transition metals in III–V semiconductors as GaAs, InP, and GaP and in II–VI semiconductors like ZnS, CdS, ZnSe, CdSe, and CdTe have been widely studied because they can create suitable electron donor and electron acceptor states in the bandgap. All compounds provide a tetrahedral site for the TM. Since tetrahedral (T_d) crystal field splitting is considerably smaller than with octahedral coordination, we always deal with [HS] configurations, and a CTL curve shape like the model curve in Fig. 15 is to be expected.

As an example for III–V semiconductors, the $TM^{3+/2+}$ CTL curve for GaP will be studied. The TM cation will enter the tetrahedrally coordinated Ga^{3+} site. GaP has an indirect bandgap with the bottom of the CB near −3.4 eV and the VB-top near −5.7 eV. A CB-bottom near −3 eV is characteristic for Ga-based compounds. It is also observed for β-Ga_2O_3 in Fig. 32. The P^{3-} anion is highly polarizable with relatively low electronegativity. This leads to a high-lying VB-top and a strong covalence and nephelauxetic effect with the cations. A strong nephelauxetic effect is also responsible for the low value of $U(\mathrm{GaP}) = 6.1$ eV and it will affect the parameter values needed to reconstruct the $TM^{3+/2+}$ CTL energies.

The experimental CTL energies relative to the host bands were well-established long ago because of the technological importance of semiconductors. The solid bullet data symbols along curve (1) in Fig. 38 are $TM^{3+/2+}$ CTL energies for GaP derived from the onset-energy of VB→TM^{3+} charge transfer. Those for Cr until Cu were compiled in Caldas et al. [40] and Ledebo et al. [39]. Clerjaud et al. [166] found that the $V^{3+/2+}$ acceptor level is quite close to the double acceptor level of $Ni^{2+/1+}$ that is at 1.55 eV above the VB-top [40]. The solid triangle data point for $Ti^{3+/2+}$ is from the threshold for photo-ionization of Ti^{2+} to the CB [167].

$\Delta(2+)$ values of 0.86 eV, 0.5 eV, 0.67 eV, and 0.68 eV are reported for Cr^{2+}, Fe^{2+}, Co^{2+}, and Ni^{2+}, respectively [168–171]. A value $\Delta(2+) = 0.50$ eV was used to reconstruct the CTL curve (2) in Fig. 38. The used nephelauxetic ratio $\beta_B = 0.3$ is about the same as the value of 0.28 obtained from spectroscopic studies of Ni^{2+} and Co^{2+} [170,171].

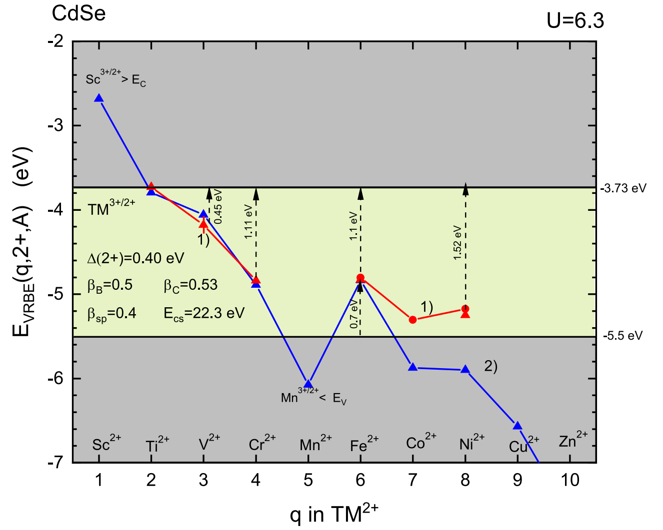

Fig. 39. Bullet data symbols along curve (1), experimentally derived $TM^{3+/2+}$ CTL energies on the tetrahedral Cd-sites in CdSe from Langer and Heinrich [43]. Solid triangle data points are based on TM^{2+}→CB photo-ionization threshold energies. Curve (2) connects the reconstructed $TM^{3+/2+}$ CTL energies for the [HS] ground state configurations.

The $Ti^{3+/2+}$ CTL energy is derived from the onset of Ti^{2+}→CB photo-ionization. It appears to deviate several 0.1 eV from the reconstructed CTL energy. For $Cu^{3+/2+}$, we are possibly dealing with a so-called Bader state. When an electron is removed from Cu^{2+}, Cu^{2+} with a nearby trapped valence band hole is formed instead of Cu^{3+}.

In the compounds treated so far, we always used the maximum of the VB→TM CT-band to place the corresponding CTL energy above the VB-top. In the semiconductor field, the onset is generally used for that purpose, and we followed that method in Fig. 38. The energy difference between the onset and the maximum of the VB→Fe^{3+} CT-band amounts to 0.23 eV in [169]. Adopting the same difference for the other TMs, the dashed CTL curve (3) in Fig. 38 would be obtained. In such a case, agreement is obtained with the $Ti^{3+/2+}$ CTL and $E_{cs}(1,2+,\mathrm{GaP})$ would become 21.7 eV.

7.3.16. Cadmium selenide

CdSe will be treated as a representative of the II–VI semiconductors that provide sites of tetrahedral coordination for the TMs. The spectroscopy of transition metals has been intensively studied, and much information can be found in the literature. All available experimental data are shown along curves (1) in Fig. 39.

Due to the small bandgap of CdSe, most $TM^{Q+1/Q}$ CTL energies fall either above the CB-bottom or below the VB-top. For example, Sc^{2+} auto-ionizes to become Sc^{3+} which means that the $Sc^{3+/2+}$ CTL is above the CB-bottom [172]. Baranowski and Langer [172] suggest that the Mn^{2+} ($3d^5$) ground state is below the VB-top which means that Mn^{3+} is not a stable valence. The $Ti^{3+/2+}$ CTL is known to be resonant with the CB-bottom [173]. The $Cr^{3+/2+}$ and $Fe^{3+/2+}$ CTL-energies are well-established and based on the threshold of TM^{2+}→CB photo-ionization reported in Baranowski and Langer [172]. The 0.45 ± 0.1 eV threshold for photo-ionization of V^{2+} is based on an estimate in Baranowski and Langer [172]. The threshold energy for VB→Fe^{3+} electron transfer is ≈ 0.7 eV [172,174]. The resulting CTL location is consistent with the 1.1 eV threshold energy for photo-ionization of Fe^{2+} as seen in Fig. 39. The value of 1.52 eV for the photo-ionization threshold energy of Ni^{2+} is from Baranowski and An [175].

Curve (2) in Fig. 39 connects the reconstructed $TM^{3+/2+}$ CTL energies. The used $\Delta(2+) = 0.40$ eV is about the same as the average $\Delta(2+)$ for Ti, V, Cr, Fe, Co, Ni, Cu as derived from optical absorption

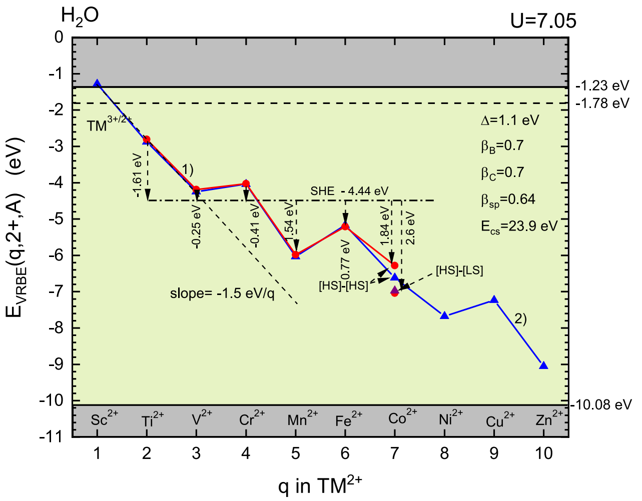

Fig. 40. Solid bullet data symbols along curve (1), are the $TM^{3+/2+}$ CTL energies in H_2O. They are based on (II/III) reduction potentials of TM in water relative to the standard hydrogen potential (SHE) shown as a dashed line at −4.44 eV energy. Curve (2) connects the reconstructed CTL energies assuming [HS] configurations.

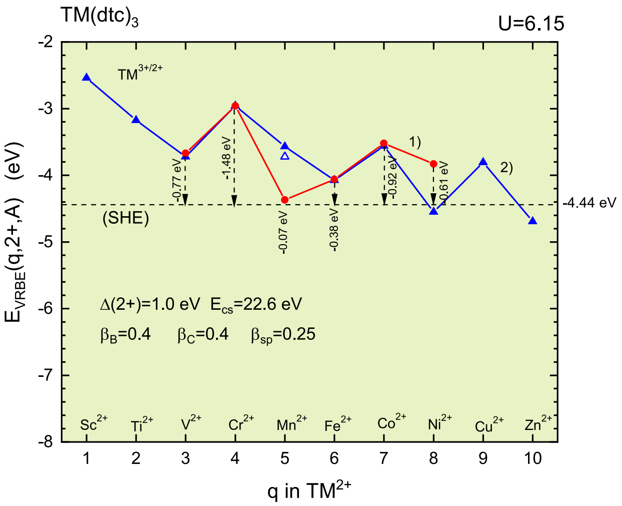

Fig. 41. Closed bullet data symbols along curve (1), $TM^{3+/2+}$ CTL energies for TM dithiocarbamate complexes based on E^0(II/III) redox potentials relative to the SHE potential in [38]. Solid curve (2) connects reconstructed CTL energies obtained for the [LS] systems on octahedral sites in the strong-field approximation. The open triangle data point is the $Mn^{3+/2+}$ CTL energy assuming a [HS] to [LS] conversion upon removing a 3d-electron.

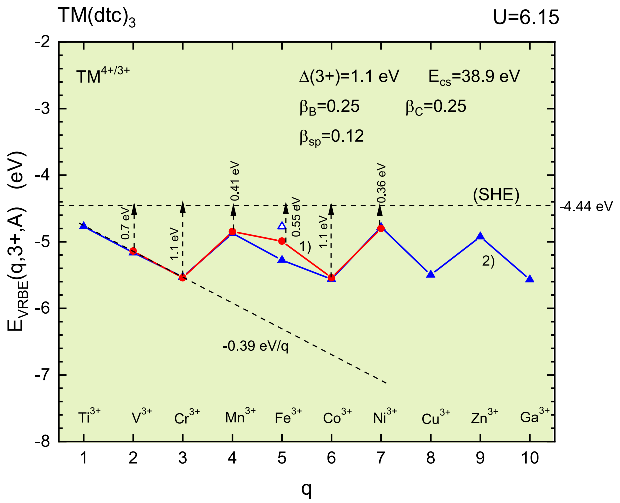

Fig. 42. Closed bullet data symbols along curve (1), $TM^{4+/3+}$ CTL energies for TM dithiocarbamate complexes based on E^0 (III/IV) redox potentials relative to the SHE potential in [38]. Solid curve (2) connects reconstructed CTL energies obtained for the [LS] systems on octahedral sites in the strong-field approximation. The open triangle data point is the $Fe^{4+/3+}$ CTL energy assuming a [HS] to [LS] conversion upon removing a 3d-electron.

date on TM^{2+} in Langer and Baranowski [176]. $\beta_B = 0.5$ used for the reconstruction is similar to the value found from optical absorption data in [176].

7.3.17. Water

TM^{2+} in water is octahedrally surrounded by six H_2O molecules with the oxygen ligands oriented towards TM^{2+}. For V until Co the (II/III) redox potentials relative to the standard hydrogen electrode (SHE) potential, as gathered by van Gaal and van der Linden [38] in 1982, were used. When the redox potentials are subtracted from the SHE absolute energy of −4.44 eV, the $TM^{3+/2+}$ CTL energies shown as solid bullet symbols along curve (1) in Fig. 40 are obtained. Johnson and Nelson [177] estimated the hydration enthalpy of $[Ti(H_2O)_6]^{3+}$ using ligand field theory, from which they predicted a Ti(II/III) redox potential of −1.61 V. Curve (2) connects the reconstructed CTL energies assuming [HS] ground state electron configurations. With $\Delta(2+, H_2O) =$ 1.1 eV, the agreement with the available experimental data is fairly good. From curve (2), the Ti(II/III) redox potential is predicted at 1.63 V which is the same as the potential estimated by Johnson and Nelson [177]. The only information found on crystal field splitting in water is $\Delta(2+, H_2O) = 0.89$ eV for Cr^{2+} from Petkova et al. [178].

The reconstructed Co^{2+} CTL energy appears ≈ 0.4 eV below the value derived from the redox potential. This was also observed by van Gaal and van der Linden [38], and they suggested that Co^{3+} might have the [LS] $3d^6\ t_{2g}^6$ ground state electron configuration in the $[Co(H_2O)_6]^{3+}$ hexa-aqua complex. Johnson and Sharpe [179] provided a deeper analysis of the Co hexa-aqua complex and claim that if both $[Co(H_2O)_6]^{3+}$ and $[Co(H_2O)_6]^{2+}$ were [HS] complexes, the redox potential in aqueous solution would be 2.6 V. The corresponding CTL energy is shown in Fig. 40 and falls 0.4 eV below the reconstructed value. The solid triangle data symbol for the $Co^{3+/2+}$ CTL in Fig. 40 is obtained when a [HS] to [LS] $Co^{2+} \rightarrow Co^{3+}$ conversion is assumed. It appears quite close to the value from the analysis of Johnson and Sharpe.

7.3.18. 3-dithiocarbamate complexes

Van Gaal and van der Linden [38] gathered (I/II), (II/III), (III/IV), and (IV/V) redox potentials relative to the SHE potential for 9 different octahedral or pseudo-octahedral $3d^q$ transition metal complexes. Their E^0 (II/III) redox potentials in water were used in Fig. 40. Here, we will treat the E^0 (II/III) and E^0 (III/IV) redox potentials of $TM(dtc)_3$ where TM is surrounded by three negatively charged chelating dithiocarbamate groups ($dtc{=}R_2NCS_2^-$). The six sulfur atoms of the three molecules form an octahedral coordination with O_h point symmetry. By using the VRBE energy of −4.44 eV of the SHE potential, the redox potentials are converted to the TM^{2+} and TM^{3+} VRBE energies as in Figs. 41 and 42. Dithiocarbamate was chosen because a fairly complete series of redox potentials is available and the sulfur atoms in the complex create a large nephelauxetic effect. β_ζ will be small due to the large nephelauxetic effect, and hence relatively little energy is gained in spin alignment when the 3d-orbitals are filled. This, together with still a large octahedral crystal field splitting, causes the [LS] electron configurations to be favored over the [HS] configurations, and the coefficients from Table 6 of the strong-field approximation were used for $q = 4$ until 7 to reconstruct the CTL energies.

Curve (2) in Fig. 41 connects the reconstructed $\mathrm{TM}^{3+/2+}$ CTL energies. The shape can be compared with the example in Fig. 14. The nephelauxetic ratios used are significantly smaller than those for the other 17 environments treated in this work. Curve (2) in Fig. 42 connects the reconstructed $\mathrm{TM}^{4+/3+}$ CTL energies. The higher TM valence causes even lower values for the nephelauxetic ratios. The extremely low $\beta_{sp} = 0.12$, tilts the spherical interaction curve $C(q, 3+, \mathrm{3dtc})$ to an almost horizontal line. The value used for $\Delta(2+, \mathrm{3dtc})$ was 0.1 eV smaller than for $\Delta(3+, \mathrm{3dtc})$ which is in line with the trend observed for other environments. A description of the shape of the CTL curve in Figs. 41 and 42 is the same as the one provided with the CTL curve example in Fig. 14.

The experimentally derived $\mathrm{Mn}^{3+/2+}$ CTL energy is ≈ 0.8 eV below the reconstructed value of curve (2) in Fig. 41. The same was noticed by van Gaal and van der Linden [38], and they suggested that $3d^5$ Mn^{2+} might adopt the [HS] $t_{2g}^3 e^2$ electron configuration. The open triangle data point for the $\mathrm{Mn}^{3+/2+}$ CTL energy in Fig. 41 is obtained when a [HS] to [LS] conversion is assumed with Eq. (34). It decreases the reconstructed CTL energy by ≈ 0.2 eV which is still insufficient to agree with the experimental result. Note that the reconstructed $\mathrm{Fe}^{4+/3+}$ CTL energy along curve (2) in Fig. 42 is 0.25 eV below the energy obtained from the redox potential. If a [HS] to [LS] conversion is assumed for Fe in Eq. (34), the $\mathrm{Fe}^{4+/3+}$ CTL energy is 0.25 eV above curve (2) as shown by the open triangle data point in Fig. 42.

8. Discussion

In this work, data have been collected to derive the TM^{Q} VRBEs or $\mathrm{TM}^{Q+1/Q}$ CTL energies for transition metals for $Q = 1+$, $2+$, and $3+$ in 18 chemical environments that provide octahedral or tetrahedral coordination around the TM. The environments cover the entire spectrum of inorganic compounds (fluorides, chlorides, bromides, oxides, sulfides, selenides, phosphides) for which bandgaps range from > 12 eV in the fluorides down to < 2 eV in the semiconductors. The environments also cover that of water and the organic 3-dithiocarbamate chelating groups. Unique in the analysis is that energies are related to the vacuum level, whereas in the past the valence band top or the SHE potential was used as the reference. By employing Eq. (34), VRBE energies were reconstructed with a set of parameters that include the Racah parameters $B_r(q, Q, A)$, $C_r(q, Q, A)$, the spin–orbit coupling parameter $\zeta_{dd}(q, Q, A)$, the crystal field splitting $\Delta(Q, A)$, the chemical shift $E_{cs}(1, Q, A)$, and the introduced spherical nephelauxetic parameter $\beta_{sp}(Q, A)$. The two Racah parameters B_r and C_r are reduced in a chemical environment relative to the value in vacuum due to the nephelauxetic effect. By introducing the nephelauxetic ratios $\beta_B(Q, A) \equiv B_r(q, Q, A)/B_r(q, Q, \mathrm{vac})$ and $\beta_C(Q, A) \equiv C_r(q, Q, A)/C_r(q, Q, \mathrm{vac})$ such reduction is parameterized where it is assumed that the ratios do not depend on q. In this work, we then use computed values for the Racah parameters in vacuum as compiled in Table 4. The spin–orbit coupling parameter ζ_{dd} does not have a large contribution to the VRBE and this contribution was usually ignored. Here, to be complete, we took it into account by introducing the nephelauxetic ratio β_ζ that was always chosen equal to β_C.

The crystal field splitting $\Delta(q, Q, A)$ can be obtained from the Tanabe–Sugano diagram. The value used in Eq. (34) should then be consistent with that obtained from such a diagram. $\Delta(q, Q, A)$ is expected and observed to increase when the valence Q increases. When Q increases, the screening charge on the surrounding anions will increase. It was suggested with Eq. (24) that the larger effective screening charge on the ligands is the cause for increased crystal field splitting. When a $3d^q$ TM^Q is introduced as a dopant in a compound, the surroundings will adapt to screen the charge of the cation. One has to assess whether, upon removal of an electron from $3d^q$, the surroundings can instantaneously adapt to the new situation with a TM of higher valence $Q + 1$. $\gamma(Q)$ as defined in Eq. (33) and introduced in Eq. (34) accounts for this effect, and fixed values of 0.25, 0.2, 0.15 were used for $Q = 1+$, $2+$, and $3+$, respectively. Although crystal field splitting often depends on q, such a dependence was ignored in the reconstruction of CTL energies. The two remaining parameters, *i.e.*, chemical shift $E_{cs}(1, Q, A)$ and the spherical nephelauxetic ratio $\beta_{sp}(Q, A)$, will appear crucial for the resulting VRBEs and CTL energies. In the following analysis, we will see that these two parameters behave in a very systematic fashion with Q and with the type of environment A, and similar will apply for β_B and β_C. Crystal field splitting appears strongly related to the immediate surroundings of the TM. This all means that although there are many parameters, in the end, they are all strongly related.

8.1. *The chemical shift*

Table 7 compiles the chemical shift $E_{cs}(1, Q, A)$ and the crystal field splitting $\Delta(Q, A)$ used for the reconstructed CTL energies in this work. They are listed with decreasing $U(A)$. $U(A)$ can be derived from experimental data on lanthanide spectroscopy or estimated from the composition of the compounds [63]. We intend to compare the chemical shift $E_{cs}(1, Q, A)$ for the transition metals with the chemical shift for the lanthanides in the same environment A. The chemical shift of the $4f$ ground state VRBE of Eu^{2+} appeared already in Eq. (23) and is given by

$$E^{4f}_{cs}(\mathrm{Eu}^{2+}, A) = \frac{18.05 - U(A)}{0.777 - 0.0353U(A)}. \tag{37}$$

The chemical shift for Eu^{3+} is then given by

$$E^{4f}_{cs}(\mathrm{Eu}^{3+}, A) = 18.05 - U(A) + E^{4f}_{cs}(\mathrm{Eu}^{2+}, A). \tag{38}$$

The chemical shift for the average of the five $5d$ states is given by

$$E^{5d}_{cs}(\mathrm{Eu}^{Q}, A) = E^{4f}_{cs}(\mathrm{Eu}^{Q}, A) - \epsilon_c(\mathrm{Eu}^{Q}, A). \tag{39}$$

The values for $E^{4f}_{cs}(\mathrm{Eu}^{2+}, A)$ are compiled in column 3 of Table 7. It is 20.5 eV for $\mathrm{KMgF_3}$ and increases steadily until 21.3 eV for GaP. The magnitude and the increase have been interpreted with Eq. (22). The remarkable almost constant value for the chemical shift implies that within the Chemical Shift model the $-Q$ screening charge is located at a screening distance that is almost invariant from compound to compound.

In the case of the lanthanides, the following empirical relation between the centroid shift for the $5d^1$ excited states of Ce^{3+} and the $U(A)$ value was found [64]

$$\epsilon_c(1, 3+, A) = -2.2\ln\left(\frac{U(A) - 5.44}{2.83}\right). \tag{40}$$

Assuming that the $5d^1$ centroid shift $\epsilon_c(6, 3+, A)$ for Eu^{3+} is the same as that for Ce^{3+}, the chemical shift $E^{5d}_{cs}(\mathrm{Eu}^{3+}, A)$ as obtained with Eq. (39) is compiled in column 5 of Table 7. Further, following the findings in [72], we will assume $\epsilon_c(7, 2+, A) = \frac{2}{3}\epsilon_c(6, 3+, A)$ which then yields $E^{5d}_{cs}(\mathrm{Eu}^{2+}, A)$ as compiled in column 4 of Table 7. We have the remarkable result that the chemical shift for the average $5d^1$ VRBE of divalent lanthanides is always ≈ 20 eV. It decreases by only 1 eV over the entire range of chemical environments. For the trivalent lanthanides, the average $5d^1$ VRBE is even more constant at ≈ 30.3 eV. The ratio 20/30.3 between both chemical shifts is the same as the ratio 2+/3+ between the valence of the lanthanides.

The $5d^1$ chemical shifts of the lanthanides and those of monovalent ($Q = 1+$), divalent ($Q = 2+$), and trivalent ($Q = 3+$) transition metals are collected in Table 7 and displayed against $U(A)$ in Fig. 43. As for lanthanides, the chemical shift of TMs is rather constant when the compound or the environment changes, but increases more or less proportionally with a higher valence Q. On closer inspection, it seems that when $U(A)$ decreases from 7.7 eV to 6.8 eV, the chemical shift tends to increase, and then below 6.8 eV it tends to decrease again. The initial increase can be interpreted with Eq. (22) or Eq. (31). When $U(A)$ decreases, the bonding of the anion ligands decreases. The polarizability of the ligands increases, resulting in better screening of the TM cation charge. In Eq. (22) or Eq. (31), this means that the screening

Table 7
The chemical shift and crystal field splitting used for the reconstructed CTL energies that are arranged in order of decreasing $U(A)$ value for the chemical environment A. All energies are in eV.

A	$U(A)$	$E_{cs}^{4f}(\mathrm{Eu}^{2+})$	$E_{cs}^{5d}(\mathrm{Eu}^{2+})$	$E_{cs}^{5d}(\mathrm{Eu}^{3+})$	$E_{cs}(1,1+)$	$E_{cs}(1,2+)$	$E_{cs}(1,3+)$	$\Delta(1+)$	$\Delta(2+)$	$\Delta(3+)$
vacuum	–	–	–	–	–	–	–	–	0	0
$KMgF_3$	7.66	20.5	20.2	30.4	–	22.5	36.8	–	1.4	1.8
MgF_2	7.5	20.6	20.1	30.4	–	22.6	–	–	1.2	–
NaF	7.3	20.7	20.1	30.5	–	22.5	–	–	1.2	–
LiF	7.3	20.7	20.1	30.5	–	23	–	–	1.3	–
H_2O	7.05	20.8	20.0	30.6	–	23.9	–	–	1.1	–
Ga_2O_3	6.9	20.9	19.9	30.6	–	24.5	39.5	–	1.6	1.8
Al_2O_3	6.8	21.0	19.9	30.6	–	24.2	39.7	–	1.9	2.2
$MgAl_2O_4$	6.8	21.0	19.9	30.6	–	24.4	40.2	–	2	2.2
$Y_3Al_5O_{12}$	6.77	21.0	19.9	30.6	–	24	39.5	–	1.7	2.1
LiCl	6.75	21.0	19.9	30.6	13.3	–	–	0.65	–	–
$CdCl_2$	6.7	21.0	19.8	30.6	12.9	–	–	0.6	–	–
TiO_2	6.7	21.0	19.8	30.6	–	–	39.9	–	–	1.6
MgO	6.6	21.0	19.8	30.5	13.1	23.6	38.6	0.8	1.5	1.7
LiBr	6.6	21.0	19.8	30.5	13	–	–	0.55	–	–
$CdBr_2$	6.55	21.1	19.7	30.5	13.1	–	–	0.5	–	–
CdSe	6.3	21.2	19.5	30.3	–	22.3	–	–	0.40	–
3-dtc	6.15	21.3	19.2	30.1	–	22.6	38.9	–	1	1.1
GaP	6.1	21.3	19.2	30.0	–	21.4	–		0.50	–

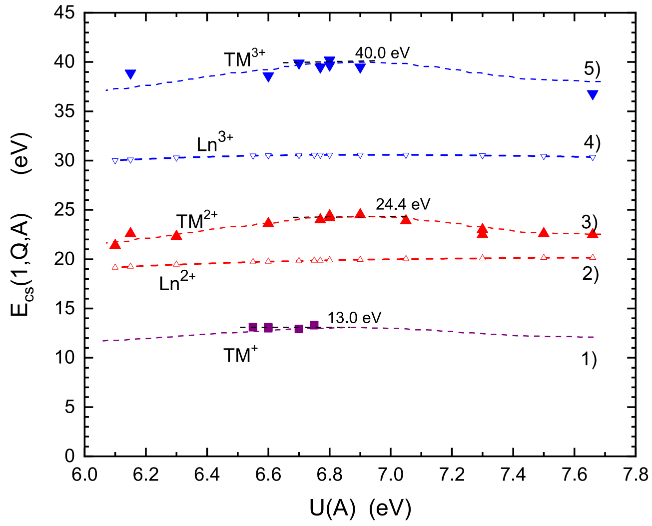

Fig. 43. Data along curves (1), (3), and (5) are the chemical shifts $E_{cs}^{3d}(1,Q,A)$ for the transition metals of valence $Q = 1+$, $2+$, and $3+$ used in reconstructing the $\mathrm{TM}^{(Q+1)/Q}$ CTL energies in the compounds treated in this work. The dashed lines tentatively illustrate the trend. Curves (2) and (4) are the chemical shifts E_{cs}^{5d} for Eu^{2+} and Eu^{3+} as a function of $U(A)$.

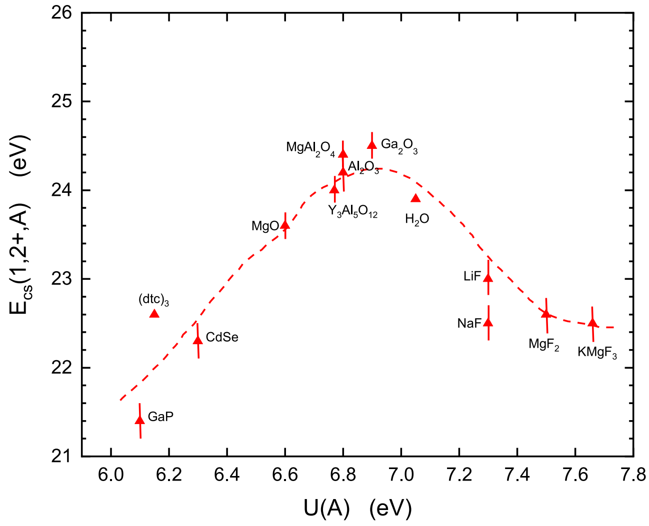

Fig. 44. $E_{cs}(1,2+,A)$ values used to reconstruct $\mathrm{TM}^{3+/2+}$ CTL energies against the parameter $U(A)$. The dashed curve is drawn to guide the eye. The error bars result from uncertainty in the energy at the VB-top.

distance R_Q shortens and the chemical shift increases. Below 6.8 eV, one still expects that screening becomes better but other contributions to $E_{cs}(1,Q,A)$, like the $3d^1$ centroid shift, apparently become more important. The average chemical shifts of these compounds with $U(A)$ between 7.1 eV and 6.5 eV are 13.0 eV, 24.4 eV, and 40.0 eV for $Q = 1+$, $2+$, and $3+$, respectively. This is in a ratio of 1 to 1.9 to 3.1. We arrive at the same conclusion as made for the lanthanides, *i.e.*, the chemical shift is almost proportional to the valence Q of the TM.

Curves (2) and (3) in Fig. 43 show that the chemical shift $E_{cs}(1,2+,A)$ for TM^{2+} is larger than the $5d^1$ chemical shift for Eu^{2+}. Curves (4) and (5) demonstrate the same for TM^{3+} and Eu^{3+}. This can be explained with Eq. (22) or Eq. (31) and the ionic radii for the lanthanides in Fig. 7 and for the TMs in Fig. 8. The ionic radius of TM^Q is always smaller than that of Ln^Q. This leads to a smaller screening distance and larger chemical shift for the TM^Q.

Fig. 44 shows an enlarged view of the $E_{cs}(1,2+,A)$ data. Starting at the highly ionic fluorides near $U(A) = 7.6$ eV, the chemical shift increases and reaches a maximum of ≈ 24.4 eV for oxides near U=6.8 eV. Moving further towards the highly covalent semiconductor GaP with $U(A) = 6.1$ eV, the chemical shift decreases. There appears to be a relation with $U(A)$ as tentatively illustrated by the dashed curve. Errors in the VRBE at the valence band top of the host compound will translate into errors in the chemical shift needed to reconstruct the CTL energies. The error bars caused by the error in E_V are shown in Fig. 44.

8.2. *The crystal field splitting*

The crystal field splitting $\Delta(Q,A)$ used to reconstruct the CTL energies is compiled in Table 7. They were all chosen close to values derived independently from Tanabe–Sugano diagrams, and in that sense are consistent. For a set of point charges at the vertices of a regular octahedron around the TM, expression Eq. (24) applies for the crystal field splitting. However, in real compounds, it is not the formal charge Z of the anion that controls the splitting. Instead, it was suggested that the screening charge $Q/6$ per anion should be used as the effective charge [71]. For the lanthanides Ce^{3+} and Eu^{2+}, it was established that $\Delta(3+,A) \approx 1.3\Delta(2+,A)$. It partly reflects the 3+/2+ ratio of the valences. The results in Table 7 show that the crystal field splitting

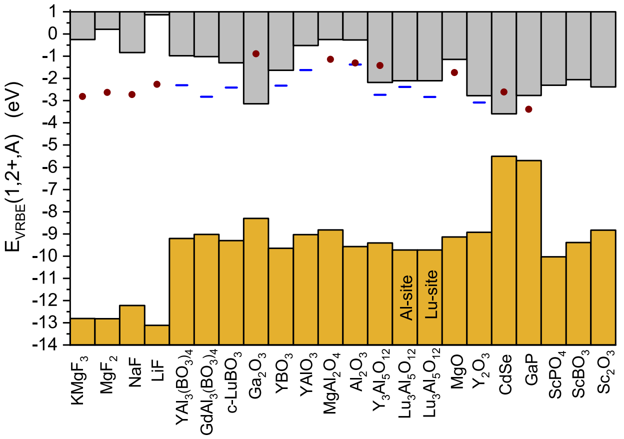

Fig. 45. Stacked VRBE diagram with the location of the experimentally derived Sc$^{3+/2+}$ CTL energies shown as horizontal bars. The Sc^{3+} doped compounds are placed in a sequence of decreasing value for U from 7.66 eV for KMgF$_3$ down to 6.1 eV for GaP. Solid bullet data points are the reconstructed Sc$^{3+/2+}$ CTL energies. E_V and E_C of three Sc^{3+} based compounds are added to the right of the diagram.

tends to increase when Q increases. For the seven compounds in Table 7 where $\Delta(3+,A)$ and $\Delta(2+,A)$ are listed, on average $\Delta(3+,A) = (1+0.16)\times \Delta(2+,A)$. This motivated the use of $\gamma(2+) = 0.2$ in the reconstruction of the TM$^{3+/2+}$ CTL energies with Eq. (34).

The VRBE energies in the $3d^1$ TMs are particularly simple to describe. Eqs. (29) and (34) reduce to $E_{VRBE}(1,Q,A) = C(1,Q,\text{vac}) + S(1,Q,A) + E_{cs}(1,Q,A) + \epsilon_1(Q,A)$. The energy $S(1,Q,A) = -\frac{3}{2}\beta_\zeta\zeta_{dd}(1,Q,\text{vac})$ is $<$ 0.01 eV and can be neglected. If $Q = 1+$, one deals with the VRBE in the [Ar]$3d^1$ configuration of Ca$^+$. This configuration is never the ground state of Ca$^+$ and CTL data are not available. For $Q = 2+$ and $Q = 3+$, one deals with Sc^{2+} and Ti^{3+} and CTL data are available.

Fig. 45 shows a stacked VRBE diagram of compounds for which the Sc^{2+} VRBE has been obtained from either VB→Sc^{3+} CT-band energies or the reconstructed TM$^{3+/2+}$ CTL energies in this work. Most of the data was collected by Rogers and Dorenbos [75]. The VRBE in the Sc^{2+} ground state tends to fall between −2 eV and −3 eV. The last three compounds in the diagram show the energy E_C at the CB-bottom of three Sc^{3+} compounds like ScPO$_4$. E_C is found in the same energy range because the bottom of the CB is dominantly formed by the $3d^1$ orbitals of Sc^{2+}.

The Sc^{2+} VRBEs are determined by $E_{cs}(1,2+,A)$ that changes smoothly with $U(A)$, and on top of that the level energy $\epsilon_1(2+,A)$. $\epsilon_1(2+,A) = -0.4\Delta(2+)$ for octahedral coordination and $-0.6\Delta(2+)$ for tetrahedral coordination. The stacked diagrams also contain data on compounds that provide coordination other than octahedral or tetrahedral.

Fig. 46 shows a stacked VRBE diagram for Ti^{3+} doped compounds where to the right of the diagram the E_V and E_C of eight Ti^{4+} compounds like CaTiO$_3$ are added. As in Fig. 45, most of the data was already collected by Rogers and Dorenbos [75]. The VRBE in the Ti^{3+} ground state tends to be located near −4 eV, and variations therein are attributed to changes in chemical shift with changing $U(A)$ and to compound-to-compound changes in $\epsilon_1(3+,A)$. The eight Ti^{4+} compounds where the CB-bottom is formed dominantly by the $3d^1$ orbitals of Ti^{3+} have E_C around −3.6 eV. The Ti^{3+} VRBE for MgO and KMgF$_3$ are 1 to 2 eV below those of the other compounds in Fig. 46. These two data, labeled with the letter C, are computed by Jing et al. [11] without experimental validation. The deviation may then hint towards a systematic computational error. In Rogers and Dorenbos [92], a strongly deviating Ti^{3+} VRBE near −7 eV was reported for LiF. It was derived from a Ti^{4+} charge transfer band observed in Vergara et al. [180]. However, rather than an F$^-$→Ti^{4+} CT-band, a charge transfer from O^{2-} impurities seems a more plausible assignment. The dubious data point for LiF in Rogers and Dorenbos [92] has been omitted in Fig. 46.

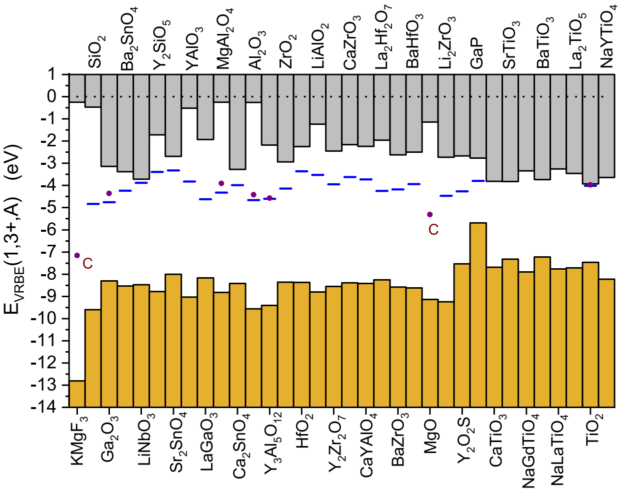

Fig. 46. Stacked VRBE diagram with the location of experimentally derived Ti$^{4+/3+}$ CTL energies shown as horizontal bars. The Ti^{4+} doped compounds are placed in a sequence of decreasing value for U from 7.66 eV for KMgF$_3$ down to 6.1 eV for GaP. Solid bullet data points are the reconstructed Ti$^{4+/3+}$ CTL energies. Those marked with the letter C are from computational studies. E_V and E_C of eight Ti^{4+} based compounds are added to the right of the diagram.

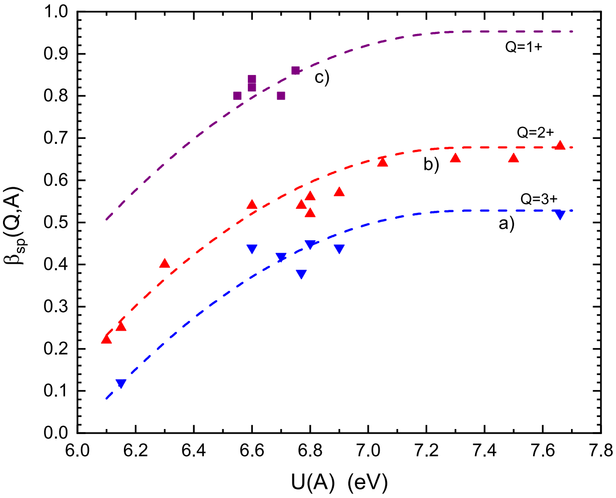

Fig. 47. The values for the spherical nephelauxetic ratio β_{sp} as obtained from reconstructed CTL energies against the $U(A)$ value of the compound. Data along curve (a) $\beta_{sp}(3+,A)$, along curve (b) $\beta_{sp}(2+,A)$, along curve (c) $\beta_{sp}(1+,A)$. The dashed curves are drawn to guide the eye.

8.3. The nephelauxetic ratios

The values of the spherical nephelauxetic ratio $\beta_{sp}(Q,A)$ and the nephelauxetic ratios $\beta_B(Q,A)$ and $\beta_C(Q,A)$ for the 18 environments of this work are compiled in Table 8. The $\beta_B(Q,A)$ and $\beta_C(Q,A)$ values can experimentally be obtained from the $3d^q$ level energies in a Tanabe–Sugano diagram. The values used for β_B and β_C are consistent with the experimentally derived values. However, $\beta_{sp}(Q,A)$ is entirely empirically established. Since $U(A)$ characterizes the size of the nephelauxetic effect, the three ratios are expected to follow $U(A)$. This is demonstrated in Table 8. For example, $\beta_B(2+,A)$ decreases from

Table 8
The nephelauxetic ratios used in the reconstruction of the CTL energies that are arranged in order of decreasing $U(A)$ value for the chemical environment A.

A	$U(A)$	$\beta_{sp}(1+)$	$\beta_{sp}(2+)$	$\beta_{sp}(3+)$	$\beta_B(1+)$	$\beta_B(2+)$	$\beta_B(3+)$	$\beta_C(1+)$	$\beta_C(2+)$	$\beta_C(3+)$
vacuum	18.05	1	1	1	1	1	1	1	1	1
$KMgF_3$	7.66	–	0.68	0.52	–	0.9	0.7	–	0.9	0.7
MgF_2	7.5	–	0.65	–	–	0.9	–	–	0.9	–
NaF	7.3	–	0.65	–	–	0.85	–	–	0.85	–
LiF	7.3	–	0.65	–	–	0.95	–	–	0.95	–
H_2O	7.05	–	0.64	–	–	0.7	–	–	0.7	–
Ga_2O_3	6.9	–	0.57	0.44	–	0.7	0.6	–	0.7	0.65
Al_2O_3	6.8	–	0.56	0.45	–	0.7	0.6	–	0.65	0.6
$MgAl_2O_4$	6.8	–	0.52	0.45	–	0.65	0.55	–	0.65	0.55
$Y_3Al_5O_{12}$	6.77	–	0.54	0.38	–	0.65	0.6	–	0.65	0.6
LiCl	6.75	0.86	–	–	0.7	–	–	0.75	–	–
$CdCl_2$	6.7	0.8	–	–	0.75	–	–	0.75	–	–
TiO_2	6.7	–	–	0.42	–	–	0.5	–	–	0.5
MgO	6.6	0.82	0.54	0.44	0.65	0.55	0.45	0.74	0.55	0.5
LiBr	6.6	0.84	–	–	0.65	–	–	0.7	–	–
$CdBr_2$	6.55	0.8	–	–	0.65	–	–	0.65	–	–
CdSe	6.3	–	0.4	–	–	0.5	–	–	0.53	–
3-dtc	6.15	–	0.25	0.12	–	0.4	0.25	–	0.4	0.25
GaP	6.1	–	0.22	–	–	0.3	–	–	0.3	–

0.9 for the highly ionic compound $KMgF_3$ with $U(A) = 7.66$ eV to 0.3 for the highly covalent compound GaP with $U(A) = 6.1$ eV. The decrease is much stronger than observed for the $4f^q$ lanthanides where β decreases from 0.96 to ≈ 0.90 for a similar range of compounds [83]. When Q increases from 1+, 2+, to 3+, Table 8 demonstrates that the three nephelauxetic ratios decrease. Fig. 47 shows $\beta_{sp}(Q, A)$ against $U(A)$ and Q. The dashed lines through the data are drawn to guide the eye. β_{sp} decreases when $U(A)$ becomes smaller, and decreases when the valence Q becomes larger.

8.4. Demonstration on how TM^Q VRBEs change with q, Q, and A

Figs. 43 and 47 show that for $U(A) \approx 6.7$ eV, the chemical shift $E_{cs}(1, Q, A)$ increases from 13.0 eV to 24.4 eV to 40.0 eV and β_{sp} decreases from about 0.84 to 0.56 to 0.41 when Q increases from 1+ to 2+ to 3+, respectively. Fig. 48 illustrates how these parameter values affect the VRBE energies. Curves (a1) (two times), (b1), and (c1) connect the spherical interaction energies $C(q, Q, \mathrm{vac})$ for Q is 1+, 2+, and 3+ where the linear approximations in Table 1 were used. Applying the $\beta_{sp}(3+, A) = 0.41$ ratio, the $C(q, 3+, \mathrm{vac})$ curve (a1) on the left tilts counterclockwise to become curve (a3). Next, the chemical shift of $E_{cs}(1, 3+, A) = 40$ eV (see arrow 1) is applied to arrive at curve (a2). Arrows (2) and (3) are drawn to illustrate the various contributions to the chemical shift. We have the upward shift (arrow 2) due to the screening charge of Eq. (22), and a downward shift (arrow 3) from the centroid shift ϵ_c and the difference $\Delta W \equiv C(1, 3+, \mathrm{vac}) - C(1, 3+, A)$. Adding the effect of 1.8 eV octahedral crystal field splitting yields curve (a4). The directional interaction energies $S(q, 3+, A)$ need to be added to arrive at the final CTL energies. Note that for $3d^1$ Ti^{3+}, $S(1, 3+, A) \approx 0$ and the start of curve (a4) is then the Ti^{3+} VRBE near −4 eV as in Fig. 46.

On the right-hand side of Fig. 48, curves (a1), (b1), (c1) are changed to curves (a2), (b2), (c2) due to the β_{sp} values of 0.41, 0.56, and 0.84 plus the chemical shift values of 40 eV (arrow 1), 24.4 eV (arrow 4) and 13.0 eV (arrow 5). We have arrived at a situation where the three curves connecting the spherical interaction energies $C(q, Q, A)$ run almost parallel with a small distance from each other. For further illustration, the location of a conduction band bottom at −1 eV and a valence band top at −8 eV, typical for wide-bandgap oxides, is shown around curves (a2), (b2), and (c2). This part of Fig. 48 is redrawn in Fig. 49 but now as a function of atomic number Z and based on the genuine $C(q, Q, \mathrm{vac})$ energies listed in Table SI-I. The CTL curves (a3), (b3), and (c3) are obtained by using typical values for $\Delta(Q, A)$ and adding the $S(q, Q, A)$ contributions using typical values for the nephelauxetic ratios. N.B., the same curves were used for the illustration in the top panel of Fig. 2.

Whenever a TM$^{Q+1/Q}$ CTL is inside or just above the valence band, the TM^{Q+1} will/may reduce to TM^Q. It may also form a Bader state which is a $3d^q$ TM^Q with a hole localized on nearby anion ligands. Ni^{4+}, Cu^{4+}, Zn^{4+}, and Ga^{4+} with TM$^{4+/3+}$ CTL located below the VB-top in Fig. 49 cannot be stable. When TM$^{Q+1/Q}$ is in or just below the conduction band, the TM^Q will/may spontaneously oxidize to TM^{Q+1}. This is the case for Sc^{2+} on the far left of curve (b3), and for the monovalent V^+ on the far left of curve (c3). Cu^+ is the monovalent TM furthest below the CB and a known stable valence.

A relation between $U(A)$ and the chemical shift was already demonstrated in Figs. 43 and 44. The β ratios are also related to the value of $U(A)$ that further helps to predict CTL energies in compounds. The interaction of the $3d$ electrons with the negative ligands around the TM is the cause of the nephelauxetic effect. When ligands are less strongly bonded, it leads to better screening that, in the case of lanthanides, decreases $U(A)$. It also leads to a larger nephelauxetic effect which explains the correlation between $U(A)$ and the three β ratios in Table 8. An increase of valence Q of the TM leads to an increased screening charge on the ligands. This leads to a larger chemical shift $E_{cs}(1, Q, A)$ and larger crystal field splitting $\Delta(Q, A)$ evident in Table 7. The larger screening charge also leads to a larger nephelauxetic effect and lower β ratios when Q becomes larger. Altogether the five parameters needed to reconstruct CTL energies are not independent, they change in a highly correlated fashion with the structure and properties of the compound.

8.5. Connections with earlier work

All theory behind Slater–Condon integrals, Racah parameters, and Tanabe–Sugano diagrams can be found in the comprehensive book of J.S. Griffith [4]. In that same book, Eq. (17) was used to demonstrate the origin of the typical zigzag shape in the ionization potentials of the divalent transition metals. Racah parameters A_r, B_r, and C_r were assumed constant with q and Q, and $C(q, 2+, \mathrm{vac})$ was assumed to decrease linearly with $(q - 1)$ as in Table 1. The ideas and theories behind Eq. (34), that were used to reconstruct the CTL energies, can be found in the archival literature. It is similar to the method of Allen [14] that was used by Mizushima et al. [19] to estimate the TM CTL energies in anatase-TiO_2. Following Griffith, they assumed a linearly decreasing spherical interaction energy $C(q, Q, A)$ with q that was expressed as $-\phi(Q, A) - (q-1)\eta(Q, A)$ as in Eq. (32). $\eta(Q, A)$ was introduced to account for a less steep downward slope of CTL energies in compounds. It is equivalent to $-a_1(Q)\beta_{sp}(Q, A)$ that tilts the spherical interaction curve $C(q, Q, A)$ counterclockwise in Eq. (34). Mizushima et al. [19] report for the divalent TMs in vacuum, $\eta(2+, \mathrm{vac}) = 1.74$ eV which is to be compared with $-a_1(2+) = 1.78$ eV in Table 1. $\eta(Q, \mathrm{vac})$ for valences other than 2+ were not available. It was expected to increase with the

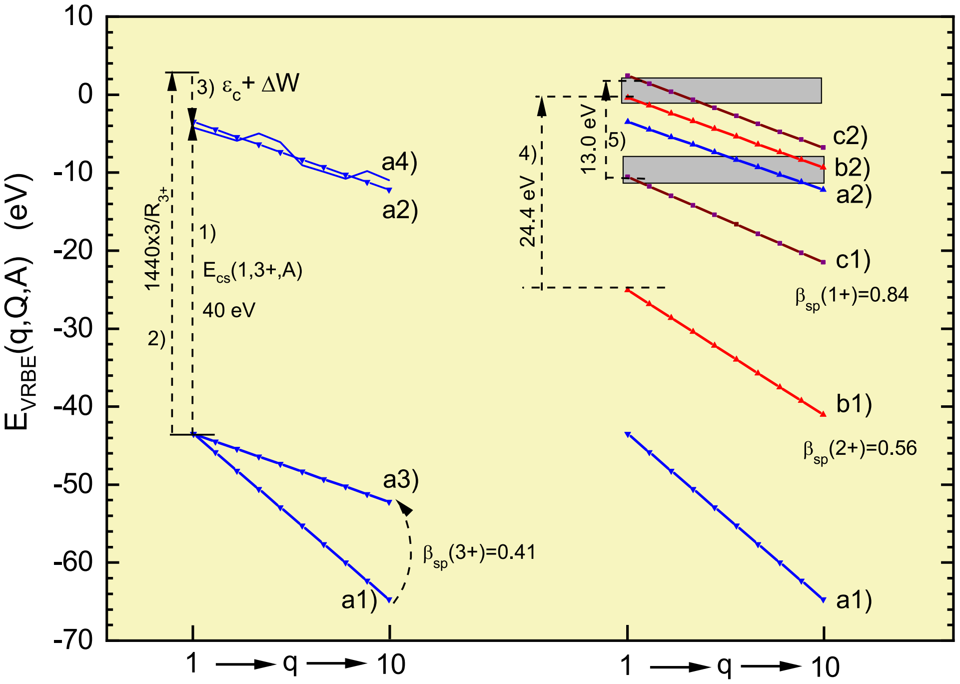

Fig. 48. Demonstration on how β_{sp} and $E_{cs}(1,Q,A)$, that represent the spherical interactions in the TM doped environment, affect the VRBEs in the TM^Q ground states. $\beta_{sp}(1+,A)$ = 0.84, $\beta_{sp}(2+,A)$ = 0.56, $\beta_{sp}(3+,A)$ = 0.41, and chemical shift $E_{cs}(1,1+,A)$ = 13.0 eV, $E_{cs}(1,2+,A)$ = 24.4 eV, and $E_{cs}(1,3+,A)$ = 40.0 eV were used. Curves (a1), (b1), (c1) connect the linearized spherical interaction energies $C(q,Q,\text{vac})$. Curve (a1) becomes curve (a3) after a tilt operation with $\beta_{sp}(3+,A)$=0.41. Curve (a2), (b2), (c2) are the result after applying both $\beta_{sp}(Q,A)$ and $E_{cs}(1,Q,A)$. Curve (a4) is obtained after adding an octahedral crystal field splitting $\Delta(3+,A)$ = 1.8 eV on the [HS] systems.

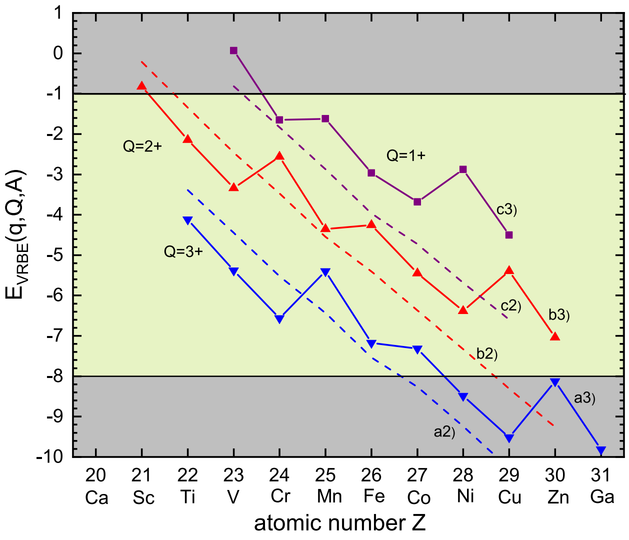

Fig. 49. Demonstration on how the parameters $\Delta(Q,A)$, $\beta_B(Q,A)$, $\beta_C(Q,A)$, that represent the directional parts of the interactions in the TM doped environment, affect the VRBE in the TM^Q ground state. Curves (a2), (b2), (c2) connect the spherical interaction energies $C(q,Q,A)$ for Q = 3+, 2+, and 1+ as obtained with $\beta_{sp}(1+,A)$ = 0.84, $\beta_{sp}(2+,A)$ = 0.56, $\beta_{sp}(3+,A)$ = 0.41, and chemical shift $E_{cs}(1,1+,A)$ = 13.0 eV, $E_{cs}(1,2+,A)$ = 24.4 eV, and $E_{cs}(1,3+,A)$ = 40.0 eV. Curves (a3), (b3), (c3) are obtained when effects of crystal field splitting, the directional parts of 3d-3d electrostatic interaction, and spin–orbit interaction are included. For $\beta_B(Q,A)$ values of 0.7, 0.6, 0.5 were used for Q = 1+, 2+, and 3+. The same values were used for β_C and β_ζ. Octahedral crystal field splitting $\Delta(Q,A)$ of 1.8 eV, 1.5 eV, and 1.3 eV were used for Q = 3+, 2+, 1+.

valence Q and estimated values were provided. The $-a_1(Q)$ values in Table 1 now provide the values from this work. In the 1960s, it was also expected and found that $\eta(Q,A)$ in compounds decreases. This is precisely what is observed for $\beta_{sp}(Q,A)$ in Fig. 47.

$\eta(Q,A)$ introduced in the 1960s or β_{sp} introduced in this work appears of fundamental importance for the TM VRBEs and CTL energies. However, after the work of Mizushima et al. in 1972, the classic theory with $\eta(Q,A)$ was rarely applied. Sharpe et al. [181] in 1990 used it to analyze the free energy of electron attachment to two types of TM-complexes in the gas phase. Since then, the method and proposed CTL energies were referenced only to benchmark computational results on TMs in TiO$_2$ in [7,159].

Tippins [48] in 1970, explained the VB→TM^{3+} CT energy in Al$_2$O$_3$ with expression $C - I(M^{2+}) + \Delta E_d$. Here, $I(M^{2+})$ is the ionization potential of divalent TMs and is equivalent to $-E_{VRBE}(q,2+,\text{vac})$. Therefore, the authors assumed that there is no nephelauxetic effect in Al$_2$O$_3$. ΔE_d accounts for the effect of the crystal field splitting, and it is equivalent to the last two terms of Eq. (34) containing the crystal field energies ϵ_i. Their value C = 36.24 eV was chosen to arrive at the best agreement with the V, Cr, and Fe data. C serves the same purpose as the chemical shift in this work. The Ni^{2+} VRBE turned out 2.7 eV higher than the VRBE predicted with their expression. With hindsight, from the knowledge in the present work, this difference is entirely due to the counterclockwise tilting of the $C(q,2+,\text{Al}_2\text{O}_3)$ curve by the $\beta_{sp}(2+,\text{Al}_2\text{O}_3)$ = 0.56 parameter. When the nephelauxetic effect is accounted for, the experimental data of Tippins can be reproduced quite well with Eq. (34) as demonstrated in Fig. 26.

Sabatini et al. [47] in 1975, Chase et al. [93] in 1976, and McClure et al. [50] in 1979 followed the approach of Tippins in their studies on TMs in KMgF$_3$, LiF, NaF, and LiCl. In their analysis of electron transfer spectra, a nephelauxetic effect was not accounted for either. The nephelauxetic effect will be small for the ionic fluoride compounds and low valence TMs in LiCl, and this is possibly the reason why still satisfactory agreement with $C - I(M^{2+}) + \Delta E_d$ was obtained. The nephelauxetic effect was also ignored in the studies of lanthanide CTLs in the bandgap in the 1970s and 1980s. This is not too serious, since the nephelauxetic effect is always small for the 4f lanthanides.

The redox potential of TMs in electrochemistry depends on the type of complex surrounding the TM, and in 1980 a satisfactory explanation was not yet available as discussed by Lintvedt and Fenton [37]. This topic was further addressed by van Gaal and van der Linden [38] in 1982. They collected redox data on about 15 TM organic complexes with octahedral ligand coordination. Using their words, the most striking observation was that different types of organic complexes show large differences in the slope $-\Delta\epsilon(t_{2g})/\Delta n$. Although different symbols are used, this slope is the same as the downward slope in VRBE energy for $q = 1$ to 3 when the t_{2g} level is filled with three electrons. Van Gaal and van der Linden realized that the changing slope is related to the net donor strength of the ligand. Ligand donor strength is another wording for concepts like ligand polarizability, screening distance, co-valence, ionicity, nephelauxetic effect, and the value of $U(A)$.

The slope $-\Delta\epsilon(t_{2g})/\Delta n$ of 1.5–1.9 V/q in the (II/III) redox potential for $TM(H_2O)_6^{2+}$ aqua-complexes in [38] must be compared with the slope of −1.5 eV/q for the TM^{2+} VRBE in water as illustrated by the straight dashed line in Fig. 40. Likewise, the slope of 0.3-0.4 V/q for the (III/IV) redox potential for $TM(dtc)_3^0$ in [38] is to be compared with the slope of −0.39 eV/q as illustrated by the straight dashed line in Fig. 42. This changing slope is directly related to our $\beta_{sp}(Q,A)$ and $\eta(Q,A)$ used by Mizushima et al. [19]. However, it is not the same. Van Gaal and van der Linden did not account for the contribution from Racah parameter B_r to the slope in the redox potentials for $q = 1$ to 3. The effect is visible in Fig. 49 where the downward slope in the beginning part from $q = 1$ to 3 of the CTL curves (a3), (b3), (c3) is steeper than that in the $C(q,Q,A)$ curves (a2), (b2), (c2).

Before 1982, TM levels in the bandgap were always placed relative to the host bands. The main and most important difference in the present work is that all energies are relative to the vacuum level enabling us to determine the chemical shift $E_{cs}(1,Q,A)$. A first attempt to relate CTL energies to the vacuum level was by Ledebo et al. [39] in 1982 and Caldas et al. [40] in 1984. They observed that the TM CTL energies relative to the host valence band in II–IV and III–V semiconductors start to coincide when energies are relative to the vacuum level. They concluded that within a class of compounds the VRBE of each impurity is nearly constant, despite significant variations in host-referred binding energies (HRBE). Langer et al. [41,43,44] used that new insight to determine the valence band offsets at the heterojunction between two semiconductors. The results of the present work explain why VRBE is nearly constant, and why and how it will differ from compound to compound.

Delerue et al. [42] employed a self-consistent semi-empirical tight-binding theory to compute the TM CTL energies in semiconductors. Although the experimental variation in CTL with the type of TM and with the type of compound could be reproduced satisfactorily, the approach does not allow a comparison with the various parameters in Table 7 and 8. The same applies to the more recent computations with the VASP 5.3 code in 2019 by Qu et al. [56] on the energy of the VB→TM^{3+} and TM^{4+} electron transfer transition in Al_2O_3 and $Y_3Al_5O_{12}$. Although calculations systematically underestimate the electron transfer energy to TM^{3+} by ≈ 0.7 eV and about 1.5 eV for transfer to TM^{4+}, the experimental trends when q increases were reproduced. However, insight into why and how the CTL energies change with the type of environment is not obtained with these computations.

In a series of papers, Jing et al. [9–11] developed methods to establish the CTL energies of the TMs. It started with computational studies [9] on Ti-doped α-Al_2O_3 that provided the energy needed for electron transfer from the VB-top to Ti^{4+} and the energy needed for photo-ionization (PI) of Ti^{3+}. The results are consistent with the experimental data. The study was later extended to the entire series of TMs in α-Al_2O_3, $MgAl_2O_4$, MgO, $KMgF_3$ and MgF_2 where the TM is on an Al or Mg site with octahedral coordination [10]. VRBE energies at the VB-top were computed employing the slab-and-vacuum model. The $TM^{3+/2+}$ and $TM^{4+/3+}$ CTL energies follow similar patterns in the above five compounds. Note that their results were used in Figs. 17, 18, 19, 26, 27, 28, and 29.

Jing et al. tried to reproduce their computed VRBE energies with a set of parameters to arrive at a predictive model. They found that the computed curves could be reproduced from the free-ion VRBE energies. First, the computed effect of the crystal field needs to be subtracted from the computed VRBE curve. The remaining curve then resembles a tilted version of the free-ion VRBE energies. Jing et al. [10,11] introduce a tilting parameter $\alpha(Q,A)$ that depends on the valence of the TM and the electronegativity of the ligand (F, Cl, Br, I, O, S, Se). Jing et al. also needed to introduce a separate α_1 for the left-hand branch ($q = 1$ to 5) and α_2 for the right-hand branch ($q = 6$ to 10) that was attributed to the nephelauxetic effect. The introduction of α, α_1, and α_2 were made on purely empirical grounds, and a physical or chemical explanation was not provided. Unfortunately, the classic theory was not used to interpret the computed results. Rather than tilting the free-ion VRBE curve $E_{VRBE}(q,Q,\mathrm{vac})$ with parameter $\alpha(Q,A)$, Eq. (34) tilts the free-ion spherical interaction curve $C(q,Q,\mathrm{vac})$ with parameter $\beta_{sp}(Q,A)$. The $\beta_{sp}(Q,A)$ parameter has the same dependence on valence Q of the TM and on the electronegativity of the ligand as $\alpha(Q,A)$. There will also be no need to introduce α_1 and α_2 because the reduction of the Racah parameter C_r will cover that with the $S(q,Q,A)$ term in Eq. (34).

8.6. Error sources and methods for improvements

The various error sources and the quality of the reconstructed CTL curves are further addressed in this section. Different assumptions led to Eq. (34), and further assumptions were made in using that equation to reconstruct the CTL energies. Starting with the chemical shift $E_{cs}(q,Q,A)$. Here we assumed that the q dependence is approximately linear with q, and then the q dependence was accounted for by the value for $\beta_{sp}(Q,A)$. $E_{cs}(q,Q,A)$ could then be replaced by $E_{cs}(1,Q,A)$ in Eq. (34). The introduction of the spherical nephelauxetic ratio $\beta_{sp}(Q,A)$ assumed that the nephelauxetic effect reduces $W(q,Q,A)$, $V(q,Q,A)$ and $A_r(q,Q,A)$ with the same factor β_{sp}. This was motivated by the fact that the integrals that determine W, V, and A all contain the same argument $(R_{3d}(r))^2$, see *e.g.* Eqs. (2), (3), and (9). The integrals are similar but not the same. Whether the assumptions are justified in compounds can only be tested by comparison with experimental data on VRBE energies.

The crystal field splitting as derived from $3d^q$ Tanabe–Sugano diagrams often shows a significant q dependence. Baranowski et al. [170] in 1967 collected data on $\Delta(q,2+,A)$ for the II–VI semiconductors ZnO, ZnTe, ZnS, CdS, ZnSe, CdTe. $\Delta(q,2+,A)$ varies quite substantially from 0.4 eV for $3d^6$ Fe^{2+} to 0.6-0.7 eV for $3d^4$ Cr^{2+} and $3d^9$ Cu^{2+}. An explanation was not provided. Langer et al. [176] in 1971 report similar dependence on q for CdSe and suggested possible causes. For $KMgF_3$ with octahedral sites $\Delta(q,2+,KMgF_3)$ is ≈ 1.5 eV for $3d^3$ V^{2+} and $3d^4$ Cr^{2+} and around 0.9–1.1 eV for Mn^{2+}, Fe^{2+}, Co^{2+}, and Ni^{2+} [47,88,91]. A clear pattern on how $\Delta(q,Q,A)$ changes with q and A is not yet available, and the topic has not attracted much attention during the past 40 years. For all reconstructed CTL curves in this work, a dependence on q for the crystal field splitting $\Delta(q,Q,A)$ was not taken into account, and this can be a serious omission.

The dependence of the crystal field splitting $\Delta(Q,A)$ on the valence Q was accounted for by introducing $\gamma(Q)$ in Eq. (33). Curves (2) and (3) in Fig. 13 demonstrate the effect on the CTL energies when $\Delta(q,3+,A) =$ 2.2 eV and when $\Delta(q,4+,A)$ is a factor $1+\gamma(3+) = 1.15$ larger. The largest difference of about 0.4 eV occurs for $q = 4$ and $q = 9$ when the $3d$ electron is removed from the e_g state upon oxidation. In this work, we always used $\gamma(3+) = 0.15$, $\gamma(2+) = 0.2$, and $\gamma(1+) = 0.25$. If larger or smaller values are used, differences in reconstructed CTL energy of several 0.1 eV will result.

Often quite similar values were chosen for β_B and β_C to reconstruct the CTL energies. The expressions Eq. (4) and (5) for the Racah parameters show that similar values can only be obtained when the nephelauxetic effect reduces the Slater–Condon integrals F^2 and F^4

with the same factor. It has been suggested several times (see *e.g.* the discussion on page 259 in [58]) that F^2 is more decreased by the nephelauxetic effect than F^4. Eq. (4) and (5) then predict that B_r is more decreased than C_r, and β_B will be smaller than β_C. In a review on Ni^{2+}, Cr^{3+}, and Mn^{4+} spectroscopy in crystals by Brik and co-workers [70,182], it is indeed observed that on average β_B is ≈ 0.15 smaller than β_C.

To account for the energy of lattice relaxation and electron–hole binding energy in the electron transfer data, we have assumed $(E^{CT}_{e-h}(\mathrm{TM^Q}, A) - E^{CT}_{rel}(\mathrm{TM^Q}, A)) = 0$ in Eq. (35). The energy at the maximum of the VB→TM^{Q+1} charge transfer band observed in spectra is then a measure for the location of the $\mathrm{TM}^{Q+1/Q}$ CTL energy above the VB-top. The same applies to TM^q→CB electron transfer data. $E^{CT}_{e-h}(\mathrm{TM^Q}, A)$ and $E^{CT}_{rel}(\mathrm{TM^Q}, A)$ are mostly determined by the host lattice and not much by the type of transition metal. An error in the assumption will then be systematic in q that affects the value obtained for the chemical shift $E_{cs}(1, Q, A)$.

The energy E^{CT}_{rel} of lattice relaxation is connected with the width (FWHM) of the CT band. There are indications that the width, and therewith E^{CT}_{rel}, decreases less rapidly with decreasing E^{ex} than the binding energy E^{CT}_{e-h}. For example, for the small-bandgap semiconductors, E^{ex} is of the order of 50–100 meV whereas the FWHM of the CT-bands is several 0.1 eV [169]. This implies that $(E^{CT}_{e-h}(\mathrm{TM^Q}, A) - E^{CT}_{rel}(\mathrm{TM^Q}, A))$ becomes < 0 for small-bandgap compounds. An energy smaller than that at the CT-band maximum should then be used to place the CTL above the VB-top. In Fig. 38, the experimental CTL data for GaP were based on the onset of the CT bands. The dashed line at 0.23 eV above the reconstructed curve (2) in Fig. 38 would be obtained using the maxima of the CT-bands. What the best method is will require a dedicated study and has been left open in this work.

9. Summary, conclusions, and outlook

In this work, we have reviewed and applied the classic theory of the 1950s–1960s to derive Eq. (34) for the $\mathrm{TM}^{Q+1/Q}$ CTL energy or VRBE in the ground state of TM^Q. Unlike almost all previous work, the energies are relative to the vacuum level. The archival literature dating back more than 70 years has been analyzed to obtain experimental data that enables us to place the CTLs relative to either the VB-top or the CB-bottom. It comprises information on 18 different compounds or chemical environments in which TM^Q is 6-fold octahedrally or 4-fold tetrahedrally coordinated with anions. Wide-bandgap halides (F, Cl, Br), chalcogenides (O, S, Se), and the II–VI and III–V small-bandgap semiconductors provide an almost full gamut of types of inorganic compounds. In addition, two TM organic complexes are treated.

To translate experimental CTL energies relative to the host bands into CTL energies relative to the vacuum level, the ideas and methods developed for the lanthanides, particularly the Chemical Shift model, were used. The parameters with Eq. (34) were chosen to reconstruct $\mathrm{TM}^{Q+1/Q}$ CTL energies until a good agreement with the available experimental data is obtained. Those parameters are; the chemical shift $E_{cs}(1, Q, A)$, the spherical nephelauxetic ratio $\beta_{sp}(Q, A)$, the octahedral or tetrahedral crystal field splitting $\Delta(Q, A)$, the directional nephelauxetic ratios $\beta_B(Q, A)$ and $\beta_C(Q, A)$, and the spin–orbit nephelauxetic ratio $\beta_\zeta(Q, A)$. The last four parameters can be derived from the Tanabe–Sugano diagrams that apply to the TM^Q in the compounds.

The chemical shift $E_{cs}(1, Q, A)$ appears to increase almost proportionally with the valence Q of the TM. This confirms the main idea behind the Chemical Shift model for the lanthanides, *i.e.*, a Q+ cation is effectively screened by a Q- charge from the surrounding environment. The chemical shift is then caused by the Coulomb repulsion from such screening charge. $E_{cs}(1, Q, A)$ shows a rather mild dependence on the type of environment characterized by the $U(A)$ value. Since $U(A)$ is known from lanthanide-doped compounds or can be estimated from the composition of the compound, one may predict the chemical shift in compounds. This work shows that the four nephelauxetic ratios change with the valence Q of the TM and the $U(A)$ value of the compound/environment in a predictable manner.

Altogether, a broad perspective has been obtained on how and why the $\mathrm{TM}^{Q+1/Q}$ CTL energies change with the valence and the type of environment. Such a perspective enables us to provide a good first guess about where to expect the CTL energies in the bandgap of compounds. Every additional piece of information, either from one TM or several TMs can then be used to better estimate the parameters in Eq. (34) and to provide a better reconstruction and prediction of the CTL energies. The various assumptions made to derive Eq. (34) and to reconstruct CTL curves, provide limitations to accuracy. However, that also applies to computational methods. The merging of the classic theory of Eq. (34) with computational methods might be a route to a better understanding and a route to obtain better predictive models.

CRediT authorship contribution statement

Pieter Dorenbos: Writing – review & editing, Writing – original draft, Visualization, Validation, Supervision, Software, Resources, Project administration, Methodology, Investigation, Formal analysis, Data curation, Conceptualization.

Declaration of competing interest

The authors declare that they have no known competing financial interests or personal relationships that could have appeared to influence the work reported in this paper.

Acknowledgments

The author thanks Jeffrey Zom and J. Jasper van Blaaderen for proofreading the manuscript and providing valuable advice.

Appendix A. Supplementary data

Supplementary material related to this article can be found online at https://doi.org/10.1016/j.optmat.2025.117007.

Data availability

Data will be made available on request.

References

[1] K. Petermann, Handbook of Solid State Physics, Materials Systems and Applications, in: Woodhead Publishing Series in Electronic and Optical Materials, 2013, pp. 3–27.
[2] John B. Goodenough, Youngsik Kim, Chem. Mater. 22 (2010) 587.
[3] R. van de Krol, Yongqi Liang, J. Schoonman, J. Mat. Chem. 18 (2008) 2311.
[4] J.S. Griffith, The Theory of Transition-Metal Ions, Cambridge University Press, London, 1961.
[5] M.G. Brik, A.M. Srivastava, Opt. Mater. 35 (2013) 1776.
[6] Mikhail G. Brik, Chong-Geng Ma, Theoretical Spectroscopy of Transition Metal and Rare Earth Ions, Jenny Stanford Publishing, ISBN: 978-981-4800-56-3, 2020.
[7] William Lafargue-Dit-Hauret, Camille Latouche, Stephane Jobic, J. Phys. Chem. C 125 (2021) 4267.
[8] William Lafargue Dit Hauret, Mathieu Allix, Bruno Viana, Stephane Jobic, Camille Latouche, Theor. Chem. Accounts 141 (2022) 58.
[9] Weiguo Jing, Mingzhe Liu, Jun Wen, Lixin Ning, Min Yin, Chang-Kui Duan, Phys. Rev. B 104 (2021) 165103.
[10] Weiguo Jing, Mingzhe Liu, Xiantao Wei, Chong-Geng Ma, Min Yin, Chang-Kui Duan, Phys. Rev. B 106 (2022) 075110.
[11] Weiguo Jing, Jiaqi Tang, Mingzhe Liu, Chang-Kui Duan, Inorg. Chem. 63 (2024) 4972.
[12] Jiaqi Tang, Chang-Kui Duan, Opt. Mater. 159 (2025) 116560.
[13] C.K. Jorgensen, Mol. Phys. 2 (1959) 309.
[14] J.W. Allen, Proc. of the 7th International Conf. on Semiconductors, Dunod Paris, 1964, p. 781.

[15] P. Dorenbos, Phys. Rev. B 85 (2012) 165107.
[16] P. Dorenbos, J. Lumin. 214 (2019) 116536.
[17] P. Dorenbos, J. Lumin. 222 (2020) 117164.
[18] C.K. Jørgensen, Mol. Phys. 5 (1962) 271.
[19] K. Mizushima, M. Tanaka, S. Iida, J. Phys. Soc. Japan 32 (1972) 1519.
[20] G. Racah, Phys. Rev. 62 (1942) 186.
[21] G. Racah, Phys. Rev. 62 (1942) 438.
[22] G.H. Dieke, H.M. Crosswhite, Appl. Opt. 2 (1963) 675.
[23] K. Mizushima, M. Tanaka, A. Asai, S. Iida, J.B. Goodenough, J. Phys. Chem. Sol. 40 (1979) 1129.
[24] D.S. McClure, Z. Kiss, J. Chem. Phys. 39 (1963) 3251.
[25] D.A. Johnson, J. Chem. Soc. (A) (1969) 1525.
[26] L.J. Nugent, J. Inorg. Nucl. Chem. 32 (1970) 3485.
[27] L.R. Morss, Chem. Rev. 76 (1976) 827.
[28] D.A. Johnson, J. Chem. Soc. Dalton Trans. (1974) 1577.
[29] L.J. Nugent, R.D. Baybarz, J.L. Burnett, J. Phys. Chem. 73 (1969) 1177.
[30] L.J. Nugent, K.L. Vander Sluis, J. Opt. Soc. Am. 61 (1971) 1112.
[31] K.L. Vander Sluis, L.J. Nugent, Phys. Rev. A 6 (1972) 86.
[32] L.J. Nugent, R.D. Baybarz, J.L. Burnett, J.L. Ryan, J. Phys. Chem. 77 (1973) 1528.
[33] K.L. Vander Sluis, L.J. Nugent, J. Opt. Soc. Amer. 64 (1974) 687.
[34] L.J. Nugent, J. Inorg. Nucl. Chem. 37 (1975) 1767.
[35] I. Kawabe, Geochem. J. 26 (1992) 309.
[36] P.A. Rock, Inorg. Chem. 7 (1968) 837.
[37] R.L. Lintvedt, D.E. Fenton, Inorg. Chem. 19 (1980) 569.
[38] H.L.M. van Gaal, J.G.M. van der Linden, Coord. Chem. Rev. 47 (1982) 41.
[39] L.A. Ledebo, B.K. Ridley, J. Phys. C: Solid State Phys. 15 (1982) L961.
[40] M.J. Caldas, A. Fazzio, A. Zunger, Appl. Phys. Lett. 45 (1984) 671.
[41] C. Delerue, M. Lannoo, J.M. Langer, Phys. Rev. Lett. 61 (1988) 199.
[42] C. Delerue, M. Lannoo, G. Allan, Phys. Rev. B 39 (1989) 1669.
[43] J.M. Langer, H. Heinrich, Phys. Rev. Lett. 55 (1985) 1414.
[44] J.M. Langer, C. Delerue, M. Lannoo, H. Heinrich, Phys. Rev. B. 38 (1988) 7723.
[45] Sadao Adachi, J. Lumin. 273 (2024) 120628.
[46] D.S. McClure, J. Chem. Phys. 36 (1962) 2757.
[47] J.F. Sabatini, A.E. Salwin, D.S. McClure, Phys. Rev. B 11 (1975) 3832.
[48] H.H. Tippins, Phys. Rev. B 1 (1970) 126.
[49] A.G. Coutts, P. Day, Phys. Stat. Sol. (B) 88 (1978) 767.
[50] D.S. McClure, J. Lumin. 18/19 (1979) 235.
[51] D.S. McClure, C. Pedrini, Le J. de Phys. Colloq. 46 (C7) (1985) C7-397.
[52] C.W. Thiel, H. Cruguel, H. Wu, Y. Sun, G.J. Lapeyre, R.L. Cone, R.W. Equall, R.M. Macfarlane, Phys. Rev. B 64 (2001) 085107.
[53] P. Dorenbos, J. Phys.: Condens. Matter. 15 (2003) 8417.
[54] K. Izumi, S. Miyazaki, S. Yoshida, T. Mizokawa, E. Hanamura, Phys. Rev. B 76 (2007) 075111.
[55] Shota Takemura, Kazuyoshi Ogasawara, Opt. Mater.: X 1 (2019) 100005.
[56] Bingyan Qu, Rulong Zhou, Lei Wang, Pieter Dorenbos, J. Mater. Chem. C 7 (2019) 95.
[57] Bingyan Qu, Meizhen Liu, Rulong Zhou, Yang Jiang, Lei Wang, J. Lumin. 247 (2022) 118919.
[58] C.K. Jørgensen, Modern Aspects of Ligand Field Theory, North-Holland Publishing Company, Amsterdam, 1971.
[59] K.A. Schneidner, Jr. Le Roy Eyring (Eds.), Vol. 3 Non-Metallic Compounds, in: Handbook on the Physics and Chemistry of Rare Earths, North-Holland Publ. Comp. Amsteram, New York, Oxford, 1979.
[60] Basic Atomic Spectroscopic Data, National Institute of Standards and Technology, https://physics.nist.gov.
[61] R.D. Shannon, Acta Crystallogr. Sect. A: Cryst. Phys. Diffr. Theor. Gen. Crystallogr. 32 (1976) 751.
[62] C. Gorller-Walr, K. Binnemans, in: K.A. Gschneidner Jr., L. Eyring (Eds.), Handbook on the Physics and Chemistry of Rare Earths, Vol. 23, Elsevier Science B.V., Amsterdam, 1996, Chap. 155.
[63] P. Dorenbos, J. Lumin. 267 (2024) 120358.
[64] P. Dorenbos, J. Lumin. 135 (2013) 93.
[65] P. Dorenbos, Phys. Rev. B 62 (2000) 15640.
[66] P. Dorenbos, Phys. Rev. B 62 (2000) 15650.
[67] P. Dorenbos, Phys. Rev. B 64 (2001) 125117.
[68] P. Dorenbos, J. Lumin. 99 (2002) 283.
[69] P. Dorenbos, Phys. Rev. B 65 (2002) 235110.
[70] M.G. Brik, S.J. Camardello, A.M. Srivastava, ECS J. Solid State Sci. Technol. 4 (2015) R39.
[71] E.G. Rogers, P. Dorenbos, J. Lumin. 146 (2014) 445.
[72] P. Dorenbos, J. Phys.: Condens. Matter. 15 (2003) 4797.
[73] P. Dorenbos, ECS J. Solid State Sci. Technol. 2 (2013) R3001.
[74] Open Access LibreTexts Chemistry website https://chem.libretexts.org.
[75] E.G. Rogers, P. Dorenbos, J. Lumin. 153 (2014) 40.
[76] Jeffrey W. Turner, Franklin A. Schultz, Coord. Chem. Rev. 219–221 (2001) 81.
[77] F.A. Schultz, J Solid State Electrochem. 15 (2011) 1833.
[78] P. Dorenbos, Phys. Rev. B 87 (2013) 035118.
[79] P. Dorenbos, J. Lumin. 136 (2013) 122.
[80] P. Dorenbos, J. Phys.: Condens. Matter. 25 (2013) 225501.
[81] P. Dorenbos, J. Mater. Chem. C 11 (2023) 8129.
[82] P. Dorenbos, Opt. Mater. 69 (2017) 8.
[83] P. Dorenbos, Opt. Mater. X 22 (2024) 100316.
[84] P. Dorenbos, J. Lumin. 269 (2024) 120443.
[85] M.D. Sturge, Phys. Rev. 130 (1963) 639.
[86] E. Feher, M.D. Sturge, Phys. Rev. 172 (1968) 244.
[87] M.G. Brik, N.M. Avram, J. Phys.: Condens. Matter. 21 (2009) 155502.
[88] M.D. Sturge, F.R. Merritt, L.F. Johnson, H.J. Guggenheim, J.P. van der Ziel, J. Chem. Phys. 54 (1971) 405.
[89] R. Nistora, A.S. Gruia, Optoelectron. Adv. Mater. Rapid Comm. 6 (2012) 717.
[90] J. Ferguson, H.J. Guggenheim, H. Kamimura, Y. Tanabe, J. Chem. Phys. 42 (1965) 775.
[91] K. Knox, R.G. Shulman, S. Sugano, Phys. Rev. 130 (1963) 512.
[92] E.G. Rogers, P. Dorenbos, ECS J. Sol. State Sci. Techn. 3 (2014) R173.
[93] D.B. Chase, D.S. McClure, J. Chem. Phys. 64 (1976) 74.
[94] J. Simonetti, D.S. McClure, J. Chem. Phys. 71 (1979) 793.
[95] S. Hirako, R. Onaka, J. Phys. Soc. Japan 51 (1982) 1255.
[96] R.T. Poole, J.G. Jenkin, J. Liesegang, R.C.G. Leckey, Phys. Rev. B 11 (1975) 5179.
[97] S.A. Payne, D.S. McClure, J. Phys. Chem. 88 (1984) 1379.
[98] J. Ackerman, C. Fouassier, E.M. Holt, S.L. Holt, Inorg. Chem. 11 (1972) 3119.
[99] J. Ramirez-Serrano, E. Madrigal, F. Ramos, U. Caldino Garcia, J. Lumin. 71 (1997) 169.
[100] U. Zorenko, T. Zorenko, T. Voznyak, S. Nizhankovskiy, E. Krivonosov, A. Danko, V. Puzikov, Opt. Mater. 35 (2013) 2053.
[101] V.A. Pustovarov, V.S. Kortov, S.V. Zvonarev, A.I. Medvedev, J. Lumin. 132 (2012) 2868.
[102] J.B. Blum, H.L. Tuller, R.L. Coble, J. Am. Ceram. Soc. 65 (1982) 379.
[103] M. Kirm, G. Zimmerer, E. Feldbach, A. Lushchik, Ch. Lushchik, F. Savikhin, Phys. Rev. B 60 (1999) 502.
[104] W.C. Wong, D.S. McClure, S.A. Basun, M.R. Kokta, Phys. Rev. B 51 (1995) 5682.
[105] G. Molnar, M. Benabdesselam, J. Borossay, D. Lapraz, P. Iacconi, V.S. Kortov, A.I. Surdo, Radiat. Meas. 33 (2001) 663.
[106] M. Yamaga, T. Yosida, S. Hara, N. Kodama, B. Henderson, J. Appl. Phys. 75 (1994) 1111.
[107] J.P. Meyn, T. Danger, K. Petermann, G. Huber, J. Lumin. 55 (1993) 55.
[108] Renping Cao, Kaniyarakkal N. Sharafudeen, Jianrong Qiu, Spectrochim. Acta Part A: Mol. Biomol. Spectrosc. 117 (2014) 402.
[109] Yudong Xu, Lei Wang, Bingyan Qu, Di Li, Jie Lu, Rulong Zhou, J. Am. Ceram. Soc. 102 (2019) 2737.
[110] S.A. Basun, S.P. Feofilov, A.A. Kaplyanski, B.K. Sevastyanov, N. M.Yu. Sharonov, L.S. Starostina, J. Lumin. 53 (1992) 28.
[111] G.T. Pott, B.D. McNicol, J. Lumin. 6 (1973) 225.
[112] S. Geschwind, P. Kisliuk, M.P. Klein, J.P. Remeika, D. Wood, Phys. Rev. B. 126 (1962) 1684.
[113] G.S. White, R.V. Jones, J.H. Jr. Crawford, J. Appl. Phys. 53 (1982) 265.
[114] N.V. Kuleshov, V.G. Shcherbitsky, V.P. Mikhailov, S. Kuck, J. Koetke, K. Petermann, G. Huber, J. Lumin. 71 (1997) 265.
[115] L.E. Bausa, I. Vergara, J. Garcia Sole, W. Strek, P.J. Deren, J. Appl. Phys. 68 (1990) 736.
[116] T. Sato, M. Shirai, K. Tanaka, Y. Kawabe, E. Hanamura, J. Lumin. 114 (2005) 155.
[117] Zhaowu Wang, Haipeng Ji, Jian Xu, Xinghui Hou, Jumpei Ueda, Setsuhisa Tanabe, Shasha Yi, Ying Zhou, Deliang Chen, Inorg. Chem. 59 (2020) 18374.
[118] Wing C. Wong, Donald S. McClure, Sergei A. Basun, J. Lumin. 60–61 (1994) 183.
[119] V. Murk, N. Yaroshevich, Phys. Status Solidi (B) 181 (1994) K37.
[120] K. Petermann, G. Huber, J. Lumin. 31–32 (1984) 71.
[121] M.V. Korzhik, M.G. Livshits, N.I. Zotov, M.L. Meil'man, Transl. from Zhurnal Prikl. Spektrosk. 48 (6) (1988) 975.
[122] C.Y. Chen, G.J. Pogatshnik, Y. Chen, M.R. Kokta, Phys. Rev. B 38 (1988) 8555.
[123] S.R. Rotman, M. Roth, H.L. Tuller, C. Warde, J. Appl. Phys. 66 (3) (1989) 1366.
[124] J. Ueda, P. Dorenbos, A.J.J. Bos, K. Kuroishi, S. Tanabe, J. Mater. Chem. C 3 (2015) 5642.
[125] Jumpei Ueda, Atsunori Hashimoto, Shota Takemur, Kazuyoshi Ogasawara, Pieter Dorenbos, Setsuhisa Tanabe, J. Lumin. 192 (2017) 371.
[126] Wuhui Li, Yixi Zhuang, Peng Zheng, Tian-Liang Zhou, Jian Xu, Jumpei Ueda, Setsuhisa Tanabe, Le Wang, Rong-Jun Xie, ACS Appl. Mater. Interfaces 10 (2018) 27150.
[127] Tongde Huang, Benxue Jiang, Yusong Wu, Jiang Li, Yun Shi, Wenbin Liu, Yubai Pan, Jingkun Guo, J. Alloy. Comp. 478 (2009) L16.
[128] S. Kuck, K. Petermann, U. Pohlmann, G. Huber, J. Lumin. 68 (1996) 1.
[129] Daqin Chen, Yang Zhou, Wei Xu, Jiasong Zhong, Zhenguo Jia, Weidong Xiang, J. Mater. Chem. C 4 (2016) 1704.
[130] P. Peshev, V. Petrov, N. Manuilov, Mat. Res. Bull. 23 (1988) 1193.
[131] M.J. Weber, L.A. Riseberg, J. Chem. Phys. 55 (1971) 2032.
[132] Lei Wang, Xia Zhang, Zhendong Hao, Yongshi Luo, Xiao-jun Wang, Jiahua Zhang, Opt. Express 24 (2010) 25177.
[133] Mitsuo Yamaga, Yohei Oda, Hideaki Uno, Kazuo Hasegawa, Hiroshi Ito, Shintaro Mizuno, J. Appl. Phys. 112 (2012) 063508.
[134] S. Kuck, Appl. Phys. B 72 (2001) 515.

[135] A.Y. Polyakov, N.B. Smirnov, I.V. Schemerov, A.V. Chernykh, E.B. Yakimov, A.I. Kochkova, A.N. Tereshchenko, S.J. Pearton, ECS J. Solid State Sci. Tech. 8 (2019) Q3091.

[136] Palvan Seyidov, Joel B. Varley, Zbigniew Galazka, Ta-Shun Chou, Andreas Popp, Andreas Fiedler, Klaus Irmscher, APL Mater. 10 (2022) 111109.

[137] M.E. Ingebrigtsen, J.B. Varley, A. Yu. Kuznetsov, B.G. Svensson, G. Alfieri, A. Mihaila, U. Badstubner, L. Vines, Appl. Phys. Lett. 112 (2018) 042104.

[138] V. Zade, R. Swadipta, C. Ramana, JOM 74 (2022) 79.

[139] P. Seyidov, J.B. Varley, J.-X. Shen, Z. Galazka, Ta-Shun Chou, A. Popp, M. Albrecht, K. Irmscher, A. Fiedler, J. Appl. Phys. 134 (2023) 205701.

[140] J. Jesenovec, J. Varley, E. Karcher, J.S. McCloy, J. Appl. Phys. 129 (2021) 225702.

[141] C. Zimmermann, Y.K. Frodason, A.W. Barnard, J.B. Varley, K. Irmscher, Z. Galazka, A.i Karjalainen, W.E. Meyer, F.D. Auret, L. Vines, Appl. Phys. Lett. 116 (2020) 072101.

[142] Yi-Ying Lu, Feng Liu, Zhanjun Gu, Zhengwei Pan, J. Lumin. 131 (2011) 2784.

[143] Yaroslav Zhydachevskyy, Vitaliy Mykhaylyk, Vasyl Stasiv, Lev-Ivan Bulyk, Vasyl Hreb, Iryna Lutsyuk, Andriy Luchechko, Shusaku Hayama, Leonid Vasylechko, Andrzej Suchocki, Inorg. Chem. 61 (2022) 18135.

[144] P. Dorenbos, J. Lumin. 197 (2018) 62.

[145] R.L. Hansler, W.G. Segelken, J. Phys. Chem. Sol. 13 (1960) 124.

[146] K.W. Blazey, Phys. B 89 (1977) 47.

[147] A.M. Stoneham, M.J.L. Sangster, P.W. Tasker, Philos. Mag. Part B 44 (1981) 603.

[148] A.M. Stoneham, M.L.J. Sangster, Phil. Mag. B 43 (1981) 1463.

[149] A.J. Mann, P.J. Stephens, Phys. Rev. B 9 (1974) 863.

[150] Takumi Kato, Go Okada, Takayuki Yanagida, J. Ceram. Soc. Japan 124 (2016) 559.

[151] F.A. Modine, Phys. Rev. B 8 (1973) 854.

[152] W.M. Yen, L.R. Elias, D.L. Huber, Phys. Rev. Lett. 24 (1970) 1011.

[153] Jack C. Cheng, James C. Kemp, Phys. Rev. B 4 (1971) 2841.

[154] G.B. Scott, J.L. Page, Phys. Stat. Sol. (B) 79 (1977) 203.

[155] F.A. Modine, E. Sonder, R.A. Weeks, J. Appl. Phys. 48 (1977) 3514.

[156] L. Delgado, Solid State Commun. 50 (1984) 943.

[157] J.J. Schuyt, G.V.M. Williams, S.V. Chong, Opt. Mater. X 23 (2024) 100345.

[158] M.O. Henry, J.P. Larkin, G.F. Imbusch, Phys. Rev. B 13 (1976) 1893.

[159] Shang-Di Mo, L.B. Lin, D.L. Lin, J. Phys. Chem Sol. 55 (1994) 1309.

[160] Nick Serpone, Darren Lawless, Langmuir 10 (1994) 643.

[161] Nguyen Minh Thuy, Duong Quoc Van, Le Thi Hong Hai, Nanomater. Nanotechn. 2 (2012) 14.

[162] Song Liu, Tianhua Xie, Zhi Chen, Jiantao Wu, Appl. Surf. Sci. 255 (2009) 8587.

[163] Amal K. Ghosh, H. Paul Maruska, J. Electrochem. Soc. Electrochem. Sci. Technol. 124 (1977) 1516.

[164] Masakazu Anpo, Masato Takeuchi, J. Catalysis 216 (2003) 505.

[165] X.-X. Wu, W.-L. Feng, W.-C. Zheng, Phys. Stat. Sol. B 244 (2007) 3347.

[166] B. Clerjaud, C. Naud, B. Deveaud, B. Lambert, B. Plot, G. Bremond, C. Benjeddou, G. Guillot, A. Nouailhat, J. Appl. Phys. 58 (1985) 4207.

[167] P. Roura, G. Bremond, A. Nouailhat, G. Guillot, Appl. Phys. Lett. 51 (1987) 1696.

[168] A. Wolos, A. Wysmolek, M. Kaminska, A. Twardowski, M. Bockowski, I. Grzegory, S. Porowski, M. Potemski, Phys. Rev. B 70 (2004) 245202.

[169] E. Malguth, A. Hofmann, M.R. Phillips, Phys. Stat. Sol. B 245 (2008) 455.

[170] J.M. Baranowski, J.W. Allen, G.L. Pearson, Phys. Rev. 160 (1967) 627.

[171] J.M. Baranowski, J.W. Allen, G.L. Pearson, Phys. Rev. 167 (1968) 758.

[172] J.M. Baranowski, J.M. Langer, Phys. Stat. Sol. B 48 (1971) 863.

[173] K. Kocot, J.M. Baranowski, Phys. Stat. Sol. B 81 (1977) 629.

[174] T. Hoshina, J. Phys. Soc. Japan 22 (1967) 1049.

[175] J.M. Baranowski, Phuong An, Phys. Stat. Sol. 9 B 122 (1984) 331.

[176] J.M. Langer, J.M. Baranowski, Phys. Stat. Sol. B 44 (1971) 155.

[177] D.A. Johnson, P.G. Nelson, Inorg. Chem. 38 (1999) 4949.

[178] P. Petkova, V. Nedkov, J. Tacheva, P. Vasilev, I. Ismailov1, M. Mustafa, Y. Tzoukrovsky, J. Phys.: Conf. Ser. 558 (2014) 012029.

[179] D.A. Johnson, A.G. Sharpe, J. Chem. Soc. A (1966) 798.

[180] I. Vergara, E. Dieguez, L.E. Bausa, J. Garcia Sole, J. Phys. D: Appl. Phys. 24 (1991) 622.

[181] Paul Sharpe, John R. Eyler, David E. Richardson, Inorg. Chem. 29 (1990) 2779.

[182] M.G. Brik, S.J. Camardello, A.M. Srivastava, N.M. Avram, A. Suchocki, ECS J. Solid State Sci. Technol. 5 (2016) R3067.